Technical Physics Letters, Vol. 29, No. 2, 2003, pp. 102–104. Translated from Pis'ma v Zhurnal Tekhnicheskoĭ Fiziki, Vol. 29, No. 3, 2003, pp. 40–45.

Peculiarities of the Nonlinear Dynamics of a Gas Bubble under the Action of Resonance and Noise Acoustic Fields

A. O. Maksimov and E. V. Sosedko

Pacific Institute of Oceanology, Far-Eastern Division, Russian Academy of Sciences, Vladivostok, Russia
e-mail: pacific@online.marine.su

Received July 22, 2002

Abstract—An analysis of the nonlinear dynamics of a gas bubble in an acoustic field comprising a high-power harmonic signal and a noise component shows that the effect of the random component is significant in the region of bistability of this dynamical system. Behavior of the bubble in this region is characterized by a significant increase in the duration of transition processes and by an essentially non-Gaussian distribution of fluctuations in the vicinity of stable trajectories. *© 2003 MAIK "Nauka/Interperiodica".*

The spectrum of the radiation caused by acoustical cavitation has the form of separate bands, related to the nonlinear dynamics of the gas bubbles in the field of a high-power acoustic wave [1, 2], on a noise base related to the generation of short pulses accompanying the collapse of isolated inclusions [3–5].

Recently [6], the shape of spectral bands of the cavitation emission has been described within the framework of the simplest generalization of a traditional model. According to this approach, the real spectrum of the acoustic pressure inducing pulsation of individual bubbles in a cavitation sheet is represented by the sum of the main harmonic and a noise component. In [6], the analysis of the nonlinear dynamics of a bubble in the field of a high-power harmonic signal and a small noise component was performed using approximate analytical methods. The effect of fluctuations related to the random component of the acoustic field is most significant in the vicinity of the bifurcational values of the field and detuning, which correspond to a change in the number of stable oscillatory states of the bubble.

We have studied this most interesting regime corresponding to bistable oscillatory states of the bubble by numerical techniques. Below, we analyze the numerical solution and compare the results with the data obtained by analytical methods.

In the Rayeigh–Plesset equation describing radial pulsation of a gas bubble, the presence of a noise component is taken into account by an additional term entering into the expression for an external field acting upon the bubble:

$$R\ddot{R} + \frac{3}{2}\dot{R}^2 + \frac{P_0}{\rho_0}\left[1 - \left(\frac{R_0}{R}\right)^{3\gamma}\right] + 2\delta R_0\dot{R} = -\frac{P(t) - P_0}{\rho_0}. \quad (1)$$

Here, P_0, P, R_0, and R are the equilibrium and current values of the pressure in the liquid medium and the bubble radius, respectively; ρ_0 is the liquid density; γ is the polytrope exponent; δ is the damping constant; and $P(t) = P_0 + p_m\sin(\omega_p t) + p_N(t)$ (where p_m and ω_p are the amplitude and frequency of the high-power harmonic signal component, respectively, and $p_N(t)$ is the random noise). In what follows, we will use the same simplest model as in [6], assuming that p_N can be described as a Gaussian delta-correlated random process.

The results of solving Eq. (1) are presented in Fig. 1 in the form of a map of the phase portraits, representing dependences of $y \equiv (T\dot{R}/R_0)$ on $x \equiv ((R - R_0)/R_0)$, where $T = 2\pi/\omega_p$. The calculations were performed for the following values of control parameters: detuning $\eta = (\Omega_0^2(R_0)/\omega_p^2) - 1$ ($\Omega_0 = \sqrt{3\gamma P_a \rho_0^{-1}}R_0^{-1}$ is the natural frequency of pulsation), from –0.26 to 0.2 with a step of 0.06; quality factor $Q = \Omega_0/\delta = 10$; driving field ampli-

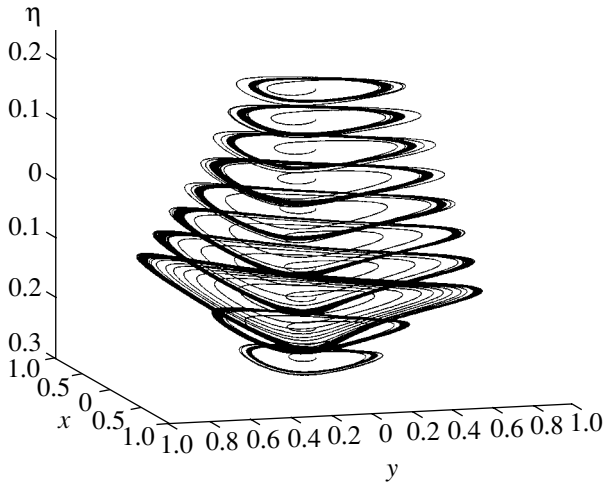

Fig. 1. Evolution of the phase portraits in the vicinity of the fundamental resonance.

1063-7850/03/2902-0102$24.00 © 2003 MAIK "Nauka/Interperiodica"

tude $(p_m/P_0) \equiv s = 1.1$; and noise intensity $\sqrt{(\overline{p_N^2}/P_0^2)} = 0.1$. This selection was determined by the formulation of the problem: we analyze the behavior of the system in the vicinity of the fundamental resonance for the values of detuning η and pressure amplitude *s* corresponding to the onset of bistability. Note that the degree of nonlinearity in this region is not high, which makes possible qualitative comparison with the results obtained by analytical methods in [6]. The duration of time evolution of the phase trajectories was equal to 400 periods of the external field. The results for greater time intervals are not presented here, because Eq. (1) becomes inapplicable and requires taking into account rectified diffusion, translational motions of the bubble, and correlation corrections to the average self-consistent field acting on the bubble. As can be seen from Fig. 1, there is an interval of detuning (coinciding with the region of bistability of the bubble pulsation in the absence of external noise) in which behavior of the phase trajectories is characterized by a significant increase in the duration of transition processes. In the steady state, the trajectories are grouped near one of the two stable orbits.

The character of bifurcation processes is more conveniently described by constructing Poincaré maps, rather than by considering the global evolution of the trajectories on the phase plane. Beginning with [7], bifurcations in the nonlinear oscillations of a bubble are analyzed by studying the dependence of the maximum radius of a bubble on the control parameters [8, 9]. This characteristic is not a Poincaré map during the initial period of time, when the evolution is determined by the transition processes, but it becomes such a map upon attaining the steady state. The convenience of this map is related to the fact that, considered as a function of detuning, it describes the amplitude–frequency characteristic of the bubble pulsation in the approximation of weak nonlinearity, which makes possible direct comparison of the numerical data to the results obtained by approximate analytical methods.

Figure 2a shows the results of calculation of the distribution density $f(x_{\max}, \eta)$ of the maximum radius $x_{\max} \equiv (R_{\max} - R_0)/R_0$, for the values of detuning η from the interval (–0.26, 0.2) in the region of the fundamental resonance. The distribution density is defined as $f(x_{\max}, \eta) \equiv [N(x_{\max})/(N\Delta x)]$, where $N(x_{\max})$ is the number of values of the maximum radius in the interval $[x_{\max} - \Delta x/2, x_{\max} + \Delta x/2]$ and, *N* is the total number of $R_{\max}$values in the time interval under consideration (in this case, 400 cycles). For reference, thin lines depict the Gaussian distributions characterized by the same mean values and dispersions as the $x_{\max}$ series for which the distribution function is constructed. In the (x, η) plane, the markers indicate the values of $x_{\max}$ (maximum radius) for the steady-state oscillations in the absence of a random force put in for the same values of

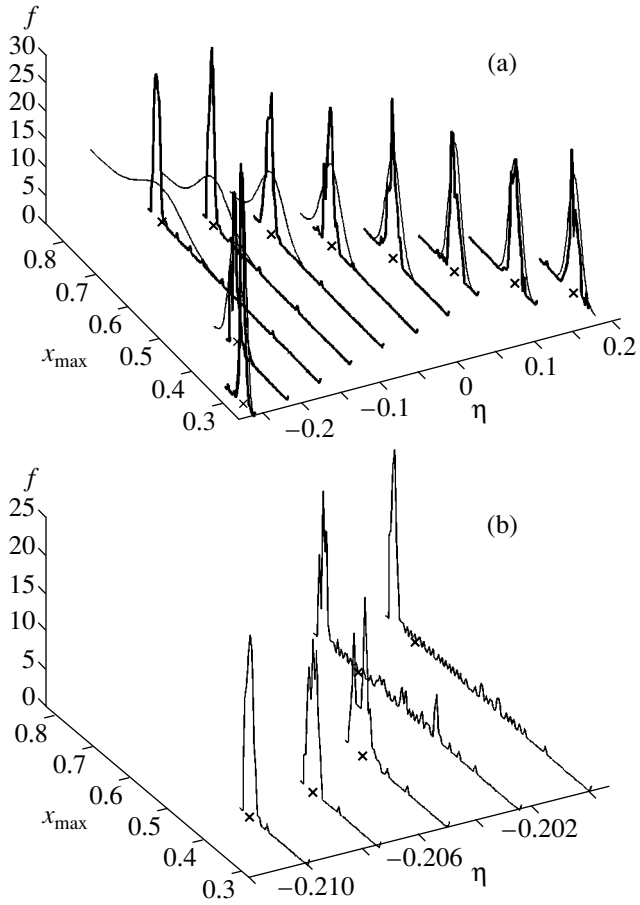

Fig. 2. Diagrams showing (a) evolution of the distribution density of the maximum radius of bubble pulsations and (b) transformation of the distribution density in the course of bifurcation.

detuning, which can be compared to the known data [7–9]. It should be noted that, since the realization of one of the two stable states in the region of bistability depends on the selection of the initial conditions and the method of detuning variation, the results correspond to $R(0) = R_0$, $\dot{R}(0) = 0$ and to an increase in η (i.e., to a decrease in the frequency of the external field ω_p at a fixed radius of the bubble). Figure 2b shows details of the distribution function transformation in the course of a transition from one stable state to another.

We can suggest the following physical interpretation of the results presented above. Outside the region of bistability, the effect of the noise component on the character of pulsation is small, the duration of transition processes is short, and the fluctuations of the bubble wall quite rapidly begin to follow the Gaussian distribution, in agreement with the results of the analytical description [6]. In the case of two stable states, the character of oscillations of the bubble—at least, within not too long an interval of time (400 cycles)—significantly differs from the physical pattern adopted in [6].

Here, the system sufficiently rapidly reaches one of the two stable orbits, performs small fluctuations near this trajectory, and exhibits rare transitions between the two stable orbits. As can be seen from Fig. 2, the distribution function has a complicated profile and significantly differs from a Gaussian, which is evidence of the weakly stable character of the bubble oscillations and the significant increase in the duration of transition processes. It should be noted that an analysis of the character of stochastic bifurcations (*P* or *D* bifurcations can take place in the system under consideration [10]) requires tracing the system over a time interval significantly greater than that in which description of the cavitation bubble dynamics by Eq. (1) can be considered as physically justified.

Acknowledgments. This study was supported by the Russian Foundation for Basic Research, project no. 01-02-96901.

REFERENCES

1. V. A. Akulichev, Pulsations of Cavitation Voids, in *High-Power Ultrasonic Fields*, Ed. by L. D. Rozenberg (Nauka, Moscow, 1968).
2. W. Lauterborn and E. Cramer, Acustica **49**, 280 (1981).
3. V. P. Morozov, Akust. Zh. **14**, 435 (1968).
4. Yu. L. Levkovskiĭ, Akust. Zh. **19**, 200 (1973).
5. R. Latorre, Acustica **83**, 424 (1997).
6. A. O. Maksimov, Akust. Zh. **47**, 110 (2001).
7. W. Lauterborn and E. Cramer, Acustica **49**, 226 (1981).
8. W. Lauterborn and J. Holzfuss, Phys. Lett. A **115**, 369 (1986).
9. V. Kamath and A. Prosperetti, J. Acoust. Soc. Am. **85**, 1539 (1989).
10. L. Arnold, *Random Dynamical Systems* (Springer-Verlag, Berlin, 1999).

Translated by P. Pozdeev

Technical Physics Letters, Vol. 29, No. 2, 2003, pp. 105–107. Translated from Pis'ma v Zhurnal Tekhnicheskoĭ Fiziki, Vol. 29, No. 3, 2003, pp. 46–52.

Electrical Activity of a Neuron Modeled by Piecewise Continuous Maps

K. V. Andreev and L. V. Krasichkov

Saratov State University, Saratov, Russia

e-mail: kandreev@cas.ssu.runnet.ru; lvk@cas.ssu.runnet.ru

Received July 30, 2002

Abstract—We suggest to model the electrical activity of an isolated neuron by using piecewise linear stochastic and piecewise continuous dynamic maps based on phenomenological notions about neuron dynamics. It is demonstrated that the proposed models provide for time series qualitatively similar to those observed in experiments with biological neurons. The possibility of using these models for constructing coupled neuron systems is discussed. *© 2003 MAIK "Nauka/Interperiodica".*

In the past decades, there has been growing interest in studying the behavior of neuron ensembles. Special attention has been paid to the problem of modeling the dynamics of such ensembles (see, e.g., review [1]). In order to provide for the effective numerical simulation of the behavior of large ensembles, it is important to develop simple models based on systems (maps) with discrete time. There were attempts at qualitatively describing the behavior of an isolated neuron within the framework of a model with discrete time and the variable of state running through a discrete set of values [2, 3]. For a detailed analysis of the behavior of a neuron ensemble, it is necessary that the map state variable take real values [4–6]. However, methods for constructing such maps are still incompletely developed and not formulated in final detail.

Below, we propose a method for constructing maps based on phenomenological notions about the electrical activity of neurons of the central pattern generator [1, 2].

According to the results of biological experiments (see, e.g., [7]), time series characterizing the neuron dynamics allow three qualitatively different regions to be distinguished (Fig. 1a). In constructing the neuron maps, these regions are described by different branches of a piecewise continuous mapping function, the passage from one to another branch being determined by specially selected transition conditions.

We propose a piecewise linear stochastic map based on two piecewise continuous mapping functions (Fig. 1b). By physical meaning, the state variable $x \in [0, 1]$ is analogous to the neuron membrane potential. The state variable $d = -1$ or 1 determines selection of one of the two piecewise linear mapping functions and the variable N_s is used to count the number of spikes generated within a given burst.

The piecewise linear map ($x' \longrightarrow x$) can be written in the following form:

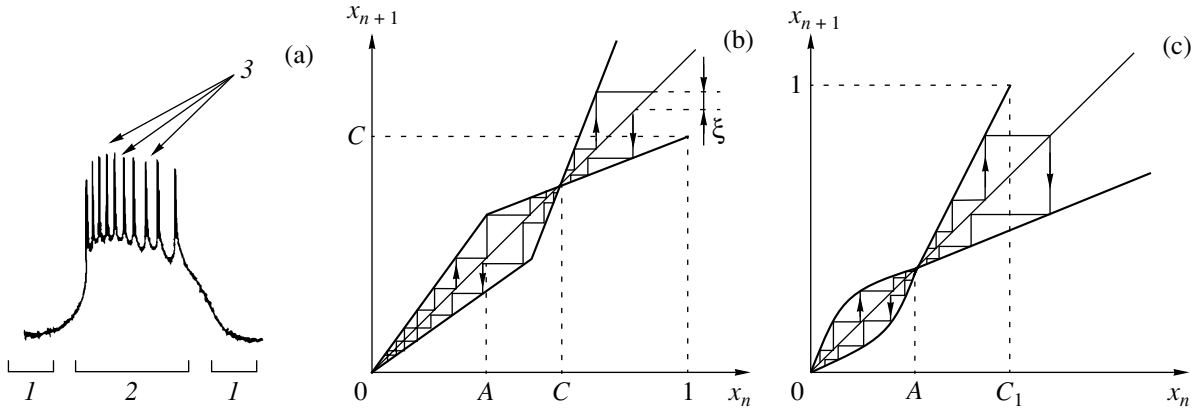

Fig. 1. (a) A fragment of the time series of a separate biological neuron showing (*1*) rest state, (*2*) burst, and (*3*) spikes; (b) the iteration diagram of a piecewise linear map; and (c) the iteration diagram of a piecewise continuous map.

1063-7850/03/2902-0105$24.00 © 2003 MAIK "Nauka/Interperiodica"

(i) $d = 1$ corresponds to an increase in the state variable x:

$$x' = \begin{cases} \alpha x, & x \in [0, A), \\ \beta(x - B) + B, & x \in [a, B - \delta_1), \\ 2B - x, & x \in [B - \delta_1, B), \\ \gamma(x - B) + B, & x \in [B, C), \\ x + \xi, & x \in [C, 1); \end{cases} \quad (1)$$

(ii) $d = -1$ corresponds to a decrease in the state variable x:

$$x' = \begin{cases} \frac{1}{\gamma}(x - B) + B, & x \in [B + \delta_2, 1], \\ 2B - x, & x \in [B, B + \delta_2), \quad N_s < N_s^0, \\ \frac{1}{\beta}(x - B) + B, & x \in [\alpha A, B), \\ \frac{1}{\alpha}x, & x \in [\delta_3, \alpha A); \end{cases} \quad (2)$$

(iii) additional conditions: $d = -1$ for $x \in [C, 1]$; $d = 1$, $N_s = N_s + 1$ for $x \in [B, B + \delta_2)$ and $N_s < N_s^0$, $N_s = 0$, for $x \in [B, B + \delta_2)$ and $N_s = N_s^0$; $d = 1$ for $x \in [0, \delta_3)$.

In Eqs. (1) and (2), the parameters A, α, β, γ, δ_1, δ_2, and δ_3 are subject to conditions following from the principle of mapping: $0 < A < 1$; $\alpha > 1$; $0 < \beta \le 1$; $\gamma > 1$; δ_1, δ_2, and $\delta_3 \ll 1$; $N_s^0 = 1, 2, 3, \ldots$ is the number of spikes in a given burst; ξ is a random value uniformly distributed over the interval [0, 0.01]; $B = A(\alpha - \beta)/(1 - \beta)$; and $C = (1 + B(\gamma - 1))/\gamma$.

Figure 2a presents time series obtained using the above map as the base for a separate neuron model. Note that the presence of an additive noise component ξ is of principal importance, since otherwise (in the absence of noise) the behavior of the system would be regular.

In constructing a piecewise continuous map, linear regions describing the motion between bursts were replaced by a single smooth curve (Fig. 1c). In this map, a burst is considered as terminated provided that spikes with minimum and maximum amplitudes in the intervals $[C_1, h_1]$ and $[h_2, 1]$, respectively, have been generated within this burst. The behavior of the system

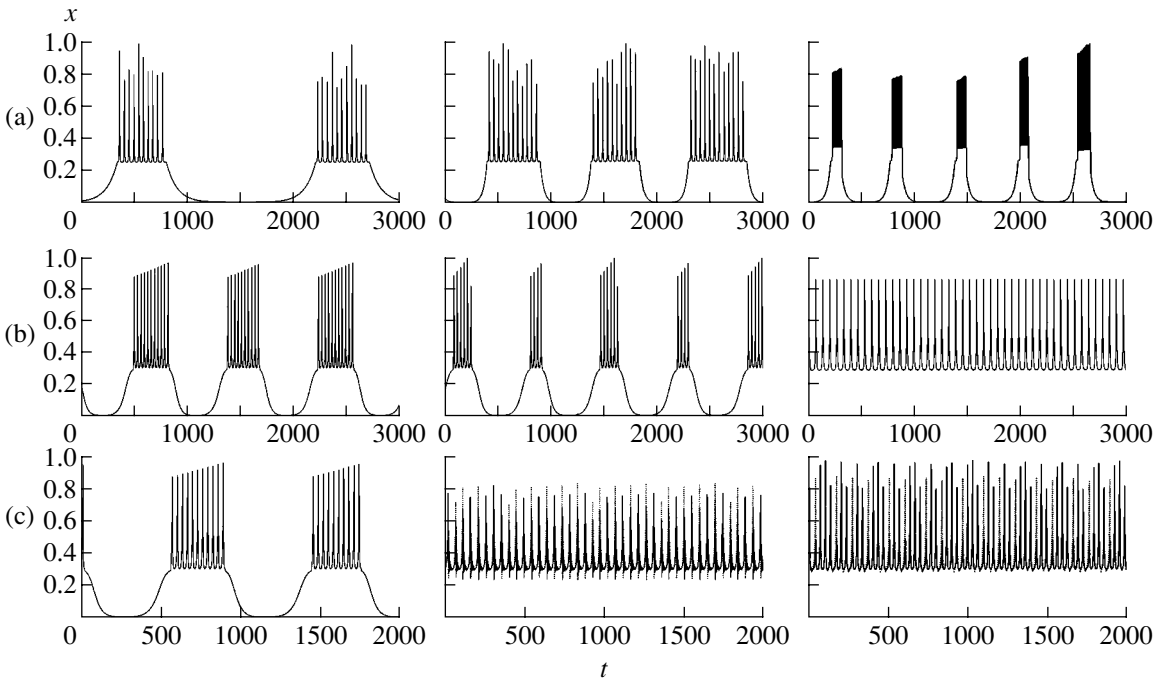

Fig. 2. Time series obtained by modeling the electric activity: (a) an isolated neuron in terms of a piecewise linear map ($A = 0.3$, $\beta = 0.3$, $\gamma = 1.6$, $\delta_1 = \delta_3 = 10^{-4}$, $N_s^0 = 10$) for $\alpha = 1.01$, $\delta_2 = 10^{-6}$ (left column), $\alpha = 1.03$, $\delta_2 = 10^{-6}$ (middle column), and $\alpha = 1.03$, $\delta_2 = 10^{-1}$ (right column); (b) an isolated neuron in terms of a piecewise continuous map ($A = 0.3$, $k_1 = 0.9$, $k_2 = 1.0$, $h_2 = 0.95$, $\delta_1 = 10^{-2}$, $\delta_3 = 10^{-3}$) for $\delta_2 = 10^{-3}$, $h_1 = 0.88$, $\gamma_1 = 1.4$, $\gamma_2 = 1.75$ (left column), $\delta_2 = 10^{-3}$, $h_1 = 0.88$, $\gamma_1 = 1.402$, $\gamma_2 = 1.75$ (middle column), and $\delta_2 = 10^{-4}$, $h_1 = 0.92$, $\gamma_1 = 1.3$, $\gamma_2 = 1.3$ (right column); (c) a pair of coupled neurons in terms of piecewise continuous maps ($A = 0.3$, $k_1 = 0.9$, $k_2 = 1.0$, $\gamma_2 = 1.75$, $\delta_1 = 10^{-2}$, $\delta_2 = 10^{-3}$, $\delta_3 = 10^{-3}$, $h_2 = 0.95$) for $\varepsilon = 0.50$, $\gamma_1 = 1.40$ (left column), $\varepsilon = 0.95$, $\gamma_1 = 1.70$ (middle column), and $\varepsilon = 0.24$, $\gamma_1 = 1.427$ (right column).

is described by the following variables: $x \in [0, 1]$ (the state variable); $d = -1$ or 1 (variable determining selection of the upper or lower branch of the mapping function); and s_1, $s_2 = \{0, 1\}$ ("switches" determining the conditions of burst termination).

The piecewise continuous map is defined by the following relations:

(i) $d = 1$ corresponds to an increase in the state variable x:

$$x' = \begin{cases} \alpha_1 \arctan(k_1 x), & x \in [0, A - \delta_1), \\ 2A - x, & x \in [A - \delta_1, A), \\ \gamma_1 (x - A) + A, & x \in [A, C_1); \end{cases} \quad (3)$$

(ii) $d = -1$ corresponds to a decrease in the state variable x:

$$x' = \begin{cases} \frac{1}{\gamma_2}(x - A) + A, & x \in [A + \delta_2, 1], \\ 2A - x, & x \in [A, A + \delta_2), \quad s_1 s_2 = 1, \\ \frac{1}{\alpha_2}\arctan(k_2 x), & x \in [\delta_3, A); \end{cases} \quad (4)$$

(iii) additional conditions: $d = -1$ for $x \in [C_1, 1]$; $d = 1$ for $x \in [A, a + \delta_2)$ and $s_1 s_2 = 0$, $s_1 = \{1, x \in [C_1, h_1]; 0, x \in [0, A]\}$; $s_2 = \{1, x \in [h_2, 1]; 0, x \in [0, A]\}$; $d = 1$ for $x \in [0, \delta_3)$. In Eqs. (3) and (4), the quantities A, k_1, k_2, γ_1, γ_2, δ_1, δ_2, δ_3, $C_1 = (1 - A)/\gamma_1 + A$, $\alpha_1 = A/\arctan(k_1 A)$, $\alpha_2 = A/\arctan(k_2 A)$, h_2, Δh, and $h_1 = C_1 + \Delta h$ are constant parameters.

Figure 2b presents time series obtained using the above piecewise continuous map. Using two such maps, it is possible to model the behavior of coupled neurons. The electric coupling can be described by analogy with that in the Rose–Hindmarsh model for two coupled neurons [1] with allowance for the threshold character of the interaction. The coupling is taken into account by adding the term $\varepsilon\Theta(x_2 - A)(x_1 - x_2)$ to the state variable x_1 of the first map and the term $\varepsilon\Theta(x_1 - A)(x_2 - x_1)$ to the state variable x_2 of the second map, where $\Theta(x)$ is the Heaviside step function and ε is the coupling parameter. The results of modeling of the behavior of two coupled neurons are presented in Fig. 2c. Note that the time series describing the behavior of an isolated neuron or a pair of coupled neurons in terms of the proposed maps are qualitatively similar to the patterns observed for a separate biological neuron and a pair of coupled biological neurons [7].

The proposed maps can be used for modeling the behavior of neuron ensembles. The approach to modeling neurons by using piecewise continuous maps, describing a neuron based on phenomenological notions, can be extended to modeling oscillatory processes in systems of various natures.

Acknowledgments. This study was supported by the Russian Foundation for Basic Research (project nos. 02-02-16351 and 00-15-96673), by the Ministry of Education of the Russian Federation (project no. E00-3.5-196), and by the US Civilian Research and Development Foundation (CRDF grant REC-006).

REFERENCES

1. G. D. I. Abarbanel, M. I. Rabinovich, A. Selverston, *et al.*, Usp. Fiz. Nauk **166**, 363 (1996).
2. M. I. Rabinovich, A. I. Selverston, L. Rubchinsky, *et al.*, Int. J. Bifurcation Chaos **6**, 288 (1996).
3. R. Huerta, Int. J. Bifurcation Chaos **6**, 705 (1996).
4. I. V. Belykh, Izv. Vyssh. Uchebn. Zaved. Radiofiz. **41**, 1572 (1998).
5. Y. Hayakawa and Y. Sawada, Phys. Rev. E **61**, 5091 (2000).
6. N. F. Rulkov, Phys. Rev. Lett. **86**, 183 (2001).
7. R. C. Elson, A. I. Selverston, R. Huerta, *et al.*, Phys. Rev. Lett. **81**, 5692 (1998).

Translated by P. Pozdeev

Technical Physics Letters, Vol. 29, No. 2, 2003, pp. 108–110. Translated from Pis'ma v Zhurnal Tekhnicheskoĭ Fiziki, Vol. 29, No. 3, 2003, pp. 53–57.

Effect of Cell Rotation Speed on Mutual Diffusion in a Three-Component Gas Mixture

Yu. I. Zhavrin, V. N. Kosov, D. U. Kul'zhanov, I. V. Poyarkov, and N. B. Ankusheva

Institute of Experimental and Theoretical Physics, Kazakh National University, Almaty, Kazakhstan

e-mail: zhavrin@physics.kz

Received July 17, 2002

Abstract—The effect of the circular frequency of a two-compartment rotary diffusion cell on mutual diffusion in a three-component gas mixture under conditions of equal gas density has been experimentally studied. It is established that an increase in the rotation speed leads to the transition from unstable mass transfer to stable molecular diffusion. *© 2003 MAIK "Nauka/Interperiodica".*

There are many factors and parameters known to influence the onset and development of a diffusion instability (i.e., instability of the mechanical equilibrium) in gas mixtures. Investigations of these phenomena showed that some effects can be employed in basic science and technology, in particular, for the enrichment of gas mixtures with desired components [1].

It is known that gravity is the main factor influencing convective flows arising in a gas mixture due to molecular diffusion of the mixture components. Previous experiments with mass transfer were performed under conditions where the acceleration of gravity was constant in both magnitude and direction. However, it can be expected that, if the acceleration vector periodically changes, the behavior of the opposite convective flows in an unstable diffusion process will probably differ from that observed in a constant gravity field.

Previously [2], we have studied the effect of oscillations on the onset and development of convection in the course of unstable diffusion processes in three-component gas mixtures. In particular, that investigation showed evidence of the small influence of the amplitude of low-frequency oscillations on the unstable diffusion process. Below, we report the results of experiments that reveal the effect of the circular frequency of a two-compartment rotary diffusion cell on the unstable diffusion process in a three-component gas mixture.

The mass transfer experiments were conducted in a two-compartment diffusion cell (see figure) comprising upper and lower vessels with equal volumes V_1 and V_2, respectively, connected by a diffusion channel with length L and diameter d. There were two experimental runs with the following system parameters: (1) $V_1 = V_2 = 70.0 \pm 0.5$ cm^3, $L = 68.3 \pm 0.1$ mm, $d = 10.00 \pm 0.01$ mm; (2) $V_1 = V_2 = 69.5 \pm 0.5$ cm^3, $L = 70.0 \pm 0.1$ mm, $d = 3.40 \pm 0.01$ mm. The average temperature was $\bar{T} = 293 \pm 0.5$ K, while the gas pressure was selected so as to provide for the maximum intensity of unstable mixing in both experiments: $P = 1.07$ (1) and 3.04 MPa (2).

The unstable diffusion process was studied in the (0.333He + 0.667Ar)–N_2 system with the binary mixture composition (indicated in molar fractions) selected so as to make its density comparable with that of nitrogen. For convenience, the upper vessel was always filled with the He–Ar binary mixture, while the lower vessel was charged with nitrogen. The binary mixture composition was determined using an ITR-1 interferometer. The gas mixture upon diffusion was analyzed using a Khrom-4 chromatograph equipped with a column filled with a 5-Å molecular sieve. The error of analysis did not exceed 0.3%.

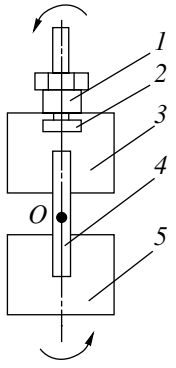

Schematic diagram of the experimental setup used to study the effect of rotation speed on the mass transfer in a two-compartment diffusion cell: (*1*) sealing gasket; (*2*) channel-blocking valve; (*3*) upper vessel; (*4*) diffusion channel; (*5*) lower vessel; (*O*) axis of rotation.

1063-7850/03/2902-0108$24.00 © 2003 MAIK "Nauka/Interperiodica"

Table 1. Effect of the rotation speed of the diffusion cell upon unstable mass transfer process in the (0.333He + 0.667Ar)–N_2 system

Circular frequency, Hz	Component transfer, mol. fraction						$\alpha = c_{exp}/c_{th}$		
	experiment			theory [3]					
	He	Ar	N_2	He	Ar	N_2	He	Ar	N_2
Experiment 1: d = 10 mm; diffusion time t_d = 1800 s									
0	0.128	0.257	0.385				2.32	9.18	4.64
0.5	0.076	0.242	0.318				1.38	8.64	3.83
1.0	0.066	0.218	0.284	0.055	0.028	0.083	1.20	7.79	3.42
2.0	0.054	0.150	0.204				0.98	5.36	2.46
2.6	0.052	0.063	0.115				0.95	2.25	1.39
3.6	0.048	0.053	0.101				0.87	1.89	1.22
Experiment 2: d = 3.4 mm; diffusion time t_d = 1800 s									
0.5	0.001	0.030	0.031	0.003	0.001	0.004	0.33	30.0	7.8
0.7	0.003	0.007	0.010				1.0	7.0	2.5
1.0 (t_d = 7200 s)	0.015	0.007	0.022	0.010	0.004	0.014	1.5	1.7	1.5

The experimental procedure was essentially as follows. The diffusion cell was filled with the gas components to the initial pressure, after which the gas admission valves were closed and the setup was disconnected from the gas preparation unit. Then, the rotary diffusion cell was fixed in a lathe chuck, the valve between vessels was opened, and the cell was rotated at a preset speed for a certain period of time measured with a chronometer. To terminate the experiment, the chuck was stopped and the valve between vessels was closed to block the channel. The results of these experiments are presented in Table 1.

As can be seen from the data in Table 1, the rate of unstable mass transfer is maximal in the absence of rotation (with the cell oriented vertically). This can be judged by the parameter α equal to the ratio of the experimental component concentrations to the theoretical values calculated assuming stable diffusion and using the Stefan–Maxwell equation [3]. Thus, $\alpha = 1$ corresponds to the case of stable diffusion. Should this parameter differ from unity, at least for one component, it can be ascertained that an instability is developed and convective flows arise in the system. Rotation of the diffusion cell results in the structural formations of various densities appearing in the system as a result of diffusion [4] being dissipated under the action of a gravitational force (periodically changing in direction) and the centrifugal force. These factors hinder the establishing of conditions favoring the formation of convective flows.

Thus, at a certain circular frequency, only flows characteristic of the molecular diffusion can exist in the rotary diffusion cell. This conclusion is confirmed by analysis of the data in Table 1 with respect to the transferred component concentrations and by variation of the parameter α. Note that a small difference of this value from unity in the vicinity of critical frequencies is quite reasonable. Since the opening and closure of the valve between vessels is not instantaneous (each operation takes about 15 s, which is comparable with the time required for the onset of convection), an insignificant amount of gases can be transferred by a nondiffusion mechanism.

The effect of the cell rotation speed was also traced for a usual binary diffusion in an He–Ar system,

Table 2. Effect of the cell rotation speed on the binary diffusion process in the He–Ar system (P = 1.96 MPa, $\bar{T}$ = 293 K, t_d = 1800 s, d = 3.4 mm)

Circular frequency, Hz	Component transfer, mol. fraction			
	experiment		theory [3]	
	He	Ar	He	Ar
0	0.085	0.085		
1.0	0.117	0.117	0.0130	0.0130
2.0	0.139	0.139		

although studying this situation is not quite correct. In the absence of rotation, experimental results for the ordinary diffusion in this system (with helium in the upper vessel and argon in the lower one) coincided with the calculated values. Upon changing orientation of the cell, the mixing process became convective (see the first line in Table 2, which also presents experimental data illustrating the effect of rotation on the gas mixing in this binary system). As can be seen from Table 2, an increase in the cell rotation speed (leading to the change from diffusive to convective mixing) favors an increase in the transfer of components. This result could be anticipated, considering the intensity of mass transfer by diffusion and convection in the rotating setup.

Thus, the results of our investigation show that the rotation speed of a two-compartment rotary diffusion cell significantly influences the character of structurized convective flows arising during unstable mixing in a three-component gas mixture. At a certain critical value of the circular frequency, the process changes from unstable diffusion to stable molecular mass transfer.

REFERENCES

1. V. N. Kosov, V. D. Seleznev, and Yu. I. Zhavrin, Zh. Tekh. Fiz. **67** (10), 139 (1997) [Tech. Phys. **42**, 1236 (1997)].
2. Yu. I. Zhavrin, V. N. Kosov, and D. U. Kul'zhanov, Vestnik Kazakh. Gos. Univ., Ser. Fiz. **7**, 151 (1999).
3. Yu. I. Zhavrin, N. D. Kosov, V. N. Kosov, *et al.*, Available from KazGosINTI, No. 6239 (Kazakh. Univ., Almaty, 1995).
4. Yu. I. Zhavrin, N. D. Kosov, S. M. Belov, and S. B. Tarasov, Zh. Tekh. Fiz. **54** (5), 943 (1984) [Sov. Phys. Tech. Phys. **29**, 561 (1984)].

Translated by P. Pozdeev

Technical Physics Letters, Vol. 29, No. 2, 2003, pp. 111–114. Translated from Pis'ma v Zhurnal Tekhnicheskoĭ Fiziki, Vol. 29, No. 3, 2003, pp. 58–64.

Optical Vortices in Crystals: Formation, Annihilation, and Decay of Polarization Ombilics

A. V. Volyar and T. A. Fadeeva

Tauride National University, Simferopol, Ukraine

Received August 9, 2002

Abstract—The field of polarization states of a paraxial Gaussian beam transmitted via two crystals with crossed optical axes exhibits phase perturbations on the side of the second crystal. These perturbations are manifested by the formation, annihilation, decay, and merging of some special field regions called ombilics. Placed behind the crystals, an analyzer of the circular polarization is capable of revealing single and bound optical vortices in such a field, thus providing a means of monitoring the movement of these vortices. © *2003 MAIK "Nauka/Interperiodica".*

A homogeneously polarized laser beam, either transmitted through a smoothly inhomogeneous medium or scattered from random inhomogeneities of the refractive index, always contains a finite number of special points forming characteristic patterns independent of the nature of the above inhomogeneities [1]. Previously [2], we have demonstrated that such special points of a vector field, called disclinations, play a decisive role in the formation of optical vortices in a beam that travels through a system comprising a uniaxial crystal, a quarterwave ($\lambda/4$) plate, and an analyzer. However, small perturbations typically present in real optical devices can violate the topological balance of the vector field involved in the vortex formation process and cause changes in the structure of this field. Thus, we are speaking essentially of the structural stability of the regions of a vector light field in the vicinity of the aforementioned special points.

Consider a paraxial light beam transmitted sequentially via two crystals with mutually perpendicular optical axes, the optical axis of the first crystal coinciding with the beam axis. The second crystal introduces a perturbation in the polarization state of the beam, which has the form of a phase difference Δ between local orthogonal components of the electric vector. At the exit from the first crystal, the beam is characterized by an inhomogeneous polarization in the cross section. By special points or lines in this polarization field, we imply regions surrounding the points (lines) with clockwise or counterclockwise circular polarization. Such regions can be divided into three groups of ombilics [1] termed (after J. Nye and M. Berry) "star," "lemon," and "monstar" (from "lemonstar," which implies an intermediate state between the former two). These singularities, representing structurally stable configurations of the wave field, exhibit certain evolution under the action of external perturbations.

The aim of this study was to describe the events of formation, annihilation, and decay of polarization ombilics as a result of a smooth perturbation related to a phase difference Δ introduced into the polarization field by the second crystal.

Let us write components of the Jones vector $\mathbf{q}_0$ of a circularly polarized light beam in the following form:

$$\begin{aligned} q_x &= \cos\delta/2[\cos\Delta/2 + i\sin\Delta/2\exp(i\sigma 2Q)] \\ &+ i\sin\delta/2\exp(i\sigma 2\varphi)[\cos\Delta/2 + i\sin\Delta/2\exp(-i\sigma 2Q)], \\ q_y &= i\sigma\{\cos\delta/2[\cos\Delta/2 - i\sin\Delta/2\exp(i\sigma 2Q)] \\ &- i\sin\delta/2\exp(i\sigma 2\varphi)[\cos\Delta/2 - i\sin\Delta/2\exp(-i\sigma 2Q)]\}. \end{aligned} \quad (1)$$

Here, $\delta = ar^2/\sqrt{r^2 + L^2}$ is the phase difference introduced by the first crystal, $r^2 = x^2 + y^2$, L is the thickness of the first crystal, Δn_1 is the differential refractive index of the first crystal, $a = k\Delta n_1$, k is the wave number, φ is the azimuthal coordinate, $\sigma = \pm 1$ is the beam helicity (the electric vector circulation direction in the primary wave), $\Delta \approx bH$, $b = k\Delta n_2$, H is the thickness of the second crystal, Δn_2 is the differential refractive index in the second crystal, and Q is the angle of orientation of the birefringence axis of the second crystal. In writing expressions (1), we omitted for brevity the factor $\Psi_{lm}(r, \varphi, z)$ characterizing the primary field, which is common for both components of the $\mathbf{q}_0$ vector:

$$\Psi_{lm} = (r/\Delta)^l L_m^{(l)}(2r^2/w^2)\exp[i(kl\varphi + \Gamma)]G,$$

where $G = 1/\Lambda\exp(-r^2/\rho^2\Lambda)$, $\Lambda = 1 - iz/z_0$, $w^2 = \rho^2(1 + z/z_0)$, $z_0 = k\rho^2/2$, $L_m^{(l)}(X)$ is the generalized Laguerre polynomial, $\Gamma = 2m\arctan(z/z_0)$ ($m = 0, 1, 2. 3, \ldots$ l is the topological charge of a singular beam, $\kappa = \pm 1$ is the sign of this charge, and ρ is the beam waist radius at $z = 0$).

1063-7850/03/2902-0111$24.00

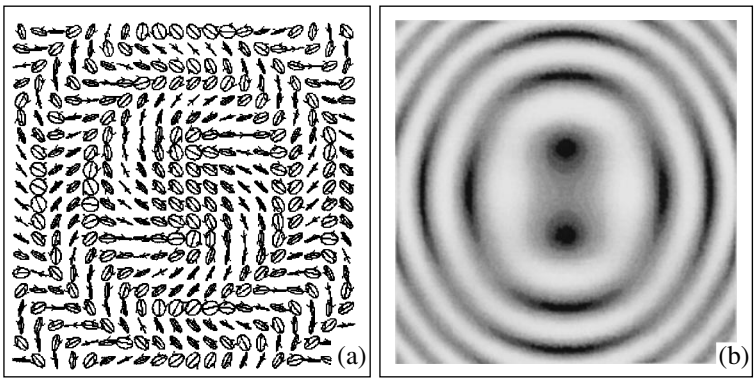

Fig. 1. (a) Schematic representation of the polarization distribution in the cross section of a paraxial Gaussian beam ($l = 0$) transmitted via two crystals with crossed optical axes, for a phase perturbation of $\Delta = \pi/6$ introduced by the second crystal; (b) polarization field intensity distribution past the circular polarization analyzer with the transmission axis oriented at $\alpha = 0$.

In order to analyze the polarization field structure of a beam with $l = 0$ past the second crystal, let us use the formalism of the Stokes parameters [3]. Without losing generality, we will consider the case of $Q = 0$. (Note that, owing to the axial symmetry of the polarization field past the first crystal, the case of $Q \neq 0$ corresponds to a synchronous rotation of all points past the second crystal by a certain angle.) In the paraxial approximation, dependence of the phase perturbation Δ on the beam divergence can be ignored. Using expression (1), the Stokes parameters can be written as follows:

$$S_0 = 1, \quad S_1 = -\sigma \sin\delta \sin 2\varphi,$$
$$S_2 = \sigma\{\sin\Delta\cos\delta + \cos\Delta\sin\delta\cos 2\varphi\}, \qquad (2)$$
$$S_3 = \sigma\{-\cos\Delta\cos\delta + \sin\Delta\sin\delta\cos 2\varphi\}.$$

Figure 1 shows a schematic representation of the polarization distribution in the intermediate case of $\Delta = \pi/6$. In this field, the ombilics are formed by the lines (level lines) tangent to one of the semiaxes of the polarization ellipse. In our case, it is sufficient to restrict the consideration to the behavior of the azimuthal angle ψ of the major semiaxis determined as $\tan 2\psi = S_2/S_1$. The level lines of the major semiaxis are described by the simple relation $dy/dx = \tan\varphi$, from which we obtain the differential equation

$$(dy/dx)^2 + 2(S_1/S_2)(dy/dx) - 1 = 0. \qquad (3)$$

Since the ombilics are formed in the vicinity of polarization singularities of the electromagnetic field, where $S_1(r, \varphi, \Delta) = S_2(r, \varphi, \Delta) = 0$, we will also seek the solutions to Eq. (3) in the vicinity of such singular points (lines).

First, let us assume that the perturbation is absent ($\Delta = 0$). Then differential equation (3) transforms to $dy/dt = -\sigma x + y$, $dx/dt = x + \sigma y$ (in writing this, we took into account that the orientation changes by $\pi/2$ when the helicity σ changes sign and that $\sin\delta \approx \delta \approx ar^2$). The solution of this equation has the form of spiral integral curves $r = r_0\exp(-\sigma\varphi)$ with a singularity of the "focus" type (Fig. 2, Ia). Following J. Nye, the singularity index s is determined by traversing the singularity on a closed contour and taking into account the number and direction of rotations of the polarization ellipse. In the case under consideration, we obtain $s_h = +1$. If the sign of helicity σ is changed to opposite, the direction of rotation of the branches of the spiral will reverse as well, but the index s will remain unchanged.

Now let us consider the case when the second crystal introduces a small perturbation ($\Delta \ll 1$) and find the form of the level lines near singularities for $\varphi = 0$ and π with slightly changed coordinates, assuming that $ar^2 \approx \Delta$. Expanding the Stokes parameters $S_1(r, \varphi)$ and $S_2(r, \varphi)$ into Taylor series in the vicinity of singularities and restricting the consideration to the first terms, we arrive at the equations $dr/rd\varphi = -\cot(\varphi/2)$ for the beam with $\varphi_0 = 0$ and $dr/rd\varphi = \tan(\varphi/2)$ for the beam with $\varphi_0 = \pi$. The corresponding solutions, $r = r_0/\sin^2(\varphi/2)$ and $r = r_0/\cos^2(\varphi/2)$, determine the level lines forming ombilics of the lemon type with equal topological indices $s_l = +1/2$. The shape of these ombilics is illustrated in Fig. 2 (Ib). Alteration of the helicity sign from $\sigma = +1$ to -1 synchronously changes the orientation of special directions in the symmetric ombilics (Fig. 2, II). This implies that a small perturbation introduced by the second crystal leads to a decay of the spiral degenerate ombilic into two singularities of the lemon type situated symmetrically relative to the axis, while the total topological index of these singularities $s_h = s_l + s_l$ remains unchanged.

Of special interest in our case are the structural transformations of the ring-shaped ombilic closest to the axis, the circular polarization of which is opposite to that of the axial singularity. An analysis of Eq. (1) shows that the main transformations take place along the beams with $\varphi = 0$, $\pi/2$, π, and $3\pi/2$, so that the radial coordinate is $ar^2 = \pi + \Delta$. In this case, Eq. (3) for $\varphi =$

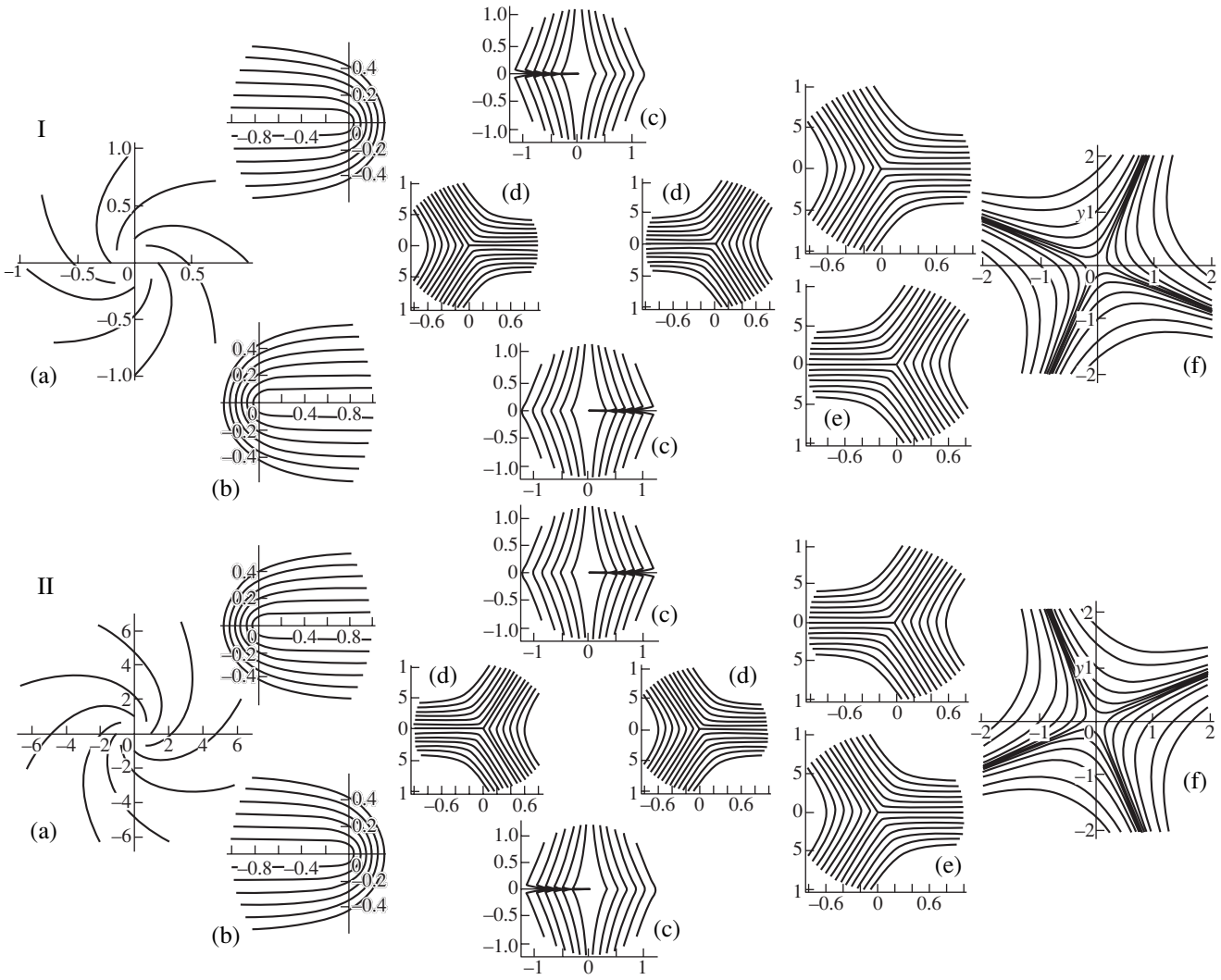

Fig. 2. Diagrams illustrating the formation, annihilation, decay, and merging of polarization ombilics as a result of the perturbation introduced by the second crystal for $\sigma = +1$ (I) and -1 (II): (a) degenerate spiral ombilic ($\Delta = 0$); (b) lemon type ombilics formed at the beam axis in the case of a small perturbation ($\Delta \ll 1$); (c, d) vector topological quadrupole comprising monstar and star ombilics, respectively; (e) star ombilics merging with the formation of an (f) degenerate hyperbolic ombilic for $\Delta = \pi$.

$\pi/2$ can be rewritten as $ydy/dx - Ax - \kappa\sqrt{Ax^2 + y^2} = 0$ (where $A = \Delta/(\pi + \Delta)$ and $\kappa = \pm 1$). Upon substituting $y = xu(x)$, this equation allows separation of variables ($\kappa = +1$ corresponds to $dy/dx > 0$, and $\kappa = -1$ to $dy/dx < 0$). The solutions of this equation,

$$Cx^4 = \left|(2Z - \kappa - \sqrt{1 + 4B})/(2Z - \kappa + \sqrt{1 + 4B})\right|^{-\frac{\kappa}{\sqrt{1+4B}}} \times (Z^2 - \kappa Z - B)$$

$$(Z = \sqrt{A^2 + (y/x)^2},\ B = A + A^2,\ C = \text{const}),$$

describe an ombilic of the monstar type with a special direction $\varphi = \pi/2$. A related ombilic on the $\varphi = 3\pi/2$ beam can be determined using an analogous procedure. At the same time, the $\varphi = 0$ and π beams give rise to two ombilics of the star type, thus forming a vector topological quadrupole (Fig. 2, Ic and Id). Note that the latter two ombilics are described by the equations $r = r_0/\sin^{2/3}(3\varphi/2)$ and $r = r_0/\cos^{2/3}(3\varphi/2)$, respectively.

New ombilics of the two types possess opposite topological indices: $s_s = -1/2$ (for the star type) and $s_m = +1/2$ (for the monstar type). The overall topological index of both the vector topological quadrupole and the degenerate ring-shaped ombilic is zero: $s_s + s_m = 0$.

As the magnitude of the perturbation Δ grows (Fig. 2, Ie), two ombilics of the star type approach one another along the $\varphi = 0$ and π beams, whereas the two lemons are displaced out to the periphery along the $\varphi = \pi/2$ and $3\pi/2$ beams (during this, the lemons gradually deform and convert into monstars). When the perturbation increases to $\Delta \propto \pi$, the two symmetric stars merge into one degenerate ombilic centered at the axis. In this

case, Eq. (3) shows that the level lines obey the equation $\{x - (\sqrt{2} - \sigma)y\}\{x + (\sqrt{2} + \sigma)y\} = C$ possessing a singularity of the saddle point type. These lines represent a family of hyperbolas with mutually perpendicular asymptotes rotated by $\alpha = \pi/8$ relative to the ordinate axis (Fig. 2, Ie). This degenerate ombilic has a topological index of $s_H = -1$. At the same time, the two peripheral ombilics (having turned monstars) and the two stars (formed by the second ring disclination counting from the center) annihilate with the formation of a degenerate ring ombilic with a topological index $s_R = 2s_s + 2s_m$.

Thus, the phase perturbation introduced by the second crystal gives rise to the sequential events of decay, merging, transformation, and annihilation of the polarization ombilics. Since an ombilic with clockwise (counterclockwise) circular polarization at the axis can be considered as a dislocation of the wave front of the counterclockwise (clockwise) circularly polarized beam, an analyzer of circular polarization can always reveal an optical vortex as illustrated in Fig. 1b. From this standpoint, the phase perturbation introduced by the second crystal allows us to monitor the linear motions of both single vortices and those bound in scalar topological quadrupoles appearing as a result of the polarization filtration of the field of vector quadrupoles.

REFERENCES

1. J. F. Nye, *Natural Focusing and Fine Structure of Light Caustics and Wave Dislocations* (Institute of Physics Publishing, Bristol, 1999).
2. A. V. Volyar, T. A. Fadeeva, and Yu. A. Egorov, Pis'ma Zh. Tekh. Fiz. **28** (22), 70 (2002) [Tech. Phys. Lett. **28**, 958 (2002)].
3. R. M. Azzam and N. M. Bashara, *Ellipsometry and Polarized Light* (North-Holland, Amsterdam, 1977; Mir, Moscow, 1981).

Translated by P. Pozdeev

Technical Physics Letters, Vol. 29, No. 2, 2003, pp. 115–118. Translated from Pis'ma v Zhurnal Tekhnicheskoĭ Fiziki, Vol. 29, No. 3, 2003, pp. 65–73.

Low-Threshold-Current 1.2–1.5 μm Laser Diodes Based on AlInGaAs/InP Heterostructures

S. O. Slipchenko, A. V. Lyutetskiĭ, N. A. Pikhtin, N. V. Fetisova, A. Yu. Leshko, Yu. A. Ryaboshtan, E. G. Golikova, and I. S. Tarasov

Ioffe Physicotechnical Institute, Russian Academy of Sciences, St. Petersburg, Russia

SigmaPlus Company, Moscow, Russia

e-mail: nike@hpld.ioffe.rssi.ru

Received September 12, 2002

Abstract—Separate confinement AlInGaAs/InP multiwell laser heterostructures emitting in a wavelength range of 1.2–1.5 μm have been synthesized by metalorganic vapor-phase epitaxy. The threshold current of laser diodes with a strip width of 4.5 μm and a cavity length of 200 μm was as low as 10 mA. With a cavity length of 1.0 mm, the threshold current density was 500–650 A/cm^2. The laser diodes can operate in a continuous regime without forced cooling at an ambient temperature of up to 170°C. In a temperature range from 10 to 80°C, the characteristic temperature parameter T_0 reached up to 110 K. © *2003 MAIK "Nauka/Interperiodica".*

Laser diodes emitting in a wavelength interval of 1.2–1.5 μm possess a rather broad spectrum of applications [1]. In particular, these devices are used in local fiber-optic communication lines. The required output power being as low as several milliwatts, the main working characteristic of laser diodes for these applications is the threshold current. Another significant advantage of such laser diodes is the ability to operate without forced cooling. Therefore, high temperature stability of the output characteristics is also among the most important requirements.

Problems pertaining to the temperature dependence of the radiative characteristics of laser diode heterostructures based on solid solutions of the InGaAsP system, as well as the possibilities of optimizing the parameters of such heterostructures to ensure maximum temperature stability of their working characteristics, have been extensively studied [2–7]. It must be noted that the requirements to the optimum parameters of heterostructures for the laser diodes possessing maximum output power and minimum threshold current are contradictory [8]. This study is devoted to low- threshold-current laser diodes.

One of the factors determining the temperature sensitivity of the threshold current in heterostructures for lasers emitting at 1.3 μm is the Auger recombination process in the active region. In addition, the high temperature dependence of the parameters of laser diodes based on solid solutions of the InGaAsP system is related to poor electron confinement, since the conduction band accounts for only 1/3 of the total difference between the bandgaps [9, 10]. For this reason, maximum values of the characteristic temperature parameter T_0 for InGaAsP/InP based laser diodes with a quantum-confined active region are about 80 K [11]. To all appearances, reaching higher T_0 values with heterostructures of this system is problematic.

We have studied heterostructures based on the AlInGaAs/InP system [1, 12, 13] as an alternative to the InGaAsP/InP system which, provides for the obtaining of laser diodes emitting in the 1.3–1.8 μm wavelength interval. The main advantage of the new system is the possibility to increase the depth of the potential well for electrons. This possibility is related to the fact that the conduction band accounts for 2/3 of the total bandgap difference between the wide- and narrow-bandgap semiconductors in this heterostructure [12, 13]. In addition, the maximum bandgap width of a solid solution isoperiodic with InP in this system amounts to 1.47 eV. This factor also favors a better confinement of charge carriers in the quantum well [13].

We used the method of metalorganic-hydride vapor-phase epitaxy (MOVPE) to grow heterostructures of two types. The samples of type I comprised a 500-Å-thick wide-bandgap AlInAs emitter, an AlInGaAs-grad waveguide with a total thickness of 0.15 μm, and four 50-Å-thick AlInGaAs stressed quantum wells (SQWs) separated by AlInGaAs barrier layers. The heterostructures of type II differed from the former ones only in that the number of SQWs was increased to six. After MOVPE synthesis, the heterostructures were processed by the standard method [11] to form mesastrips with a width of W = 4–4.5 μm, provided with the necessary ohmic contacts, and divided into laser diode chips. Finally, the laser diodes were mounted on copper heat exchangers and fixed with the aid of an indium-based solder.

1063-7850/03/2902-0115$24.00 © 2003 MAIK "Nauka/Interperiodica"

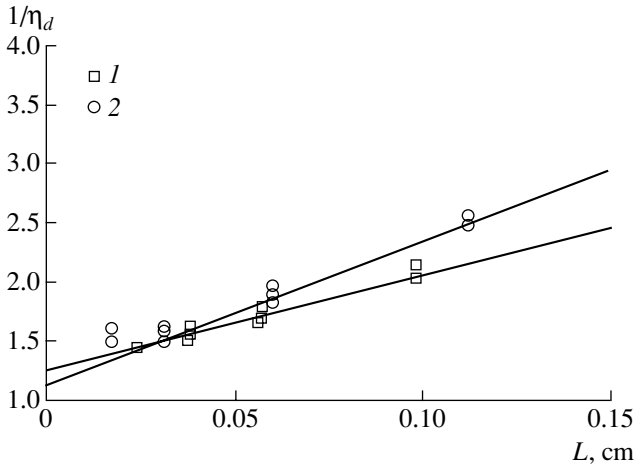

Fig. 1. The plots of experimental inverse differential quantum efficiency $1/\eta_d$ versus cavity length L for laser diodes based on the AlInGaAsP/InP heterostructures of the first (*1*) and second (*2*) types.

The laser diode samples were studied by measuring their output power–current (*P–I*) characteristics. These data were used to determine the differential quantum efficiencies and threshold current densities. Figure 1 shows the experimental plots of inverse quantum efficiency ($1/\eta_d$) versus the cavity length for laser diodes based on heterostructures of the two types studied. The values of internal optical losses determined from these dependences for the heterostructures of types I and II amounted to 8 and 13 cm^{-1}, respectively. As can be seen, an increase in the number of SQWs leads to a growth in the internal optical losses. This can be related to the light scattering from inhomogeneities on the SQW heteroboundaries and to an increase in the volume of the active region with a threshold carrier density.

In order to demonstrate the possibilities of heterolaser structures based on the AlInGaAs/InP solid solution system, we measured the *P–I* characteristics at various heat sink temperatures. It should be emphasized that these experiments were performed without using standard means of maintaining the heat sink temperature constant in the entire range of pumping currents. The heat sink with a laser diode being studied was mounted on a copper plate equipped only with a heater, while the standard system of temperature stabilization ensuring the removal of excess heat was absent. The heater was used to set a certain initial temperature prior to the measurement, which was monitored by a thermocouple attached to the edge of the laser diode. As the pumping current was increased, the heat sink temperature (indicated by the thermocouple) grew as well. For example, in the test with an initial temperature of 20°C set in the absence of the pumping current, the heat sink temperature at a current corresponding to the maximum output power increased by 5°C.

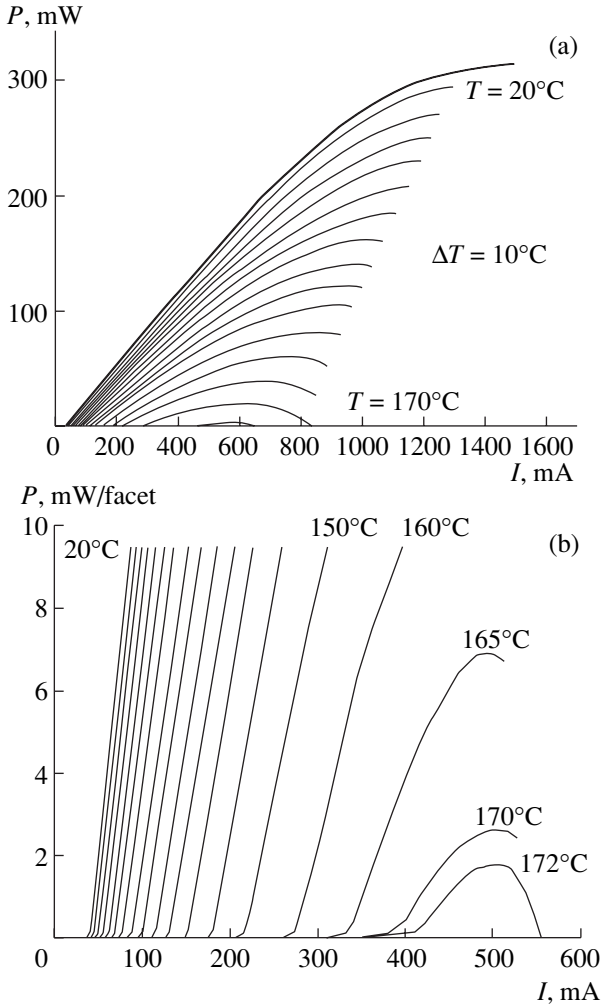

Fig. 2. The families of output power versus current curves measured in the continuous operation mode: (a) for a laser diode based on the heterostructure of type I with a cavity length of L = 1120 μm and with high-reflection (95%) and antireflection (5%) coatings on the resonator edges (heat sink temperature varied from 20 to 170°C with 10°C steps); (b) for a laser diode based on the heterostructure of type II with a cavity length of L = 1040 μm and with natural mirrors on the resonator edges (heat sink temperature varied from 20 to 160°C with 10°C steps).

Figure 2a shows a family of the *P–I* curves obtained for a laser diode with four SQWs (type I). These data demonstrate the possibility of lasing in a continuous regime at a heat sink temperature of up to 170°C, in contrast to laser diodes with the same parameters based on the classical solid solution system (InGaAsP/InP), for which this maximum temperature is 130°C [2]. It should be emphasized that the test heterostructures were not optimized from the standpoint of reaching a maximum output power. The maximum output power of our samples studied in the continuous regime was 300 mW, and this is not a limiting value. The results of analogous measurements performed by the same scheme for diode lasers based on heterostructures of

type II showed the possibility of continuous lasing at a heat sink temperature of up to 173°C (Fig. 2b).

Figure 3 presents the plots of threshold current density versus inverse length of the laser diode resonator. The experimental data showed that the threshold current density per quantum well (calculated with allowance for the internal quantum yield of induced emission [14]) in laser diodes with cavity lengths of 1000 and 400 μm amounts to 125 and 178 A/cm^2, respectively, for the heterostructure of type I and to 110 and 130 A/cm^2, respectively, for the samples of type II. These results indicate that the SQWs of heterostructures of the second type are characterized by a lower average threshold charge carrier density despite higher internal optical losses. This is related to the effect of gain saturation observed in the heterolasers with active regions on quantum wells, which is manifested in the logarithmic dependence of the gain on the carrier density of the quantum well [14].

The above example shows that a difference between the threshold carrier densities in the active regions (SQWs) of laser diodes based on the heterostructures of types I and II quite rapidly increases with the cavity length. Thus, our results indicate that an increase in the number of quantum wells increases the thermal stability of laser diodes, which has to be taken into account in the design of particular laser heterostructures. However, the number of SQWs has natural limitations. The main factor is the increase in optical losses, which cannot be eliminated at the existing technological level.

In order to eliminate the risk of overheating in the active region relative to the heat sink, we have employed lasing in the pulsed mode. As is known, the characteristic temperature parameter T_0 for laser diodes based on the classical solid solution system (InGaAsP/InP) does not exceed 80 K for devices operating in the temperature interval 10–80°C [11]. The results of our measurements showed that the AlInGaAs/InP solid solution system provides for a higher value of T_0. Indeed, the laser diodes implementing the heterostructures of types I and II with cavity lengths ranging from 500 to 1200 μm possessed the characteristic temperature parameter T_0 within 90–105 and 90–110 K, respectively.

The decrease in the temperature sensitivity of heterostructures with a greater number of quantum wells is probably explained by the aforementioned lower average threshold carrier density in the SQW. One of the factors favoring an increase in the thermal stability of the threshold current can be related to the enhanced electron confinement in SQWs, which decreases the thermal injection of free charge carriers from the active region to the waveguide layer. For a more complete analysis of the temperature dependence of the properties of laser diodes based on solid solutions of the AlInGaAs/InP system, it is necessary to take into account the process of nonradiative Auger recombination, since this process, together with the aforementioned thermal injection, determines the temperature sensitivity of the radiative characteristics of laser diodes.

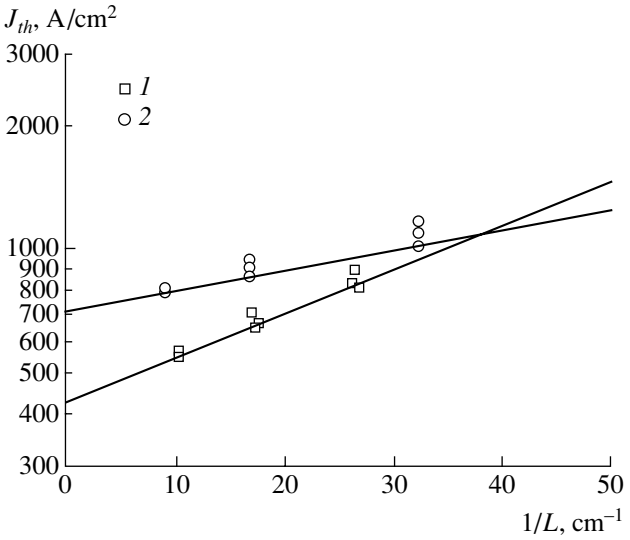

Fig. 3. The plots of experimental threshold current density J_{th} versus cavity length L for laser diodes with a strip width W = 4.5 μm based on the AlInGaAsP/InP heterostructures of the first (*1*) and second (*2*) types.

The results of investigation of the far field patterns for laser diodes based on the heterostructures of types I and II showed evidence of a stable zeroth mode generation in the plane perpendicular to the *p–n* junction, with an FWHM of 38°. In the plane parallel to the *p–n* junction, the far field exhibited a single-lobe character in the entire range of working currents, with an FWHM of 10–15°.

Thus, we have obtained low-threshold-current diode lasers of mesastrip design based on heterostructures of the AlInGaAs/InP solid solution system synthesized by MOVPE. It was demonstrated that the heterolasers are capable of operating in the continuous mode at a heat sink temperature of up to 170°C, which is unattainable for the lasers based on the classical solid solution system (InGaAsP/InP). The new laser diodes are characterized by a characteristic temperature parameter T_0 ranging from 90 to 110 K, which is evidence of a significantly higher thermal stability. The threshold current densities of the laser diodes being studied did not exceed the values reported previously for lasers based on the InGaAsP/InP heterostructures.

REFERENCES

1. C. Zah, R. Bhat, B. N. Pathak, *et al.*, IEEE J. Quantum Electron. **QE-30**, 511 (1994).
2. H. Temkin, D. Coblentz, R. A. Logan, *et al.*, Appl. Phys. Lett. **62**, 2402 (1993).
3. A. A. Bernussi, H. Temkin, D. L. Coblentz, and R. A. Logan, Appl. Phys. Lett. **66**, 67 (1995).

4. S. Seki, H. Oohasi, H. Sugiura, *et al.*, Appl. Phys. Lett. **67**, 1054 (1995).
5. G. G. Zegrya, N. A. Pikhtin, G. V. Skrynnikov, *et al.*, Fiz. Tekh. Poluprovodn. (St. Petersburg) **35**, 1001 (2001) [Semiconductors **35**, 962 (2001)].
6. G. L. Belenky, D. V. Donetsky, C. L. Reynolds, *et al.*, IEEE Photonics Technol. Lett. **9**, 1558 (1997).
7. L. V. Asryan, N. A. Gunko, A. S. Polkovnikov, *et al.*, Semicond. Sci. Technol. **15**, 1131 (2000).
8. B. B. Elenkrig, S. Smetona, J. G. Simmons, *et al.*, J. Appl. Phys. **85**, 2367 (1999).
9. S. Adachi, *Physical Properties of III–V Semiconductor Compounds* (John Wiley, 1992).
10. A. Yu. Leshko, A. V. Lyutetskiĭ, N. A. Pikhtin, *et al.*, Fiz. Tekh. Poluprovodn. (St. Petersburg) **34**, 1457 (2000) [Semiconductors **34**, 1397 (2000)].
11. E. G. Golikova, V. A. Gorbylev, Yu. V. Il'in, *et al.*, Pis'ma Zh. Tekh. Fiz. **26** (7), 57 (2000) [Tech. Phys. Lett. **26**, 295 (2000)].
12. Y. Sugiyama, T. Inata, T. Fujii, *et al.*, Jpn. J. Appl. Phys. **30**, L648 (1986).
13. I. Vurgaftman, J. R. Meyer, and L. R. Ram-Mohan, J. Appl. Phys. **89**, 5815 (2001).
14. N. A. Pikhtin, S. O. Slipchenko, Z. N. Sokolova, and I. S. Tarasov, Fiz. Tekh. Poluprovodn. (St. Petersburg) **36**, 364 (2002) [Semiconductors **36**, 344 (2002)].

Translated by P. Pozdeev

Technical Physics Letters, Vol. 29, No. 2, 2003, pp. 119–121. Translated from Pis'ma v Zhurnal Tekhnicheskoĭ Fiziki, Vol. 29, No. 3, 2003, pp. 74–81.

Extraction Equilibria in a Fullerene-Containing C_{60}–C_{70}–*o*-Xylene–*i*-Butylamine–Water System

O. V. Arapov, N. A. Charykov, V. I. Seregin, K. V. Nekrasov, V. I. Gerasimov, K. B. Strel'nikov, A. A. Pronkin, and V. V. Klepikov

St. Petersburg State Technological Institute (Technical University), St. Petersburg, Russia

Received April 22, 2002

Abstract—Extraction equilibria of the liquid(I)–liquid(II) type have been studied for the first time in a system containing light fullerenes C_{60} and C_{70}. The experiments were performed with a five-component mixture of fullerene C_{60}, fullerene C_{70}, *o*-xylene, *i*-butylamine, and water at 25°C. Isothermal diagrams describing the distribution of fullerene components between separating liquid phases have been obtained. The distribution coefficients of fullerenes (C_{60} and C_{70} concentrations in the xylene phase relative to those in the amine phase) are found to be almost constant and approximately equal to ~16.1 for both C_{60} and C_{70}. © *2003 MAIK "Nauka/Interperiodica".*

Introduction. A fullerene soot, containing from several units to a few dozens mass per cent of C_{60} and C_{70} molecules, is usually synthesized by a method based on the electric-arc erosion of graphite electrodes in a helium atmosphere under low-temperature plasma conditions. After synthesis, the fullerene mixture is isolated from soot by extraction with carbon sulfide, toluene, or (for the most part) *o*-xylene. The separation and purification of fullerenes under commercial conditions are performed almost exclusively by chromatographic techniques. These labor-intensive processes are mostly responsible for the relatively high cost of commercial fullerenes. This circumstance makes the search for alternative methods capable of providing effective separation and purification of fullerenes important.

This study is aimed at a verification of the principal possibility of using extraction methods based on the two-phase equilibria of the liquid(I)–liquid(II) type for the separation and purification of fullerene soot components. To the best of our knowledge, no investigations of such equilibria in fullerene-containing systems have been reported so far.

Formulation of the system. In order to solve the main task, it was necessary to select a system meeting the following requirements.

(1) The main components (solvents) of the system must possess a phase separation diagram containing a sufficiently broad concentration range of immiscibility in which the physicochemical properties of the coexisting phases significantly differ so as to provide sufficiently large coefficients of distribution of the fullerene components between separating solvent phases.

(2) For technological purposes, it is extremely important that the solubility of fullerenes C_{60} and C_{70} in both equilibrium phases be sufficiently large (not less than 50–100 mg of fullerenes per liter of solution).

(3) It is desired that solvents do not form overly strong compounds (such as charge-transfer complexes in compounds of C_{60} and C_{70} with anthracene) with dissolved fullerenes. In any case, either the formation of such complexes must be reversible or these compounds have to decompose readily with the liberation of pure fullerene components.

An analysis of published data on the solubility of C_{60} and C_{70} in various individual solvents (see, e.g., [1–5]) showed that the class of such media is rather restricted. This class includes aromatic hydrocarbons (benzene, toluene, some of xylenes); halogen-substituted derivatives of benzene, naphthalene, anthracene, and phenanthrene; heterocyclic compounds (e.g., pyridine); inorganic solvents, including CS_2, CCl_4, and CHI_3; some amines; decalin; and a few others. Reference data on the phase equilibria of the liquid(I)–liquid(II) type [6] indicate that most of the pairs of solvents selected from the above list are miscible in arbitrary proportions in the region of room temperature. On the other hand, when the state of a phase separation is achievable (e.g., as in anthracene-based mixtures at elevated temperatures), the resulting phases are characterized by irreversibly formed strong complexes of fullerenes with solvents.

Upon preliminary analysis, we selected two solvents as macrocomponents of the extraction system. These were *o*-xylene and *i*-butylamine, which readily dissolve fullerenes C_{60} and C_{70} (up to several grams per liter of solvent at 25°C) and exhibit absolute miscibility (mutual solubility). As the third component, we selected water (H_2O), which is virtually insoluble in *o*-xylene (~0.015 mass % at 25°C [6]) but miscible with

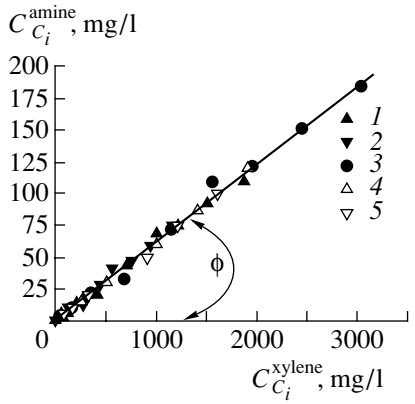

Fig. 1. The equilibrium diagram of the distribution of fullerenes C_{60} and C_{70} between the amine and xylene phases 14 days after mixing at 25°C (see the text for explanations): (*1*) C_{60}, (*2*) C_{70}, and (*3*) $C_{60} + C_{70}$ in C_{60}–C_{70}–*o*-xylene–*i*-butylamine–H_2O system; (*4*) C_{60} in C_{60}–*o*-xylene–*i*-butylamine–H_2O system; (*5*) C_{70} in C_{70}–*o*-xylene–*i*-butylamine–H_2O system.

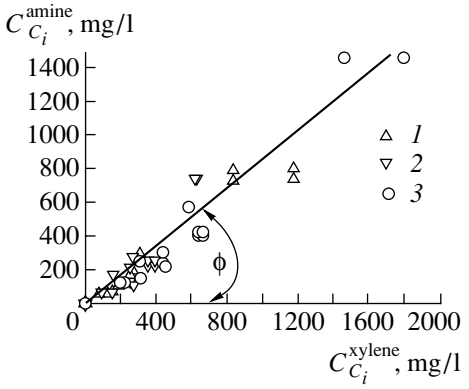

Fig. 2. The dynamic nonequilibrium diagram of the distribution of fullerenes C_{60} and C_{70} between the amine and xylene phases 24 h after mixing in C_{60}–*o*-xylene–*i*-butylamine–H_2O, C_{70}–*o*-xylene–*i*-butylamine–H_2O, and C_{60}–C_{70}–*o*-xylene–*i*-butylamine–H_2O systems at 25°C; (*1*) C_{60}; (*2*) C_{70}; (*3*) $C_{60} + C_{70}$.

i-butylamine in arbitrary proportions, thus providing excellent possibilities for the phase separation.

Experimental. First, the separating liquid phases were prepared by mixing *o*-xylene *i*-butylamine, and H_2O was taken in a volume ratio of 2 : 2 : 0.6, followed by treating in a shaker for 3 h at room temperature. Then the system was allowed to stand until phase separation. The bottom (predominantly amine) phase was used to prepare the solutions of various amounts of individual fullerenes C_{60} and C_{70}, as well as a fullerene solid solution with the composition $(C_{60})_{0.61}(C_{70})_{0.39}$. The latter compound was preliminarily synthesized at 80°C as described in [7]. Strictly speaking, this solid solution is unstable with respect to diffusion and actually represents a heterogeneous mixture of two solid solutions, $(C_{60})_{0.21}(C_{70})_{0.79}$ and $(C_{60})_{0.82}(C_{70})_{0.18}$, obtained by isothermal evaporation of a nonvariant eutonic solution [7]. Finally, aliquots of the top (predominantly xylene) phase were added to aliquots of the bottom phase with dissolved fullerenes, the resulting heterogeneous mixtures were treated in a shaker for 6 h at 25 ± 0.1°C, and kept in a thermostat for 14 days at the same temperature. Aliquots of the coexisting phases were used for analysis.

An analysis of the separated phases for the content of fullerene components, C_{60} and C_{70}, was performed as follows. The samples were evaporated to dryness at 80 ± 5°C under reduced pressure (10 Torr). The dry residues were dissolved in aliquots of *o*-xylene. The concentrations of C_{60} and C_{70} in these solutions were determined spectrophotometrically, by measuring the optical densities of solutions at the characteristic wavelengths $\lambda_1 = 335.7$ nm and $\lambda_2 = 472.0$ nm [8]. Concentrations of the solvent macrocomponents (*o*-xylene, *i*-butylamine, and water) in the coexisting phases were determined by chromatography.

It is necessary to consider one point in more detail. Immediately after preparation by mixing in a shaker, the separating phases take the form of emulsions intensively scattering light in the visible spectral range. Upon standing for the first 4–6 h, the mixtures exhibited visually complete separation of liquid phases, whereby the light scattering in the visible range vanished and that in the near UV range (at $\lambda \approx 360$ nm) somewhat decreased. The latter scattering effect was retained for several days, which was evidence of a significant inhomogeneity (and the nonequilibrium character) of the coexisting phases. The results of small-angle X-ray scattering (SAXS) measurements also confirmed the presence of microscopic (5–30 nm in size) inhomogeneities in these phases over 2–3 days (SAXS measurement were performed as described in detail elsewhere [9, 10]).

According to the spectroscopic data, neither fullerene molecules in solutions nor solvent components can form such giant aggregates [9, 10], and, hence, we can only suggest that liquid phases of the system being studied may contain microcolloidal particles exhibiting slow degradation. The transition of fullerenes into the *o*-xylene phase (until reaching stationary concentrations) was observed over the first 10 days. For comparison, Figs. 1 and 2 show an equilibrium diagram of the distribution of fullerenes C_{60} and C_{70} obtained after 14 days and a dynamic nonequilibrium diagram obtained the day after mixing. As can be seen, the two diagrams are sharply distinct, the distribution coefficients differing almost by one order of magnitude (the latter diagram also shows a large scatter of points).

Discussion of results. Chromatographic analysis of the coexisting phases for the content of the main solvent components (*o*-xylene, *i*-butylamine, and water) gave the following results. Amine phase (mass %):

$C_{o\text{-}C_6H_4(CH_3)_2} \approx 34.6$; $C_{i\text{-}C_4H_9NH_2} \approx 42.0$; $C_{H_2O} \approx 23.4$. Xylene phase (mass %): $C_{o\text{-}C_6H_4(CH_3)_2} \approx 85.3$; $C_{i\text{-}C_4H_9NH_2} \approx 10.2$; $C_{H_2O} \approx 4.5$. With respect to these components, the phase compositions are virtually independent of the content of fullerenes. This result is by no means surprising, since the fullerene solutions in both phases are highly diluted.

The content of macrocomponents in the coexisting phases is most conveniently controlled by increasing or decreasing the content of water in the primary heterogeneous solvent mixture. Adding even a few volume fractions of water to this mixture leads to a sharp redistribution of components (water passes almost completely to the amine phase). As a result, the liquid(I)–liquid(II) nodes are elongated, differences in the physicochemical properties grow, and the total phase separation time decreases. However, adding water leads to a critical decrease in the solubility of fullerenes C_{60} and C_{70} in the amine phase (while their solubility in the xylene phase remains virtually unchanged), and the distribution coefficients begin to grow sharply (reaching hundreds and thousands relative units). The reverse process (decrease in the total H_2O content) leads to the opposite results: the liquid(I)–liquid(II) nodes shorten and the differences in properties between phases rapidly disappear. As the water content decreases further (e.g., to 15–20 vol %), the system represents a homogeneous mixture (which corresponds to crossing the isothermal-isobaric separation binodal [11]). A decrease in the node length, in turn, leads to a sharp drop in the distribution coefficients for C_{60} and C_{70} (down to unity at the critical separation point [11]). However, the total phase separation time dramatically increases and the phases do not separate even after standing for several months.

Figure 1 shows the diagram of the distribution of fullerenes C_{60} and C_{70} (in milligrams per liter of solution) at 25°C between the amine and xylene phases for the four-component systems C_{60}–*o*-xylene–*i*-butylamine–H_2O and C_{70}–*o*-xylene–*i*-butylamine–H_2O and the five-component system C_{60}–C_{70}–*o*-xylene–*i*-butylamine–H_2O. The concentrations of macrocomponents (*o*-xylene, *i*-butylamine, and water) and the total content of fullerenes $C_{60} + C_{70}$ (in the five-component system) were fixed.

As can be seen, the diagrams appear (rather unexpectedly) very simple, representing straight lines over the entire concentration range studied (although the content of fullerenes was varied by a factor of almost 100). The distribution coefficients of fullerenes (C_{60} and C_{70} concentrations in the xylene phase relative to those in the amine phase) are found to be almost constant and approximately equal for both C_{60} and C_{70}, amounting to $K_{distr} \approx 16 \pm 5$ rel. units. This value was observed irrespective of whether one of the fullerenes or both were present in solution, which implies that these fullerene molecules exhibit no competition during the extrication process (i.e., C_{60} and C_{70} are extracted independently of each other). The fact of equal distribution coefficient during the extraction is evidence of the impossibility of separating fullerenes C_{60} and C_{70} by extraction in the C_{60}–C_{70}–*o*-xylene–*i*-butylamine–water system.

Acknowledgments. This study was supported by the Presidential Grant Council (project no. 00-15-99334).

REFERENCES

1. N. Sivaraman, R. Dhamodaran, I. Kalliapan, *et al.*, J. Electrochem. Soc. (Recent Adv. Chem. Phys. Fuller. Relat. Mater., Ed. by R. S. Rouff) **94** (24), 156 (1994).
2. N. D. Kushch, I. Majchrzak, W. Ciesielski, *et al.*, Chem. Phys. Lett. **215**, 317 (1993).
3. X. Zhou and Z. Gu, Chin. Bull. **38**, 175 (1993).
4. X. Zhou, Z. Gu, J. Wu, *et al.*, Carbon **32**, 935 (1994).
5. N. Ceolin, V. Agafonov, D. Andre, *et al.*, Chem. Phys. Lett. **208**, 259 (1993).
6. P. B. Smite, *Liquid-Liquid Phase Equilibria* (Plenum Press, New York, 1976), Vols. I–III.
7. A. N. Ponomarev, B. M. Aksel'rod, N. A. Charykov, *et al.*, Zh. Fiz. Khim. **74**, 2031 (2000).
8. A. N. Ponomarev, M. E. Yudovich, N. A. Charykov, *et al.*, Opt. Spektrosk. **88**, 230 (2000) [Opt. Spectrosc. **88**, 195 (2000)].
9. V. V. Golubkov, B. A. Shakhmatkin, N. A. Charykov, *et al.*, Zh. Fiz. Khim. **75**, 1819 (2001).
10. V. V. Golubkov, B. A. Shakhmatkin, N. A. Charykov, *et al.*, Zh. Fiz. Khim. **76**, 561 (2002).
11. A.V. Storonkin, *Thermodynamics of Heterogeneous Systems* (Len. Gos. Univ., Leningrad, 1967, 1969), Vols. I–III.

Translated by P. Pozdeev

Technical Physics Letters, Vol. 29, No. 2, 2003, pp. 122–124. Translated from Pis'ma v Zhurnal Tekhnicheskoĭ Fiziki, Vol. 29, No. 3, 2003, pp. 82–88.

Recombination Instability and Double S-Switching in *p*-Ge(Au)

Kh. O. Ibragimov, K. M. Aliev, I. K. Kamilov, and N. S. Abakarova

Institute of Physics, Dagestan Scientific Center, Russian Academy of Sciences, Makhachkala, Dagestan, Russia

e-mail: kamilov@datacom.ru

Received May 30, 2002

Abstract—We report on the experimental investigation of *p*-Ge(Au) samples and compare the results qualitatively to a one-dimensional theoretical model describing the recombination instability of current in gold-compensated germanium in a two-parameter (voltage–emission) space. Experiments showed the existence of three regimes of the system functioning in the parametric space. The second S-switching region was found on the current–voltage characteristic, which is probably related to a noise-induced nonequilibrium phase transition. *© 2003 MAIK "Nauka/Interperiodica".*

We have continued the experimental investigation [1, 2] of a real system corresponding to the one-dimensional theoretical model developed by Oshio and Yahata [3, 4] for germanium with deep levels of gold, according to which a recombination instability in the semiconductor leads to a current instability and gives rise to current oscillations. The model takes into account both the temporal and spatial evolution of a high-field domain formed in the system, describing this variation in a two-parametric space of the applied voltage U and the electron emission coefficient β. According to this model, the system can operate in various regimes, features the formation of subdomains and their reconstruction, and exhibits some other unusual properties not observed in typical nonlinear systems.

Depending on the particular region in the two-parametric space, the current–voltage characteristics (*I–U* curves) of the samples showed ohmic or superlinear initial regions and then either exhibited a smooth transition to saturation or acquired an N-like shape, which changed to an S-like shape with a further increase in the critical parameters. Previously [1, 2], the main experimental results were obtained using samples with an interelectrode distance of d = 3–8 mm and a cross section area of 1 mm^2 for the regions of *I–U* curves with saturation or N-like behavior.

In this short communication, we present new experimental results obtained for some specially selected regions of the parametric space under the conditions of injection from contacts and simultaneous illumination of the samples. The experiments were performed using "short" (not in the usual sense of $d \le L_D$, where L_D is the diffusion length, but in comparison with the samples studied in [1, 2]) *p*-Ge(Au) based p^+–p–n^+ structures with d = 1–3 mm, divided into two groups with the following characteristic parameters (77 K): $\rho_1 = 8.7 \times 10^4\ \Omega$ cm, $\mu_1 = 16500$ cm^2/(V s), $P_{01} = 4.33 \times 10^9$ cm^{-3} (group I); $\rho_2 = 1.95 \times 10^5\ \Omega$ cm, $\mu_2 = 29900$ cm^2/(V s), $P_{02} = 1.07 \times 10^9$ cm^{-3} (group II); here, ρ is the resistivity, μ is the carrier (hole) mobility, and P_0 is the equilibrium hole density.

The measurements were performed in the temperature range from 77 to 130 K using pulses with durations not exceeding 500 μs in order to avoid Joule heating of the samples. The sawtooth-shaped voltage pulses used to measure the forward and reverse (ascending and descending) branches of the *I–U* curves had a duration of 400 μs. The time series of the current oscillations measured in the samples were fed into a computer after conversion with an analog-to-digital converter operated at a sampling frequency of 200 MHz. These data were used to construct the phase portraits, bifurcation diagrams, and power spectra of the system studied. The emission coefficient β could be smoothly varied by exposure of the samples to a 100-W incandescent lamp and/or by nonequilibrium charge carrier injection via indium contacts (with 0.5% Ga, 0.5% Sn, and 7% Sb additives) deposited onto opposite edges of the samples with an area of 1 mm^2.

A distinctive feature of the *I–U* curves of the relatively "short" samples measured under the conditions of illumination without injection from contacts is the smooth transition from the ohmic to sublinear behavior (see Fig. 1, diagram *1*). The onset of sublinearity is manifested by the appearance of chaotic oscillations and a continuous noise band (Fig. 1, diagram *2*). With an increase in the applied voltage, the noise gives rise to spike-like oscillations (Fig. 1, diagram *3*) of the domain type, which sometimes exhibit a periodic character with period doubling (tripling, etc.). In most of the sublinear region of the *I–U* characteristic, the oscillations are chaotic and resemble the behavior typical of intermittency. The amplitude of the current pulse modulation by oscillations reaches up to 90%. The spectral

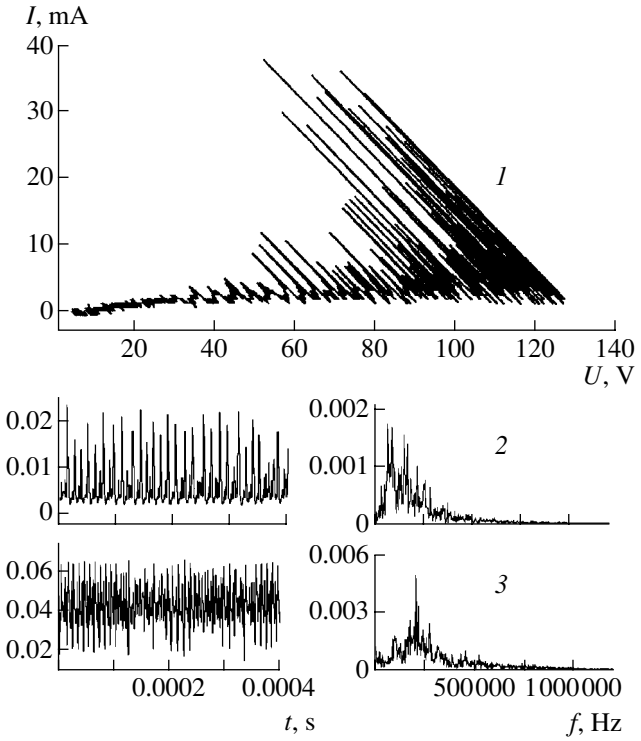

Fig. 1. Current–voltage characteristic (*1*), time series of current oscillations (*2* and *3*, left diagrams), and power spectra (*2*, and *3*, right diagrams) of a *p*-Ge(Au) sample measured at 77 K with an applied voltage of $U = 36.7$ (*2*) and 56 V (*3*).

characteristic displays a continuous noise band. As the applied voltage is increased further, the *I–U* curve acquires an S-like shape.

In the *I–U* curves of the samples simultaneously subjected to the illumination and the injection of carriers via contacts, increasing the applied voltage leads to a smooth transition from the linear to superlinear region, followed by the passage to a sublinear or N-like behavior. In the beginning of such sublinear (or N-like) region, there appear the current oscillations with a nearly coherent shape. As the applied voltage grows, this regime transforms via quasiperiodicity (Fig. 2, diagram *1*) to chaotic oscillations (Fig. 2, diagram *2*). Further increase in the voltage leads to the appearance of spike-like oscillations of the domain type (Fig. 2, diagram *3*). In some regions of the parametric space, these domains reveal oscillations with periods 2, 3, and 4, and subsequently, prior to the S-switching, the system passes to a chaotic state via intermittency. It should be noted that, using "short" structures, it is difficult to observe the whole variety of regimes related to a transformation of the spatial wave structure, including smooth subdomain formation. Nevertheless, all three theoretically predicted regimes of the system functioning (ohmic, quenched, transit-time) can be observed given thoroughly selected regions of the parametric space in the *I–U* curve regions corresponding to saturation or N-like behavior prior to the S-switching.

The most interesting results were obtained for samples of group I with $d = 1$–2 mm studied under the conditions of illumination with simultaneous carrier injection via contacts. Figure 3 shows evolution of the *I–U* curve of such a sample in the course of a gradual increase in the applied voltage at a constant illumination intensity. The curves clearly reveal the transition from an ohmic to superlinear regime and the appearance of current oscillations upon the onset of sublinearity (Fig. 3, diagram *1*). Prior to the S-switching, as pointed out above, there arises a large-amplitude noise, and the S-switching proceeds in the form of oscillations with a large amplitude and a nearly coherent shape. Two branches (forward and reverse) of the *I–U* curve form a limiting cycle. Further increase in the applied voltage leads to the appearance of cycles with periods 2 and 3. In this case, the noise component starts sharply growing again, and, as a result, the coherence is broken and the curve acquires an S-like shape (Fig. 3, diagram *2*). Positive branches of the region behind the S-switching are filled by a large-amplitude noise,

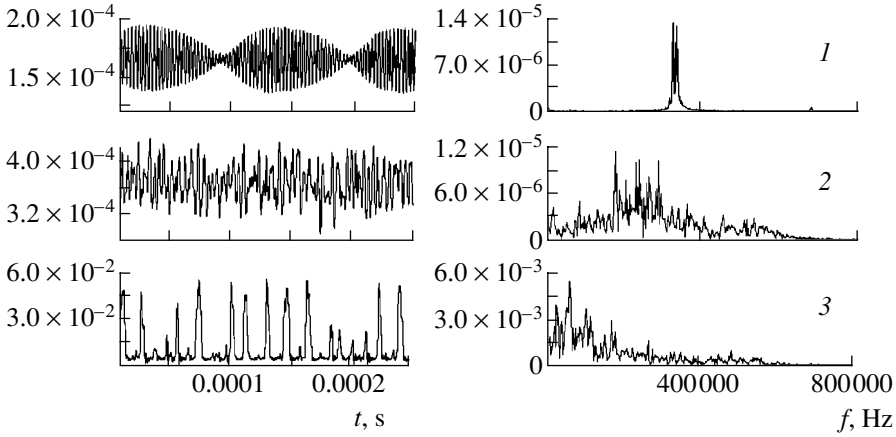

Fig. 2. The patterns of current oscillations (left column) and the corresponding power spectra (right column) measured in a *p*-Ge(Au) sample for various values of the applied voltage $U = 31.4$ (*1*), 102.4 (*2*), and 107.5 V (*3*).

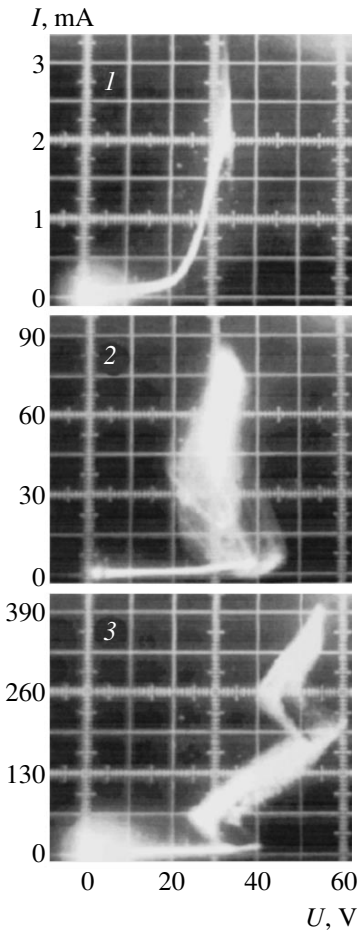

Fig. 3. Evolution of the current–voltage characteristic of a *p*-Ge(Au) sample with increasing applied voltage.

which is confirmed by the shape of the power spectrum. Increase in the applied voltage leads to the formation of the S-like region (Fig. 3, diagram *3*) with the noise amplitude gradually decaying on the positive branch. It should be noted that the ascending and descending branches of the *I–U* curve exhibit a significant hysteresis (~25%) in both S-switching regions.

The physical mechanisms explaining the above results can be reduced to the following. The *I–V* curve regions prior to the first S-switching (and the recombination instability of current in the two-parameter space characteristic of these regions) are quite consistent with the theoretical and experimental models [1–4]. The first S-switching is well explained in terms of the τ-mechanism according to Stafeev [5]. The nonequilibrium carrier injection simultaneously with intense illumination can lead to occupation of the gold levels ($E_{\mathrm{Au}}^{1} \approx$ 0.15 eV) in Ge and, hence, to a sharp increase in the lifetime of minority carriers (electrons).

The appearance of the second S-switching region in the *I–U* curve can be related to the second deep level of gold occurring below the conduction band bottom ($E_{\mathrm{Au}}^{2} \approx 0.2$ eV). However, this phenomenon is difficult to explain, because we failed to observe such a region in samples with interelectrode distances above 3 mm and below 1 mm. Probably, samples of a certain length possess some characteristic spatial and temporal scales and/or critical parameters that account for the noise-induced nonequilibrium phase transition appearing as the S-switching.

Some possible variants of the tricritical points in the space of parameters similar to that studied in our case were presented in [6]. It was also demonstrated [7] that, by means of injection, the concentration of minority carriers (electrons in *p*-Ge(Au)) can be increased relative to the equilibrium level to an extent such that the value $\alpha = (n/p)(\tau_n/\tau_p)$ will exceed unity (here n, p are the densities and τ_n, τ_p are the lifetimes of electrons and holes, respectively), which is a necessary condition for the excitation of recombination waves [8]. It should also be noted that an increase in the low-frequency noise intensity prior to the S-switching, as revealed by the power spectra, is analogous to the growth of long-wave fluctuations accompanying phase transitions.

Acknowledgments. This study was supported by the Russian Foundation for Basic Research, project no. 02-02-17817.

REFERENCES

1. I. K. Kamilov, N. S. Abakarova, Kh. O. Ibragimov, and K. M. Aliev, Pis'ma Zh. Tekh. Fiz. **27** (6), 24 (2001) [Tech. Phys. Lett. **27**, 183 (2001)].
2. N. S. Abakarova, Kh. O. Ibragimov, K. M. Aliev, and I. K. Kamilov, Semicond. Sci. Technol. **16**, 909 (2001).
3. K. Oshio and H. Yahata, J. Phys. Soc. Jpn. **65**, 1490 (1996).
4. K. Oshio and H. Yahata, J. Phys. Soc. Jpn. **67**, 2538 (1998).
5. V. I. Stafeev, Fiz. Tverd. Tela (Leningrad) **5**, 3095 (1963) [Sov. Phys. Solid State **5**, 2267 (1964)].
6. E. School, *Nonequilibrium Phase Transitions in Semiconductors* (Springer, Berlin, 1987).
7. I. V. Karpova and S. M. Syrovegin, Fiz. Tekh. Poluprovodn. (Leningrad) **16**, 1601 (1982) [Sov. Phys. Semicond. **16**, 1023 (1982)].
8. O. V. Konstantinov, V. K. Perel', and G. V. Tsarenkov, Fiz. Tverd. Tela (Leningrad) **9**, 1761 (1967) [Sov. Phys. Solid State **9**, 1381 (1967)].

Translated by P. Pozdeev

Technical Physics Letters, Vol. 29, No. 2, 2003, pp. 125–127. Translated from Pis'ma v Zhurnal Tekhnicheskoĭ Fiziki, Vol. 29, No. 3, 2003, pp. 89–94.

The Diffraction Focusing of X-rays upon Backscattering from a Bent Crystal Covered with Epitaxial Film: Sensitivity with Respect to the Interplanar Spacing Mismatch between Film and Substrate

T. Tchen

Moscow State Academy of Fine Chemical Technology, Moscow, Russia
e-mail: docent65@mtu-net.ru; ttchen@e-mail.ru

Received July 18, 2002

Abstract—The diffraction focusing of an X-ray wave reflected from a thick bent crystal covered with an epitaxial film is theoretically studied in the case when the Bragg angle θ_B is close to $\pi/2$. It is shown that the X-ray wave focusing upon backscattering from this system is sensitive with respect to the relative interplanar spacing mismatch $\Delta d/d$ between the epitaxial film and the thick crystal substrate. It is suggested that this effect can be employed for evaluating $\Delta d/d$ with an accuracy on the order of 10^{-10}. *© 2003 MAIK "Nauka/Interperiodica".*

As is known, the dynamic backscattering of X rays from crystals ($\theta_B \cong \pi/2$) offers the following advantages: (i) high reflected beam intensity, which is proportional to $-|\chi_{hr}|^{1/2}$ (χ_{hr} being the real part of the Fourier component of the X-ray polarizability) [1–4]; (ii) the absence of geometric aberrations [5]; (iii) small widths of the spectral interval $\Delta\lambda \sim \lambda(\Delta\theta)^2$ and the energy interval $\Delta E = E(\Delta\theta)^2$ of the backscattered radiation (λ, E, and $\Delta\theta$ being the X-ray wavelength, energy, and beam divergence angle, respectively) [6, 7]; and (iv) high sensitivity of the backscattered signal with respect to variations of the interplanar distance Δd [8, 9]. Using bent crystals can provide for an additional increase in the reflected beam intensity as compared to the case of $\theta_B \neq \pi/2$.

For realization of the backscattering regime, it is necessary to provide for "detuning" from the exact Bragg angle ($\theta_B = \pi/2$) and use a monochromatic (synchrotron) X-ray source. In this case, the source and its image (focus) will be separated by a sufficiently large distance.

This letter addresses the theory of the diffraction focusing of an X-ray wave reflected from a weakly bent thick crystal covered with a homoepitaxial film. The analysis proceeds from several assumptions. First, we consider a thick flat crystal substrate covered with a homoepitaxial film and then uniaxially bent to acquire the shape of an elliptic cylinder. Note that, in the case of usual diffraction, where $\theta_B \neq \pi/2$ and the angular width of the reflection curve is proportional to $|\chi_{hr}|$, a good approximation for the elliptic cylinder is provided by a parabolic cylinder. Second, we assume that bending the crystal does not cause any exfoliation of the epitaxial film. Third, the interplanar spacing mismatch between the epitaxial film and the thick crystal substrate is assumed to be constant throughout the film thickness. As is known, weak elastic bending of a crystal leads to a linear variation in the lattice period, but we will neglect this change. Fourth, the incident wave is assumed to be monochromatic, with the degree of monochromaticity $\Delta\lambda/\lambda \ll \Delta d/d$.

If the incident beam divergence angle satisfies the condition

$$\Delta\theta \geq (\Delta\theta)_{TRR} \cong 2|\chi_{hr}|^{1/2} > |\Delta d/d|^{1/2}, \quad (1)$$

where $(\Delta\theta)_{TRR}$ is the angular width of the total reflection region, we will observe two images of the source in the focal plane, S_s and S_f (Fig. 1), corresponding to reflection from the substrate and film, respectively.

In what follows, the degree of bending of a perfect crystal with a homoepitaxial film is considered as "weak" from the dynamic diffraction standpoint. This means that the amplitude reflection coefficient can be approximated by using the corresponding expression for a flat (unbent) crystal [10–12]:

$$R(\Delta\vartheta) = (R_1 - R_2 q)/(1 - q), \quad (2)$$

where

$$R_{1,2} = (-\breve{y} \pm \{\breve{y}^2 - 1\}^{1/2})(\chi_h/\chi_{-h})^{1/2}, \quad (3)$$

$$\breve{y} = [2\{(\Delta\vartheta)|\Delta\vartheta| - (\Delta d/d)\} + \chi_0]/(\chi_h\chi_{-h})^{1/2}, \quad (4)$$

χ_0, χ_h, and χ_{-h} are the Fourier components of the X-ray polarizability; $\Delta\vartheta = \vartheta - \pi/2$ is the angular deviation

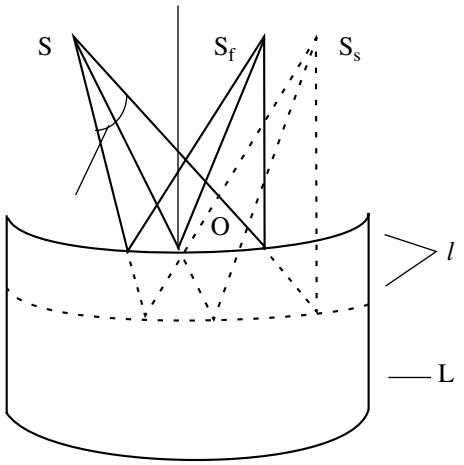

Fig. 1. The geometry of X-ray beam focusing upon backscattering from a weakly bent crystal covered with an epitaxial film: (S) X-ray source (SO = $L_0 = R_x$); (S_f) source image upon reflection from the film; (S_s) source image upon reflection from the substrate; (l) epitaxial film thickness; (L) thick bent crystal.

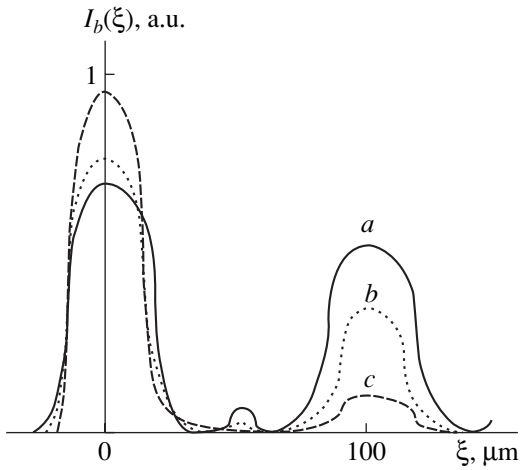

Fig. 2. Spatial distribution of the diffracted intensity in the plane of the source image for the backscattering from a bent crystal covered with films of various thicknesses $l = 3\Lambda$ (a), 2Λ (b), and 0.5Λ (c) ($\Lambda = \lambda/|\chi_{hr}| = 17$ μm is the extinction length). The calculations were performed for a (220) reflection of CuK_α radiation backscattered from a Si crystal; L_h = 10 m, $\Delta d/d = 10^{-10}$. The transverse coordinate ξ is measured relative to the direction of a wave backscattered from the substrate.

from the exact Bragg angle for an arbitrary plane-wave harmonic,

$$q = (R_1 - R_0) \times \exp[i2\pi(\chi_h\chi_{-h})^{1/2}(y^2 - 1)^{1/2} l/\lambda]/(R_2 - R_0), \quad (5)$$

$$R_0 = (-y + \{y^2 - 1\}^{1/2})(\chi_h/\chi_{-h})^{1/2}, \quad (6)$$

$$y = [2(\Delta\vartheta)|\Delta\vartheta| + \chi_0]/(\chi_h\chi_{-h})^{1/2}, \quad (7)$$

and l is the film thickness. Note that formulas (4) and (7) take into account that, in the case of backscattering, $\cos\theta_B \le |\Delta\vartheta| \le |\chi_{hr}|^{1/2}$.

According to the theory developed by Gabrielyan *et al.* [13], the diffracted wave amplitude $E_h(\xi_p)$ in the plane of the diffraction image is expressed as an integral of the plane-wave harmonics:

$$E_h(\xi_p) \sim \int_{-(\Delta\vartheta)_x}^{+(\Delta\vartheta)_x} d(\Delta\vartheta) R(\Delta\vartheta) \times \exp[-i\kappa(\Delta\vartheta)^2(1/\alpha_0 + 1/\alpha_h)/2 - i\kappa\Delta\vartheta\xi_p(1 - L_h/R_x)^{-1}], \quad (8)$$

where $\kappa = 2\pi/\lambda$, $\alpha_0 = L_0^{-1} - R_x^{-1}$, $\alpha_h = L_h^{-1} - R_x^{-1}$, R_x is the radius of bending of the crystal with the film, L_0 is the distance from the source to the center of the crystal, L_h is the distance from the center of the crystal to the source image, ξ_p is the transverse coordinate of the observation point, $(\Delta\vartheta)_x = l_x/(2L_0)$, and l_x is the crystal size in the plane of diffraction (backscattering).

Let us assume that the plane-wave reflection coefficient determined by formula (2) varies much slower than the exponents under the integral of relation (8). Then, the geometric condition of the focusing (lens formula) can be written as $\alpha_0 = -\alpha_h$, which implies that $L_0^{-1} + L_h^{-1} = 2R_x^{-1}$. Numerical integration of the expression for the intensity $I_h(\xi_p) = |E_h(\xi_p)|^2$ has been performed for $L_0 = 10$ m, $l_x = 10^{-2}$ m, $|\Delta d/d| = 10^{-10}$, and $R_x = 10$ m. As can be seen from the results presented in Fig. 2, backscattering from a crystal covered with a film of thickness $l \ge 2\Lambda$ ($\Lambda = \lambda/|\chi_{hr}|$ is the extinction length) leads to the appearance of two diffraction maxima, which correspond to reflection from the substrate and film. The distance between these maxima is well described by the formula $\Delta\xi = L_h|\Delta d/d|^{1/2}$.

The above results indicate that, theoretically, it is possible to use the diffraction focusing of X-rays upon backscattering from a bent crystal covered with an epitaxial film for estimating the interplanar spacing mismatch between film and substrate to within $\Delta d/d \sim 10^{-10}$.

Unfortunately, this method is inapplicable in the case of epitaxial films with thicknesses $l \le 0.5\Lambda$. Violation of the initial condition (1), resulting in a single maximum being observed for the intensity of radiation backscattered from the films and substrate, also makes the above results inapplicable.

REFERENCES

1. K. Kohra and T. Matsushita, Z. Naturforsch. A **27**, 484 (1972).

2. O. Brümmer, H. R. Höche, and J. Nieber, Phys. Status Solidi A **53**, 565 (1979).
3. A. Caticha and S. Caticha-Ellis, Phys. Rev. B **25**, 971 (1982).
4. V. I. Kuschnir and E. V. Suvorov, Pis'ma Zh. Éksp. Teor. Fiz. **44**, 205 (1986) [JETP Lett. **44**, 262 (1986)].
5. T. Tchen, V. A. Bushuev, and R. N. Kuz'min, Zh. Tekh. Fiz. **60** (10), 60 (1990) [Sov. Phys. Tech. Phys. **35**, 1148 (1990)].
6. W. Graeff and G. Materlik, Nucl. Instrum. Methods Phys. Res. **195**, 97 (1982).
7. Yu. V. Shvyd'ko and E. Gerdau, Hyperfine Interact. **123**–**124**, 741 (1999).
8. C. Cusatis, D. Udron, I. Mazzaro, *et al.*, Acta Cryst. A **52**, 614 (1996).
9. Yu. V. Shvyd'ko, E. Gerdau, J. Jäschke, *et al.*, Phys. Rev. B **57**, 4968 (1998).
10. M. V. Koval'chuk, V. G. Kon, and É. F. Lobanovich, Fiz. Tverd. Tela (Leningrad) **27**, 3379 (1985) [Sov. Phys. Solid State **27**, 2034 (1985)].
11. V. A. Bushuev and T. Chen, Vestnik Mosk. Univ., Ser. 3: Fiz. Astron. **29**, 58 (1988).
12. V. G. Kohn, Phys. Status Solidi B **231**, 132 (2002).
13. K. T. Gabrielyan, F. N. Chukhovskiĭ, and D. I. Piskunov, Zh. Éksp. Teor. Fiz. **96**, 834 (1989) [Sov. Phys. JETP **69**, 474 (1989)].

Translated by P. Pozdeev

Technical Physics Letters, Vol. 29, No. 2, 2003, pp. 128–129. Translated from Pis'ma v Zhurnal Tekhnicheskoĭ Fiziki, Vol. 29, No. 4, 2003, pp. 1–4.

Violet Luminescence in α-ZnSe Heterolayers

V. P. Makhniĭ, M. M. Sletov, and E. V. Stets

Chernovtsy State University, Chernovtsy, Ukraine

e-mail: oe-dpt.@chnu.cv.ua

Received July 19, 2002

Abstract—Zinc selenide layers of hexagonal modification, characterized by dominating violet emission in the room temperature luminescence spectrum, have been obtained on single crystal cadmium sulfide substrates by method of isovalent substitution. © *2003 MAIK "Nauka/Interperiodica".*

The creation of light-emitting devices operating in the short-wavelength region of the visible spectral range is among urgent problems that can be solved only by using wide-bandgap semiconductors. Materials extensively studied from this standpoint include bulk crystals and thin films of cubic zinc selenide (β-ZnSe) characterized by a bandgap width of E_g = 2.7 eV at 300 K, which corresponds to emission in the blue spectral region. Room temperature emission in this region was reported for various samples synthesized by different methods, including a promising isovalent substitution technique [1]. This method not only allows the class of appropriate semiconductor materials to be expanded but also provides for an increase in some physical and technological properties of these materials.

Below, we report on the effective room temperature luminescence in the violet region observed in hexagonal zinc selenide (α-ZnSe) heterolayers grown by isovalent substitution and present the main characteristics of this emission.

The samples were prepared on single crystal plates of undoped cadmium sulfide (α-CdS) possessing a wurtzite structure. This material was characterized by a weak electron conductivity at room temperature ($\sigma_n \approx 10^{-10}$ Ω^{-1} cm^{-1}) and exhibited intense green photoluminescence (PL). The α-ZnSe layers were obtained by sequentially annealing the initial substrates in saturated Zn and Se vapors. The process was conducted in quartz ampules evacuated to a pressure of 10^{-4} Torr, with the evaporated material and sample placed at opposite ends of the ampule.

The first annealing in Zn vapor leads to the formation of a white surface layer possessing a higher electron conductivity as compared to that of the initial substrate material. The λ-modulated optical reflection spectrum R'_ω of this layer exhibited a sharp peak with a maximum at $\hbar\omega_m \approx 3.75$ eV (which coincides with the E_g value of α-ZnS at room temperature [2]). Subsequent annealing of these samples in Se vapor results in a change of the sample surface color and a shift of the $\hbar\omega_m$ value to 2.89 eV (which is close to the E_g value of a hexagonal zinc selenide [3]). The thickness of the modified surface layer formed under the given annealing conditions (temperature, 1100 K; duration, 1 h) was 10–15 μm.

Additional evidence for the formation of an α-ZnSe heterolayer is provided by the following experimental facts: (i) the annealing of β-ZnSe in Se vapor under the same conditions leads to the formation of a surface layer with E_g = 2.7 eV (corresponding to the bandgap width of cubic zinc selenide [4]); (ii) the X-ray diffraction patterns of the samples upon annealing confirmed the cubic and hexagonal structure of ZnSe layers synthesized on β-ZnS and α-CdS substrates, respectively; (iii) N_2-laser irradiation of the samples leads to intense room temperature luminescence with the peaks at ~2.68 and 2.86 eV for β- and α-ZnSe, respectively. The above experimental evidence is sufficient to ascertain that a hexagonal zinc selenide layer rather than a $ZnSe_xS_{1-x}$ solid solution is formed on the sample surface as a result of the annealing.

Let us consider the PL spectrum (N_ω) in more detail. The room temperature emission is characterized by a broad asymmetric band with a maximum at about 2.86 eV (see figure). An inflection observed at the photon energy of 2.89 eV is most probably due to the interband recombination of free electrons and holes. The contour of this band can be readily calculated using the well-known formula [4]

$$N_\omega \approx (\hbar\omega)^2(\hbar\omega - E_g)^{1/2}\exp\left(-\frac{\hbar\omega - E_g}{kT}\right). \qquad (1)$$

However, as can be seen from the figure, the results of such calculations (dashed curve) do no agree with the experimental PL spectrum at $\hbar\omega \geq 2.9$ eV. The difference between the experimental and theoretical curves corresponds to an additional component (depicted by the dash–dot line). This emission can be explained by electron transitions from the conduction band to a valence subband (E_{vb}) split by the crystal field. However, final judgment concerning the nature of this band

1063-7850/03/2902-0128$24.00 © 2003 MAIK "Nauka/Interperiodica"

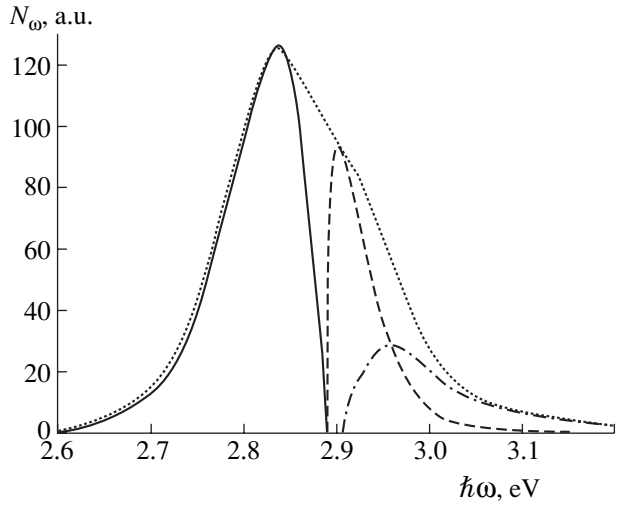

Experimental (points) and calculated (curves) room temperature PL spectra of the α-ZnSe layers studied (see the text for explanations).

requires additional detailed investigations under conditions of higher excitation levels and low temperatures.

The dominating PL band (solid curve) is characterized by the following features: (i) the band intensity I depends on the excitation intensity L according to a power law with an exponent of about ~1.5; (ii) as the excitation level L grows, the band maximum shifts toward higher energies; (iii) the high-energy band front is sharp and the low-energy front is relatively smooth, irrespective of the excitation level; and (iv) low excitation intensities L give rise to equidistant inflections on the low-energy wing at $\hbar\omega_0 \approx 21$ meV, which may correspond to an LO phonon energy in α-ZnSe. Note that the LO phonon energy of a cubic zinc selenide is well known (28 meV) [2]. This behavior is characteristic of the emission related to the annihilation of excitons upon inelastic scattering on free charge carriers [5].

Thus, the above results are indicative of the possibility of obtaining α-ZnSe layers exhibiting intense violet room temperature emission possessing an exciton character. The presence of an isovalent impurity, the role of which is played by residual sulfur atoms, can be expected to favor a high temperature stability of the emission observed. Note that this feature is typical of isovalent impurities and has been reported for many semiconductor crystals and films [6–8].

REFERENCES

1. V. P. Makhniy, V. E. Baranyuk, M. V. Demitch, *et al.*, Proc. SPIE **4425**, 272 (2000).
2. *The Physics of II–VI Semiconductor Compounds*, Ed. by A. N. Georgobiani and M. K. Sheĭkman (Nauka, Moscow, 1986).
3. R. Ludeke, J. Vac. Sci. Technol. **8**, 199 (1971).
4. V. P. Gribkovskiĭ, *Theory of Light Absorption and Emission in Semiconductors* (Nauka i Tekhnika, Minsk, 1975).
5. Koh Era and D. V. Langer, J. Lumin. **1–2**, 514 (1970).
6. V. K. Bazhenov and V. I. Fistul', Fiz. Tekh. Poluprovodn. (Leningrad) **18**, 1345 (1984) [Sov. Phys. Semicond. **18**, 843 (1984)].
7. E. V. Makhniĭ and M. M. Sletov, Pis'ma Zh. Tekh. Fiz. **26** (17), 71 (2000) [Tech. Phys. Lett. **26**, 787 (2000)].
8. V. P. Makhniĭ, M. M. Sletov, and Yu. Ya. Chaban, Zh. Tekh. Fiz. **72** (6), 135 (2002) [Tech. Phys. **47**, 786 (2002)].

Translated by P. Pozdeev

Technical Physics Letters, Vol. 29, No. 2, 2003, pp. 130–133. Translated from Pis'ma v Zhurnal Tekhnicheskoĭ Fiziki, Vol. 29, No. 4, 2003, pp. 5–13.

Microwave Losses in Electrodes of Distributed and Lumped Ferroelectric-Based Elements

O. G. Vendik, M. A. Nikol'skiĭ, and M. S. Gashinova

St. Petersburg State Electrotechnical University, St. Petersburg, 197376 Russia

e-mail: OGVendik@mail.eltech.ru

Received September 6, 2002

Abstract—The microwave losses in electrodes of a ferroelectric-based transmission line and a lumped ferroelectric-based element have been theoretically analyzed. The results of calculations of the effective loss tangent for the transmission line are confirmed by a two-dimensional electrodynamic model analysis and by experiments with a coplanar phase shifter. It is established that the use of microwave devices based on ferroelectric lumped elements is expedient in the 1–50 GHz frequency range (that is, in most microwave applications). The microwave losses in electrodes are significantly lower for lumped elements than for a long transmission line. These losses are determined by the ratio of the depth of electromagnetic field penetration into a conductor (superconductor) to the interelectrode gap width and are independent of the dielectric permittivity. © *2003 MAIK "Nauka/Interperiodica".*

Use of ferroelectric materials in planar electronic technology allows controlled microwave devices such as delay lines, phase shifters, and tunable filters to be obtained. Based on ferroelectrics of the BSTO type in combination with normal metals (Cu, Ag, Pt), such devices can operate at room temperature. Devices based on ferroelectrics of the STO type in combination with YBCO superconductors operate at liquid nitrogen temperature [1–5]. An important characteristic of any microwave device is the level of losses.

Microwave absorption in a transmission line based on a ferroelectric film. In a microwave device based on a transmission line with a thin dielectric (ferroelectric) layer, the total losses consist of contributions due to the dielectric film, characterized by the loss tangent $\tan\delta_d$, and the metal (or superconductor) electrodes with the corresponding effective loss tangent $\tan\delta_{eff}^{N(S)}$. Since ferroelectrics are used in microwave technology mostly as thin films, the electric field strengths necessary to control the permittivity in such devices are obtained using small interelectrode gap widths on the order of 5–20 μm. In the range of frequencies below 50 GHz, these distances are comparable to the depth of electromagnetic field penetration into a conductor (skin layer thickness) δ_{sk}. As will be demonstrated below, the losses in metal electrodes of a long transmission line with such gaps can significantly (by an order of magnitude) exceed the level of losses in dielectrics.

Recently, Krowne *et al.* [6] described a ferroelectric phase shifter based on a coplanar transmission line with a 5.5-μm-wide interelectrode gap (Fig. 1). The phase shifter exhibited anomalous losses, which were certainly determined by the losses in metal electrodes of the line. In this context, questions naturally arise as to whether this situation is general or represents a special case related to the particular device geometry and whether it is possible to avoid such anomalous losses.

Let us consider the cross section of an idealized model strip transmission line filled with a dielectric characterized by the permittivity ε_d and bounded with nonideal (lossy) "electric walls" at the interfaces with metal electrodes and with ideal "magnetic walls" at the interfaces with surrounding medium (Fig. 2a). Let us denote the dielectric layer thickness by d and the electrode width by w assuming that $d \ll w$.

The electromagnetic field components in the space bounded by the aforementioned "walls" are continuous. The field inside the structure is homogeneous and independent of the coordinates x and y. Under these conditions, the Helmholtz equation simplifies and a

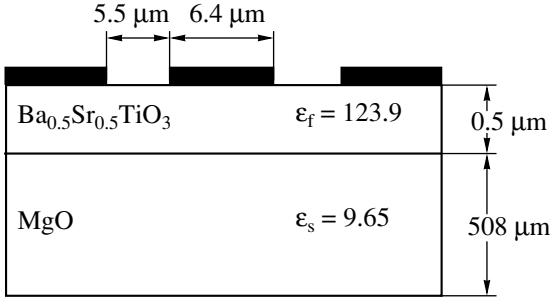

Fig. 1. Cross section of an experimental coplanar transmission line [6].

solution representing the wave propagating in the positive z direction can be written as

$$E(z) = E(0)e^{-i\gamma z},$$

where $E(0)$ is the electric field amplitude and γ is the complex propagation constant for a wave in a long lossy line. The latter quantity is defined as

$$\gamma = -\alpha - i\beta, \quad (1)$$

where α is the damping constant determining losses in the transmission line and β is the wavenumber in this line.

According to the theory of long lines, the lossy line can be represented by an equivalent scheme depicted in Fig. 2b. For this system, expression (1) can be written as

$$\gamma = \sqrt{(R_1 + i\omega L_1)(G_1 + i\omega C_1)}, \quad (2)$$

where the specific (per unit length) parameters of the idealized transmission line under consideration are as follows: inductance $L_1 = \mu_0 d/w$ (μ_0 is the permeability of vacuum); capacitance $C_1 = \varepsilon_0\varepsilon_d w/d$ (ε_0 is the permittivity of vacuum); resistance $R_1 = 2R_s/w$ (R_s is the surface resistance of conductors); and conductance $G_1 = \omega C_1 \tan\delta_d$ ($\tan\delta_d$ is the dielectric loss tangent).

Using formula (2) for the propagation constant and assuming that $\alpha \ll |k|$, we obtain the following expression for the damping constant:

$$\alpha = \frac{\pi}{\lambda}\left(\frac{R_1}{\omega L_1} + \tan\delta_d\right). \quad (3)$$

Here, the term $\tan\delta_d$ describes losses in the dielectric and the term

$$\frac{R_1}{\omega L_1} = \tan\delta_{eff}^{M} \quad (4)$$

characterizes losses in the metal (superconductor) electrodes of the transmission line.

Let us assume that the thickness of metal electrodes is greater than the depth of the electromagnetic field penetration into the conductor or superconductor (that is, than the skin layer depth δ_{sk} or the London penetration depth λ_L) at a given frequency. Substituting the expressions for the transmission line parameters from (2) into relation (4), we obtain the following formulas describing losses in the conductor (superconductor):

$$\tan\delta_{eff}^{N}(\omega, T) = \frac{\delta_{sk}(\omega, T)}{d} \quad (5a)$$

(loss tangent of a conductor),

$$\delta_{sk}(\omega, T) = \sqrt{\frac{2}{\omega\mu_0\sigma(T)}} \quad (5b)$$

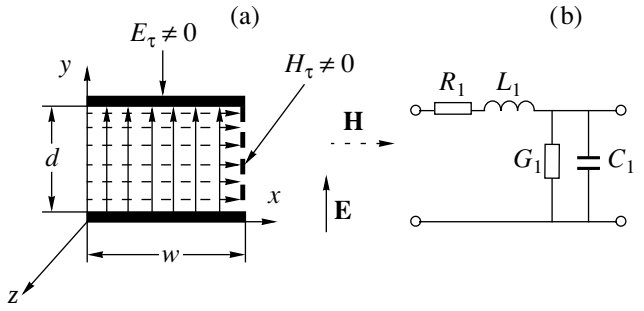

Fig. 2. Schematic diagrams of an idealized microstrip transmission line based on a ferroelectric film: (a) cross section; (b) equivalent scheme of a long line.

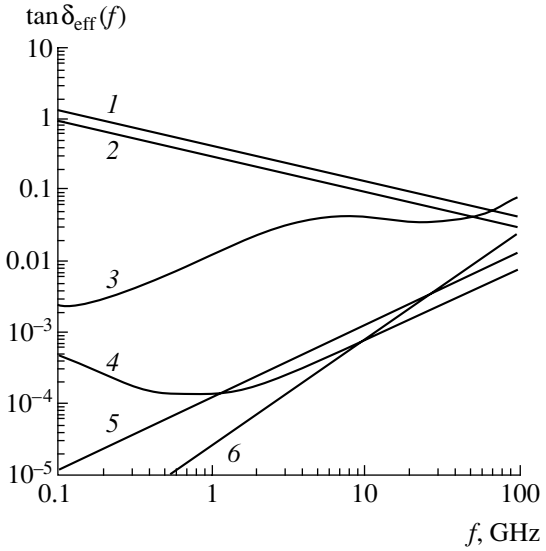

Fig. 3. Plots of the effective loss tangent versus frequency for (*1–5*) transmission lines and (*6*) a lumped element: (*1*) copper film at room temperature; (*2*) copper film at liquid nitrogen temperature; (*3*) $Ba_{0.5}Sr_{0.5}TiO_3$ film at room temperature [7, 8]; (*4*) $SrTiO_3$ single crystal at liquid nitrogen temperature [7, 8]; (*5*) high-T_c (YBCO) film at liquid nitrogen temperature; (*6*) copper film at room temperature.

(skin layer thickness or penetration depth),

$$\tan\delta_{eff}^{S}(\omega, T) = \frac{\omega\mu_0\sigma_N(T)\lambda_L^3(T)}{d} \quad (5c)$$

(loss tangent of a superconductor). Here, $\sigma(T)$ is the conductivity of a metal, $\sigma_N(T)$ is the conductivity of a superconductor in the normal state, ω is the frequency, and T is the absolute temperature.

According to formulas (4) and (5), the losses in electrodes are determined by the ratio of the electromagnetic field penetration depth in the conductor (superconductor) (characterized by the skin layer thickness δ_{sk} or the London penetration depth λ_L) to the interelectrode gap width.

Figure 3 shows the frequency dependences of the effective loss tangent for various materials calculated

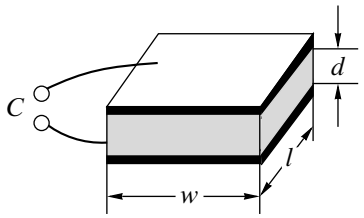

Fig. 4. Geometry of the sandwich capacitor with ferroelectric layer.

using formulas (4) and (5) for $d = 5.5$ μm. As can be seen from these data, the losses in metal electrodes dominate over the contributions of all other materials in the frequency range from 1 to 50 GHz. For comparison, Fig. 3 also shows the behavior of the loss tangent of a $SrTiO_3$ single crystal and a $Ba_{0.5}Sr_{0.5}TiO_3$ film calculated using a well-known phenomenological model [7, 8].

Microwave absorption in a lumped element based on a ferroelectric film. An alternative to distributed elements is offered by lumped ones. Consider such an element based on a strip line with a length of $l \ll \frac{\lambda}{8}$ (Fig. 4). The input impedance of the element (with neglect of losses in the ferroelectric) can be written as

$$Z_{IN} = -iZ_0\cot(kl), \tag{6}$$

where

$$Z_0 = \sqrt{(i\omega L_1 + R_1)/i\omega C_1}$$

and

$$k = -i\sqrt{(R_1 + i\omega L_1)i\omega C_1}.$$

Since $kl \ll 1$ (for lumped elements), $\cot(kl)$ in this expression can be expanded into series in small parameter. Restricting the expansion to the first two terms, we obtain

$$Z_{IN} = -iZ_0\left(\frac{1}{kl} + \frac{1}{3}kl\right). \tag{7}$$

This expression can also be presented (for $kl \ll 1$) as

$$Z_{IN} = \frac{1}{i\omega C}\left[1 + i\frac{1}{3}\left(\frac{2\pi}{\lambda}l\right)^2\frac{R_1}{\omega L_1}\right], \tag{8}$$

where $R_1/\omega L_1 = \delta_{sk}/d$ (see (3) and (4)). As can be seen from Eq. (8), the input impedance of the element under consideration (Fig. 2) exhibits a capacitive character. Therefore, losses in the metal are determined by the expression

$$\tan\delta_{eff}^N = \frac{1}{3}\left(\frac{2\pi}{\lambda}l\right)^2\frac{\delta_{sk}}{d}. \tag{9}$$

The frequency dependence of the effective loss tangent for metal electrodes of a lumped element is presented in Fig. 3. As can be seen, the losses in the element with a length of $l = 20$ μm (which is approximately $\lambda/10$ at a frequency of 50 GHz) are significantly lower as compared to those of a long line in the entire 1–50 GHz frequency range.

In addition, formula (9) shows that the losses in electrodes of a lumped element, as well as those of a distributed one, (i) are determined by the ratio of the electromagnetic field penetration depth δ_{sk} to the interelectrode gap width and (ii) significantly decrease with decreasing length of the element.

Microwave losses in a coplanar transmission line based on a ferroelectric film. In order to check the above theoretical conclusion that the microwave losses in electrodes of a distributed element by the ratio of the electromagnetic field penetration depth δ_{sk} to the interelectrode gap width, we used experimental data for the phase shifter based on a coplanar transmission line reported in [6]. The phase shifter geometry is presented in Fig. 1. For elucidating the influence of the ferroelectric layer on the parameters of wave propagation in this

Experimental and calculated values of the effective loss tangent in metal electrodes of a phase shifter based on a coplanar line (Fig. 1) and a microstrip line (10 GHz, zero dc bias)

Experiment (coplanar line [6])			Idealized model (microstrip line)	Electrodynamic analysis (coplanar line)		
h_f, μm	ε_f	$\tan\delta_{eff}^N$	$\tan\delta_{eff}^N$	h_f, μm	ε_f	$\tan\delta_{eff}^N$
0.5	123.9	0.143	0.118	0.5	124	0.144
				0.5	620	0.14
				0.5	1240	0.14
				0.1	1860	0.139
				0.5		0.139
				1		0.139

coplanar line, we have performed a two-dimensional electrodynamic spectral analysis analogous to that presented recently in [9]. The effective loss tangent in electrodes is related to the propagation parameters by the formula

$$\tan\delta_{\text{eff}}^{\text{N}} = \frac{2\alpha}{\beta}, \quad (10)$$

which is valid under the conditions that damping in the transmission line is determined primarily by the losses in electrodes, while the losses in the ferroelectric film can be ignored (Fig. 3).

Table presents the results of calculations of the effective loss tangent in metal electrodes of a coplanar line, performed using expressions (4) with $d = 5.5$ μm, in comparison with the values obtained using formula (10) and with the experimental data (for 10 GHz at a zero dc bias) [6].

Discussion or results. Thus, according to expressions (4) and (5) obtained above for the distributed elements and formula (9) for a lumped element, the losses in electrodes are determined by the ratio of the electromagnetic field penetration depth in the conductor (characterized by the skin layer thickness δ_{sk} or the London penetration depth λ_L) to the interelectrode gap width while being independent of the properties of the filling medium (in our case, of the dielectric permittivity and thickness of the ferroelectric film). In addition, the above analysis of the microwave losses in both distributed and lumped elements based on ferroelectric films leads to a conclusion that, in the 1–50 GHz frequency range (i.e., in most microwave applications), it is expedient to employ microwave devices with lumped elements where the losses in electrodes are significantly losses as compared to those in the systems with distributed elements (Fig. 3).

Conclusion. Our calculations of the effective loss tangent by formula (4) agree with the two-dimensional electrodynamic model analysis [9] and with the experimental data [6] for a phase shifter based on a coplanar transmission line. These results are compared in the table. As can be seen from this comparison, relation (4) derived for an idealized transmission line (Fig. 2), in which the field geometry is significantly different from that of the coplanar line, gives the effective loss tangent close to the values obtained from the electrodynamic calculation and from the experiment. Note that even a significant change in parameters of the coplanar line is not accompanied by noticeable variations of the loss tangent. Simple relations (4), (5), and (9), provide for a rapid and sufficiently accurate estimation of the effective loss tangent in metal or superconductor electrodes of any planar microwave device.

REFERENCES

1. R. Romanofsky, J. Bernhard, G. Washington, *et al.*, IEEE MTT-S Int. Microwave Symp. Dig. **3**, 1351 (2000).
2. V. Sherman, K. Astafiev, N. Setter, *et al.*, IEEE Microwave Wireless Comp. Lett. **11** (10), 407 (2001).
3. I. Vendik, O. Vendik, V. Sherman, *et al.*, IEEE MTT-S Int. Microwave Symp. Dig. **3**, 1371 (2000).
4. O. G. Vendik, I. B. Vendik, V. V. Pleskachev, *et al.*, Integr. Ferroelectrics **43** (1–4), 153 (2002).
5. O. G. Vendik, I. B. Vendik, and V. Sherman, Integr. Ferroelectrics **43** (1–4), 145 (2002).
6. C. M. Krowne, M. Daniel, S. W. Kirchoefer, *et al.*, IEEE Trans. Microwave Theory Techn. **MTT-50**, 537 (2002).
7. O. G. Vendik and S. P. Zubko, J. Appl. Phys. **82**, 4475 (1997).
8. O. G. Vendik and S. P. Zubko, J. Appl. Phys. **88**, 5343 (2000).
9. O. G. Vendik, M. S. Gashinova, and A. N. Deleniv, Pis'ma Zh. Tekh. Fiz. **28** (11), 37 (2002) [Tech. Phys. Lett. **28**, 461 (2002)].

Translated by P. Pozdeev

Technical Physics Letters, Vol. 29, No. 2, 2003, pp. 134–137. Translated from Pis'ma v Zhurnal Tekhnicheskoĭ Fiziki, Vol. 29, No. 4, 2003, pp. 14–21.

The Effect of Photoexcitation of the Electrical Properties of ZnS:Mn Thin-Film Emitters

N. T. Gurin, A. V. Shlyapin, O. Yu. Sabitov, and D. V. Ryabov

Ul'yanovsk State University, Ul'yanovsk, Russia

e-mail: soy@sv.uven.ru

Received July 29, 2002

Abstract—Significant distinctions have been observed in the current kinetics and current–voltage characteristics of ZnS:Mn electroluminescent thin-film emitters measured with pulsed photoexcitation in different (blue, red, and infrared) spectral intervals. The results show evidence that a recharge of deep centers related to the zinc and sulfur vacancies takes place in the course of the emitter operation, leading to the formation of space charges in the near-anode and near-cathode regions of the phosphor layer. © *2003 MAIK "Nauka/Interperiodica".*

Introduction. Data reported on the photoelectric properties of ZnS:Mn electroluminescent thin-film (ELTF) emitters, as well as the fact of emission in the blue spectral region, are indicative of the important role of deep centers related to zinc vacancies (V_{Zn}) with energies 2.7–2.8 eV below the conduction band bottom of ZnS:Mn [1–4]. On the other hand, some characteristics of these ELTF emitters cannot be explained without assuming that deep centers related to the sulfur vacancies (V_S) participate in the electroluminescence (EL) process as well [4–8].

We aimed at studying the effect of photoexcitation in different spectral regions on the electrical properties of ZnS:Mn ELTF emitters in the active regime in order to elucidate the role of deep centers in the EL process development and to estimate the positions of the corresponding energy levels in the forbidden band of ZnS:Mn.

Experimental. The experiments were performed on ELTF emitters with a metal–insulator–semiconductor–insulator–metal (MISIM) layer structure. Here, M layers represent a lower transparent 0.2-μm-thick SnO_2-based electrode deposited onto a glass substrate and the upper nontransparent thin-film Al electrode with a thickness of 0.15 μm and a diameter of 1.5 mm; S is the 0.48-μm-thick electroluminescent ZnS:Mn (0.5 wt %) layer; and I are the 0.17-μm-thick insulating ZrO_2–Y_2O_3 (13 wt %) layers. The ZnS:Mn phosphor layer was obtained by thermal evaporation in a quasi-closed volume in vacuum and deposition onto a substrate heated to 250°C, followed by annealing for 1 h at 250°C. The upper nontransparent metal electrode was also formed by thermal deposition in vacuum, while thin insulating layers were prepared using the electron-beam deposition technique.

We have experimentally studied the time variation of the current I_e through an ELTF emitter excited with alternating-sign voltage pulses of a triangular shape $V(t)$. The excitation signal was supplied by a G6-34 generator equipped with an additional shaping amplifier and controlled by a G5-89 master generator. The maximum pulse amplitude was V_m = 160 V at a nonlinearity coefficient not exceeding 2%. The measurements were performed either in a continuous excitation regime at a frequency of f = 20 or 50 Hz or in a pulse train mode, whereby the excitation signal represented pairs of triangular pulses with a frequency of f = 4, 20, or 50 Hz. In the first half-period, either a positive or a negative excitation half-wave can be applied to the upper electrode, which will be referred to as the +Al and –Al regimes, respectively. The time interval T_s between excitation pulse trains was T_s = 0.2, 2, or 100 s.

The emitter current I_e was measured in a 100 Ω–10 kΩ resistor connected in series with the emitter structure (the voltage drop on this resistor did not exceed 0.5% of V_m). The patterns of excitation voltage $V(t)$ and ELTF emitter current $I_e(t)$ were recorded with the aid of a two-channel storage oscillograph of the S9-16 type linked via an interface to a personal computer. The data acquisition system ensured the measurement and storage of 2048 experimental points at a preset discretization period in each channel and 256 levels of the amplitude quantization. The data were mathematically processed and graphically displayed using the application program packages MAPLE V (Release 4, Version 4.00b) and GRAPHER (Version 1.06, 2-D Graphing System).

The time variation of the average field $F_p(t)$ in the phosphor layer, the current $I_p(t)$, and the charge $Q_p(t)$ passing through this layer during ELTF emitter operation were determined as described elsewhere [6, 7], using the values of capacitances of the insulating films (C_i = 730 pF) and the phosphor layer (C_p = 275 pF) determined using an immittance meter of the E7-14 type and the known ELTF emitter geometry. The ELTF

1063-7850/03/2902-0134$24.00 © 2003 MAIK "Nauka/Interperiodica"

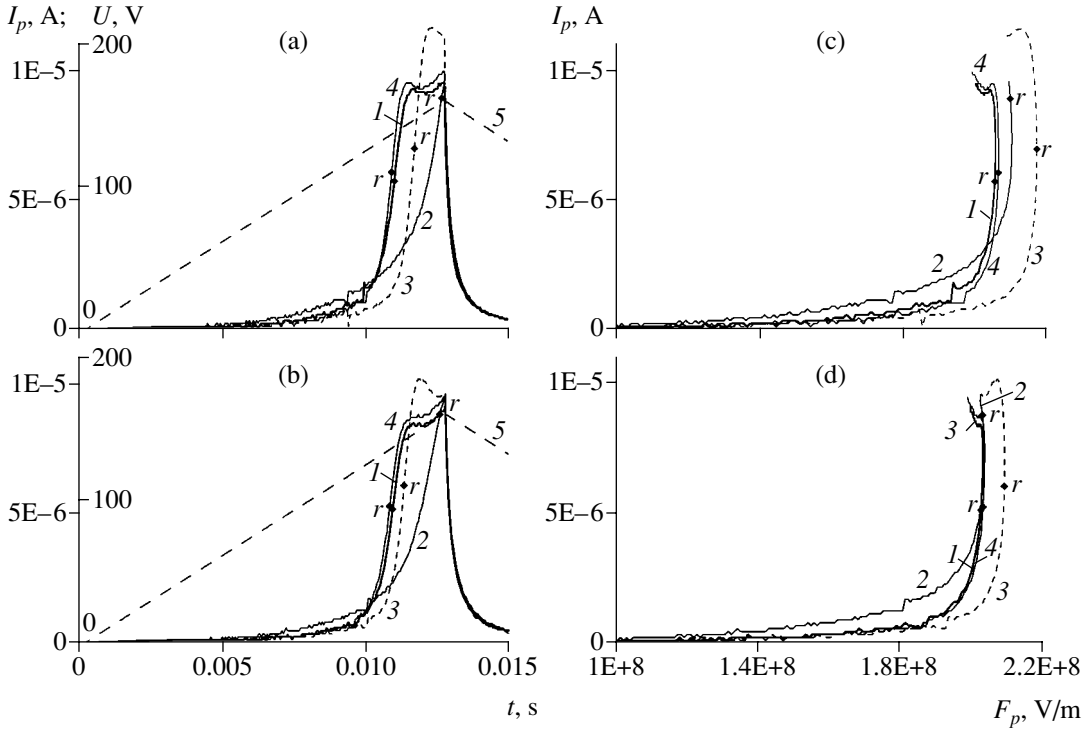

Fig. 1. The plots of (a, b) $I_p(t)$ kinetics and (c, d) $I_p(F_p)$ for ZnS:Mn ELTF emitters measured in the pulsed photoexcitation regime in the pause between voltage pulses (f = 20 Hz; T_s = 100 s) applied in the (a, c) –Al and (b, d) +Al modes: (*1*) no photoexcitation; (*2*) blue light; (*3*) red light; (*4*) IR radiation; (*5*) $V(t)$ profiles.

emitter structures were photoexcited from the substrate side using either continuous or pulsed light. In the blue spectral region, the photoexcitation source was an E1L51-3B light-emitting diode (LED) with an emission band maximum at λ_m = 475 nm, a halfwidth of $\Delta\lambda_{0.5} \approx 35$ nm, a luminous intensity of ~1 cd, a total power of $P \approx 5$ mW, and a photon flux density of $\Phi \approx 1.6 \times 10^{15}$ mm^{-2} s^{-1}. In the red spectral region, the photoexcitation source was a semiconductor laser with λ_m = 656 nm, $\Delta\lambda_{0.5}$ = 15 nm, $P \approx 1$ mW; and $\Phi \approx 4 \times 10^{14}$ mm^{-2} s^{-1}. In the IR range, the samples were photoexcited using a pair of LEDs of the AL107A type with λ_m = 950 nm, $\Delta\lambda_{0.5}$ = 25 nm, total power $P \approx 12$ mW; and total photon flux density $\Phi \approx 3 \times 10^{15}$ mm^{-2} s^{-1}.

Photoexcitation in the pulsed regime could be performed in two ways, whereby a sample was exposed to light (i) during the action of a pulse train of two periods of the triangular voltage or (ii) during the interval between pulse trains (starting immediately upon termination of the second pulse and lasting for the entire time interval between neighboring pulse trains).

Results. The main experimental results can be summarized as follows:

(1) There is asymmetry in the $I_e(t)$, $L(t)$, $I_p(t)$, and $I_p(F_p)$ curves measured in the +Al and –Al regimes (see Fig. 1). This is explained (following [6, 7]) by the nonuniform distribution of the structural defects and Mn^{2+} impurity ions in the phosphor layer (the concentration of Mn^{2+} ions increases on the passage from lower to upper electrode).

(2) In the pulsed optical photoexcitation regime, the behavior in the pause between applied voltage pulses differs from that in the variant without illumination:

(i) In the blue spectral region, there was observed a significant increase in the current magnitude in the initial part of the $I_p(t)$ profile before point r separating the regions of "fast" and "slow" growth of $I_p(t)$. On the passage through this point, the slope of the curve decreases [6, 7], the length of the "slow" growth region drops (see Figs. 1a and 1b), and the average field $F_p(t)$ in the phosphor layer for the –Al variant increases (see Figs. 1c and 1d).

(ii) In the red spectral region, the current in the initial "fast" region of the $I_p(t)$ buildup decreases, the $I_p(t)$ pulse amplitude increases in the "slow" region (see Figs. 1a and 1b), and the $F_p(t)$ amplitude grows in both regions (see Figs. 1c and 1d), this growth being more significant in the –Al variant.

(iii) In the IR spectral region, the $I_p(t)$ current magnitude in the initial "fast" growth region in the –Al variant exhibits a slight decrease, followed by an increase in the growth rate, a small increase in the current pulse amplitude $I_p(t)$ (see Figs. 1a and 1b), and a small increase in the $F_p(t)$ field for both +Al and –Al variants (see Figs. 1c and 1d).

(3) The above variations in the $I_p(t)$ profile observed with photoexcitation in the blue and red spectral regions significantly decrease in the second half-period of the excitation voltage, decrease still lower in the third half-period, and fall within the experimental error limits in the fourth half-period. For the IR illumination, the increments of the $I_e(t)$ (and, hence, $I_p(t)$) current amplitudes are retained during the excitation voltage half-periods from second to fourth.

(4) For the pulsed illumination during the voltage pulse action, changes in the $I_p(t)$ values are much less pronounced as compared to those in the absence of illumination and are observed only in the region of the $I_p(t)$ buildup, whereby the $I_p(t)$ amplitudes vary within the limits of experimental uncertainty.

(5) For ELTF emitters excited in the continuous regime in the entire range of frequencies studied, no influence of continuous illumination on the $I_p(t)$ kinetics was observed in the three spectral regions employed.

Discussion of results. The above results can be explained as follows. With the sample preparation technology employed, various structural defects are formed in the ZnS:Mn layer. From the thermodynamic standpoint, the most probable defects are zinc and sulfur vacancies [9]. The energy positions of deep centers related to these vacancies are as follows: for a singly charged zinc vacancy (V_{Zn}^-), 0.5–0.6 eV above the valence band top (E_V) [10, 11]; for a singly charged sulfur vacancy (V_S^+), 0.6–2.0 eV below the conduction band bottom (E_C) [10, 12]; for a doubly charged zinc vacancy (V_{Zn}^{2-}), 1–1.1 eV above E_V [1–4, 11]; for a doubly charged sulfur vacancy (V_S^{2+}), 1.05–1.3 eV above E_V [9, 13]; and for a neutral sulfur vacancy (V_S^0), 0.2–1.05 eV below E_C [10, 12].

Taking into account that the Fermi level in ZnS in the equilibrium state occurs slightly above the middle of the forbidden band, thus accounting for the small electron conductivity, it is more probable that the main defects in this state are the deep sulfur vacancies V_S^+ occurring at the center of the forbidden band (with the energy above that of the doubly charged V_S^{2+} centers) and the V_{Zn}^{2-} vacancies (occurring deeper than the singly charged V_{Zn}^- centers in the forbidden band).

In the active ELTF emitter operation regime, as the applied voltage exceeds the threshold level, electrons are injected by means of tunneling emission from the surface states on the near-cathode region of the insulator–phosphor interface. Ballistically accelerated in the interelectrode region, electrons produce impact ionization of Mn^{2+} centers and the deep centers related to V_{Zn}^{2-}, V_S^+, and V_{Zn}^+ in the near-anode region of the phosphor with the formation of a positive space charge. In the near-cathode region, free electrons trapped on the deep centers related to V_S^+ and V_S^{2+} neutralize the positive space charge formed in the preceding ELTF emitter operation cycle and give rise to a negative space charge. In the pause between the two sequential ELTF emitter operation cycles, both space charges are neutralized to a degree increasing with the pause duration.

Irradiation of an ELTF emitter during the pause with photons in the spectral intervals studied leads to the following conclusions.

(i) Photoexcitation in the blue spectral region hinders neutralization of the positive space charge in the (former) near-anode region, which increases the field strength in the near-cathode region, enhances the tunneling emission current from the surface states on the near-cathode region of the insulator–phosphor interface, and decreases the current component due to the impact ionization of deep V_{Zn}^{2-} and V_S^+ centers in the new ELTF emitter operation cycle (see Fig. 1a and 1b).

(ii) Photoexcitation in the red spectral region hinders neutralization of the negative space charge in the former near-cathode region and produces neutralization of the positive space charge in the former near-anode region with the formation of a negative space charge in this region (due to photoelectrons from the valence band trapped on a level corresponding to V_S^+). This decreases the field strength in the near-cathode region, suppresses the tunneling emission current, and increases the average fields strength required for ionization of the deep V_S^0 and V_{Zn}^{2-} centers in the near-anode region of the phosphor during the new ELTF emitter operation cycle (Figs 1c and 1d). After reaching these values, the current amplitude increases to a level above that in the absence of photoexcitation (see Figs. 1a and 1b).

(iii) Photoexcitation in the IR spectral region results in the production of additional V_S^+ centers as a result of the trapping electrons (liberated in the valence band) on the V_S^{2+} centers. This leads to a decrease in the field strength in the near-cathode region during the next operation cycle and in the tunneling emission current for the –Al variant (Fig. 1a), in which case the density of sulfur vacancies at the upper phosphor–insulator interface exceeds that of the zinc vacancies and determines the positive space charge. As the applied field strength increases, the current amplitude grows due to ionization of the V_S^+ centers additionally formed in the phosphor (see Fig. 1). The increment of the $I_p(t)$ current amplitude is retained during the $V(t)$ half-periods from second to fourth, probably because relaxation of V_S^{2+} centers (additionally neutralized by the IR radiation

and occurring in the V_S^+ state—the deepest in the forbidden band of ZnS) to the equilibrium state proceeds over a maximum time, which is longer than that for the other centers and significantly exceeds the time period between sequential ELTF emitter operation cycles during the application of two excitation voltage pulses.

The decrease in the magnitude of variations in the $I_p(t)$ current under the conditions of photoexcitation in the blue or red spectral regions during the second, third, and fourth half-periods of the excitation voltage is caused by sequential recharge of the V_{Zn}^{2-} and V_S^+ deep centers in the forbidden band of ZnS:Mn. This process is related to the impact ionization of these centers in the active operation state and the trapping of free carriers during the pause between sequential ELTF emitter operations, under the conditions of a constant equilibrium density of these centers upon return to a quasistationary state characteristic of an unirradiated ELTF emitter.

Finally, the significantly weaker changes in the $I_p(t)$ current observed in the pulsed photoexcitation regime during the application of voltage pulses is explained by the significantly shorter time of the radiation action upon the ELTF emitter (at f = 20 Hz, not exceeding 12.5 ms for the first half-period of the excitation voltage) as compared to the pause duration between these pulses (99.9 s). For the same reason, the photoexcitation of an ELTF emitter operating in the continuous regime does not lead to noticeable changes in the current kinetics.

REFERENCES

1. W. E. Howard, O. Sahni, and P. M. Alt, J. Appl. Phys. **53** (1), 639 (1982).
2. K.-W. Yang and S. J. T. Owen, IEEE Trans. Electron Devices **ED-30** (5), 452 (1983).
3. A. A. Douglas, J. F. Wager, D. C. Morton, *et al.*, J. Appl. Phys. **73** (1), 296 (1993).
4. K. A. Neyts, D. Corlatan, P. De Visschere, *et al.*, J. Appl. Phys. **75** (10), 5339 (1994).
5. E. Bringuier, Philos. Mag. **75** (2), 209 (1997).
6. N. T. Gurin, O. Yu. Sabitov, and A. V. Shlyapin, Zh. Tekh. Fiz. **71** (8), 48 (2001) [Tech. Phys. **46**, 977 (2001)].
7. N. T. Gurin, A. V. Shlyapin, and O. Yu. Sabitov, Zh. Tekh. Fiz. **72** (2), 74 (2002) [Tech. Phys. **47**, 215 (2002)].
8. N. T. Gurin, A. V. Shlyapin, and O. Yu. Sabitov, Pis'ma Zh. Tekh. Fiz. **28** (15), 24 (2002) [Tech. Phys. Lett. **28**, 631 (2002)].
9. *The Physics of II–VI Semiconductor Compounds*, Ed. by A. N. Georgobiani and M. K. Sheĭkman (Nauka, Moscow, 1986).
10. F. A. Kröger, *The Chemistry of Imperfect Crystals* (Wiley, New York, 1964; Mir, Moscow, 1969).
11. N. A. Vlasenko, M. M. Chumachkova, Z. L. Denisova, *et al.*, J. Cryst. Growth **216**, 249 (2000).
12. I. K. Morozova and V. A. Kuznetsova, *Zinc Sulfide: Synthesis and Properties* (Nauka, Moscow, 1987).

Translated by P. Pozdeev

Technical Physics Letters, Vol. 29, No. 2, 2003, pp. 138–140. Translated from Pis'ma v Zhurnal Tekhnicheskoĭ Fiziki, Vol. 29, No. 4, 2003, pp. 22–27.

Centrosymmetric Acoustic Emission from a Nonlinearly Oscillating Charged Drop

A. R. Gaibov, S. O. Shiryaeva, A. I. Grigor'ev, and D. F. Belonozhko

Yaroslavl State University, Yaroslavl, Russia

e-mail: shir@uniyar.ac.ru

Received April 5, 2002

Abstract—Oscillations of a charged drop of an incompressible liquid have been calculated to within the second order of smallness relative to the oscillation amplitude. It is predicted that a monopole component is present in the acoustic emission spectrum, which is related to the time dependence of the zero mode oscillation amplitude manifested in this approximation. *© 2003 MAIK "Nauka/Interperiodica".*

1. An incompressible liquid drop oscillating in a compressible medium can emit acoustic waves. The oscillation spectrum calculated in an approximation linear with respect to the oscillation amplitude contains no contributions due to the zero and first modes [1]. For a constant drop volume, the most intense component in the acoustic emission spectrum is that related to the fundamental mode [2]. Dipole emission, related to the excitation of translational modes, appears only in the calculations tasking into account terms of the second order of smallness in the oscillation amplitude, whereby the spectrum of modes determining the initial deformation of the drop contains two adjacent modes [3, 4].

Formulation of the problem concerning the acoustic emission from an oscillating liquid drop is related to the notion that the *n*th oscillation mode produces a distortion of the equilibrium spherical shape proportional to $\sim P(\mu)\exp(i\omega_n t)$, where $\mu \equiv \cos\theta$, $P_n(\mu)$ are the Legendre polynomials, and ω_n is the frequency of the *n*th mode. Periodic motions of the drop surface give rise to periodic pressure variations in the compressible surrounding medium, that is, generate an acoustic wave. In drops with dimensions typical of natural systems (fog, cloud, rain), the frequencies of oscillations fall within the frequency range of sound waves and longwave ultrasonic waves (see, e.g., [5–8] and references therein). The presence of an electric charge on a drop, deviation of the drop shape from spherical, motion of the drop relative to the medium, and allowance for the drop viscosity lead to a shift of the spectrum of capillary oscillations toward lower frequencies [4–6], that is, to the region of acoustic waves detected by the human ear.

In this context, we will consider the problem of describing the time variation of the oscillation mode amplitudes of a charged drop generating acoustic waves as a result of oscillations of the drop surface. The problem refers to the modes generated upon the initial excitation of one mode and is considered in the second order of smallness with respect to the oscillation amplitude, aiming at an analysis of the features of acoustic emission due to excited modes. To simplify the qualitative analysis, we will assume that the initial perturbation of the equilibrium spherical drop shape can be expressed as $\alpha P_2(\mu)$, where α is a small perturbation amplitude.

2. Consider a drop of an ideal incompressible electrically conducting liquid with the radius *R*, the density ρ_1, the surface tension γ, and the charge *Q* occurring in an external ideal compressible medium characterized by the density ρ_2 and the sound velocity *c*. The system will be described in a spherical coordinate system with the origin at the drop center, in which an equation describing the drop surface in dimensionless polar coordinates at an arbitrary time can be written as

$$r = R + \xi(\theta, t),$$

where ξ is a small perturbation of the drop surface ($|\xi|/R \le \alpha/R \ll 1$). The drop oscillations and the wave motions in the surrounding medium are assumed to possess a potential character and are described by the velocity field potentials ψ_1 and ψ_2, respectively.

The mathematical formulation of the initial-value problem of determining the amplitudes of excited modes is as follows [2–4]:

$$\Delta\Phi = 0; \quad \Delta\psi_1 = 0; \quad \frac{1}{c^2}\frac{\partial^2\psi_2}{\partial t} - \Delta\psi_2 = 0;$$

$$r = R + \xi; \quad \frac{\partial\psi_1}{\partial n} = \frac{\partial\psi_2}{\partial n};$$

$$\frac{\partial\psi_1}{\partial r} = \frac{\partial\xi}{\partial t} + \frac{1}{r^2}\frac{\partial\xi}{\partial\theta}\frac{\partial\psi_1}{\partial\theta};$$

1063-7850/03/2902-0138$24.00 © 2003 MAIK "Nauka/Interperiodica"

$$\Delta p - \rho_1 \frac{\partial \psi_1}{\partial t} - \rho_1 \frac{1}{2}(\nabla \psi_1)^2 + \rho_2 \frac{\partial \psi_2}{\partial t} - \frac{\rho_2}{2c^2}\left(\frac{\partial \psi_2}{\partial t}\right)$$

$$+ \frac{1}{2}\rho_2 (\nabla \psi_2)^2 + \frac{\varepsilon}{8\pi}(\nabla \Phi)^2 = \gamma \mathrm{div}\mathbf{n};$$

$$\Phi = \mathrm{const};$$

$$r \longrightarrow \infty: \frac{\partial \psi_2}{\partial t} + ik\psi_2 = o\left(\frac{1}{r}\right); \qquad (1)$$

$$t = 0: r = R + \xi_0 + \alpha P_2(\mu); \quad \psi_1 = 0;$$

$$-\frac{1}{4\pi}\oint_S (\mathbf{n} \cdot \nabla \Phi) ds = Q,$$

$$S = [r = R + \xi(\theta, t),\ 0 \le \theta \le \pi,\ 0 \le \phi \le 2\pi];$$

$$\int_V \mathbf{e}_r \cdot r^3 dr \sin\theta d\theta d\phi = 0;$$

$$V = [0 \le r \le R + \xi(\theta, t),\ 0 \le \theta \le \pi,\ 0 \le \phi \le 2\pi];$$

$$\int_V r^2 dr \sin\theta d\theta d\phi = \frac{4}{3}\pi R^3.$$

Here, Φ is the electric field potential, **n** is the unit vector of normal to the drop surface; Δp is the difference of hydrostatic pressures inside and outside the drop, γ is the surface tension coefficient, and ξ_0 is a normalization constant determined from the conditions of constancy of the drop volume.

As demonstrated previously [9], initial excitation of the fundamental mode ($n = 2$) gives rise, in addition to this mode, to the zero ($n = 0$) and forth ($n = 4$) modes due to the mode interaction in the second order of smallness. Since we are interested only in the features of an acoustic emission from the drop, the analysis will be concentrated on the possible zero mode oscillations, which can give rise to a monopole acoustic emission not reported previously. Emission of the modes with $n \ge 1$ was studied, for example, in [2, 3].

Solution of the above problem by standard methods (see, e.g., [4, 9, 10]) in the approximation quadratic in α yields the following expression for the time variation of the zero mode amplitude of the surface oscillations:

$$a_0(t) = -\frac{1}{10R}\{2\kappa^2 \exp(-2\omega^* t)$$

$$\times \cos^2(\omega t + \beta) + [2\alpha^2 - 2\kappa^2 \cos^2(\beta)]\},$$

$$\kappa = \sqrt{\alpha^2 + \alpha^2\left(\frac{\omega^*}{\omega}\right)^2}; \quad \beta = \arctan\left(-\frac{\omega^*}{\omega}\right);$$

$$\omega = \mathrm{Re}(\sqrt{\tau + i\tau^*}); \quad \omega^* = \mathrm{Im}(\sqrt{\tau + i\tau^*});$$

$$\tau = \frac{4\gamma(1-W)}{R^3}[2\rho_1(81 + 9k^2R^2 - 2k^4R^4 + k^6R^6)$$

$$+ 4\rho_2(27 + 6k^2R^2 + k^4R^4)] \qquad (2)$$

$$\times [(81 + 9k^2R^2 - 2k^4R^4 + k^6R^6)\rho_1^2$$

$$+ 4(27 + 6k^2R^2 + k^4R^4)\rho_1\rho_2 + 4(9 + 3k^2R^2 + k^4R^4)\rho_2^2]^{-1};$$

$$\tau^* = \frac{4\gamma(1-W)}{R^3}[4\rho_2 k^5 R^5]$$

$$\times [(81 + 9k^2R^2 - 2k^4R^4 + k^6R^6)\rho_1^2$$

$$+ 4(27 + 6k^2R^2 + k^4R^4)\rho_1\rho_2 + 4(9 + 3k^2R^2 + k^4R^4)\rho_2^2]^{-1};$$

$$W \equiv Q^2/16\pi R^3\gamma; \quad k \equiv \omega/c.$$

3. At first glance, the circumstance that the zero mode amplitude is a periodic function of time contradicts the initial assumption concerning incompressibility of the liquid drop and the fact (well known from linear theory and related to the condition of constancy of the drop volume [1, 11]) that the drop must perform no radial oscillations. Indeed, the equation describing the shape of a drop surface perturbed by a capillary wave motion can be represented (in the dimensionless form adopted above) as an expansion in terms of the normalized Legendre polynomials [11]

$$r(\theta, t) = a_0 + \sum_{n=2}^{\infty} a_n(t) P_n(\mu); \quad \mu \equiv \cos(\theta). \qquad (3)$$

Here, $a_n(t)$ are the time-dependent mode amplitudes of the capillary oscillations and a_0 is the zero mode amplitude determined from the condition of constancy of the drop volume in Eqs. (1). Substituting expression (3) into Eq. (1), using an approximation linear with respect to the mode amplitude a_n (i.e., with respect to $|\xi|$) and taking into account the mutual orthogonality of the Legendre polynomials, we obtain a formula showing that a_0 is independent of time and equal to the equilibrium radius of the drop ($a_0 = R$). However, the same calculation retaining terms of the second order of smallness yields an expression for a_0 depending on the time:

$$a_0 \approx R - \frac{1}{2R}\sum_{n=2}^{\infty} (a_n(t))^2.$$

For an ideal liquid, the coefficients $a_n(t)$ are periodic functions of time. Thus, the time dependence of the zero mode amplitude, appearing in the second order of smallness with respect to the initial perturbation amplitude, follows from the condition of conservation of the drop volume.

A periodic time variation of the zero mode amplitude gives rise to centrosymmetric waves of compression and rarefaction in the surrounding compressible

medium, that is, to the acoustic waves. In other words, a nonlinearly oscillating drop can be considered as a monopole emitter of the acoustic waves.

4. As can be also seen from Eqs. (1), a periodic part of the amplitude accounting for the acoustic emission decays with time as described by the decrement ω^*. This damping determines losses of the energy of oscillations for the acoustic emission.

For the numerical estimates, we will consider (as in [2, 3]) raindrops with $\rho_1 = 1$ g/cm^3, $\rho_2 = 1.3 \times 10^{-3}$ g/cm^3, $\gamma = 73$ dyn/cm, $a = 0.1R$, $kR \ll 1$, $R = 250$ μm, and a number density of $N = 0.3$ cm^{-3}. The drop charge is assumed to be much smaller that a limiting value in terms of stability according to Rayleigh ($W \ll 1$) [8, 11].

The expression for the power J of an acoustic emission from a spherical droplet oscillating with a amplitude a_0 is as follows [12]:

$$J = \frac{2\pi\rho_2 R^4 \omega^4 a_0^2}{c(1 + \omega^2 R^2/c^2)}. \quad (4)$$

According to Eqs. (2)–(4), $\alpha_0 \approx 10^{-3}R$, and the power of monopole acoustic emission at a frequency of $\omega \approx 6 \times 10^3$ s^{-1} from a single drop with the above characteristics is on the order of 10^{-7} erg/s. The acoustic power emitted from a rain space with a volume of 1 km^3 is ≈3 W, which significantly exceeds both the power of dipole acoustic emission related to the excitation of translational modes [3] and the power of quadrupole acoustic emission generated by the fundamental mode in the linear approximation [2]. On the boundary of such a cloud, the integral monopole acoustic emission is characterized by a loudness of ≈60 dB, which is comparable with that of human speech.

According to Eqs. (2), the role of the intrinsic drop charge mostly influences the frequency of the acoustic emission. Thus, by changing the drop charge, it is possible to control the acoustic emission frequency, for example, to convert ultrasonic oscillations into usual sound and vice versa.

5. In conclusion, monopole acoustic emission in the range of sound frequencies related to excitation of the zero mode oscillations in an oscillating liquid drop (manifested as a nonlinear effect in the second order of smallness relative to the oscillation amplitude) plays a determining role in the integral intensity of acoustic emission from liquid drop systems, for example, from the space occupied by a rain.

Acknowledgments. This study was supported by Presidential Grant no. 00-15-9925.

REFERENCES

1. L. D. Landau and E. M. Lifshitz, *Fluid Mechanics* (Nauka, Moscow, 1986; Pergamon Press, Oxford, 1987).
2. A. I. Grigor'ev and A. R. Gaibov, Zh. Tekh. Fiz. **71** (11), 6 (2001) [Tech. Phys. **46**, 1351 (2001)].
3. A. I. Grigor'ev, S. O. Shiryaeva, A. R. Gaibov, and D. F. Belonozhko, Pis'ma Zh. Tekh. Fiz. **21** (22), 7 (2001) [Tech. Phys. Lett. **21**, 934 (2001)].
4. S. O. Shiryaeva, Zh. Tekh. Fiz. **72** (4), 15 (2002) [Tech. Phys. **47**, 389 (2002)].
5. Won-Kyu Rhim, Sang Kun Chung, M. T. Hyson, *et al.*, IEEE Trans. Ind. Appl. **IA-23** (6), 975 (1987).
6. V. Sh. Shagapov, Izv. Akad. Nauk SSSR, Fiz. Atmos. Okeana **24** (5), 506 (1988).
7. E. H. Trinh, R. G. Holt, and D. B. Thiessen, Phys. Fluids **8** (1), 43 (1996).
8. A. I. Grigor'ev and S. O. Shiryaeva, Izv. Ross. Akad. Nauk, Mekh. Zhidk. Gaza, No. 3, 3 (1994).
9. S. O. Shiryaeva, Zh. Tekh. Fiz. **71** (2), 27 (2001) [Tech. Phys. **46**, 158 (2001)].
10. D. F. Belonozhko and A. I. Grigor'ev, Zh. Tekh. Fiz. **70** (8), 45 (2000) [Tech. Phys. **45**, 1001 (2000)].
11. C. D. Hendricks and J. M. Schneider, Am. Phys. **1** (6), 450 (1963).
12. L. F. Lependin, *Acoustics* (Vysshaya Shkola, Moscow, 1978).

Translated by P. Pozdeev

Technical Physics Letters, Vol. 29, No. 2, 2003, pp. 141–143. Translated from Pis'ma v Zhurnal Tekhnicheskoĭ Fiziki, Vol. 29, No. 4, 2003, pp. 28–32.

Minimization of Phase Distortions of Transmitted Radiation upon Optical Switching in Vanadium Dioxide Film

O. P. Mikheeva and A. I. Sidorov

Institute of Laser Physics, St. Petersburg, Russia

Received August 15, 2002

Abstract—We have numerically modeled transmission of radiation with a wavelength of $\lambda = 10.6$ or 3.4 μm through a VO_2 film and a change in phase of the transmitted radiation upon a transition of the film material from semiconductor to metallic state. It is established that there are optimum values of the film thickness for which the phase changes tend to zero. Conditions favoring minimization of the phase distortions are determined for a single VO_2 film and a multilayer interferometer with such a film. © *2003 MAIK "Nauka/Interperiodica".*

Polycrystalline films of vanadium dioxide (VO_2) are used in optical switching devices and laser radiation attenuators operating in the middle infrared range [1, 2]. In these devices, the transmitted (or reflected) radiation intensity is controlled using the effect whereby the dielectric permittivity of VO_2 strongly varies upon the reversible semiconductor–metal phase transition [3, 4]. An increase in the coefficients of refraction and reflection of a VO_2 film as a result of the phase transition is manifested not only in a decrease of the transmission coefficient but in a phase shift of the transmitted radiation as well. When the optical switches and attenuators are employed in transceivers, it is frequently required to provide for a minimum phase distortion related to the amplitude processing.

We have studied the influence of a semiconductor–metal phase transition in a VO_2 film on the phase shift of transmitted radiation with $\lambda = 10.6$ and 3.4 μm and analyzed the possibility of minimizing this shift while retaining the optimum amplitude characteristics of the optical switching element.

The system was modeled using optical constants of a polycrystalline VO_2 film for $\lambda = 10.6$ and 3.4 μm [1, 5]. Numerical calculations according to the Fresnel formulas were performed by a recurrent method for a single VO_2 film on a germanium substrate and for a multilayer interferometer involving such a film on the same substrate. A change in the phase of the transmitted radiation as a result of the phase transition in VO_2 was determined by the formula $\Delta\varphi(t) = \delta\varphi(t_0) - \delta\varphi(t)$, where $\delta\varphi(t_0)$ and $\delta\varphi(t)$ are the phase shifts before the phase transition and at a temperature $t > t_0$, respectively.

Figure 1a shows the temperature dependence of $\Delta\varphi$ for radiation with $\lambda = 10.6$ μm in VO_2 films of various thicknesses d calculated for the temperature interval of the semiconductor–metal phase transition ($t_0 < t < t_1$, where t_1 is a temperature in the interval of the phase transition). Here and below, for the sake of better illustration, the initial points of all curves are fit to the same level and $\delta\varphi(t_0)$ is taken equal to zero. For films with small thicknesses ($d < 0.15$ μm), the shapes of the $\Delta\varphi(t)$ curves are determined by the temperature dependence of the real part of the complex permittivity. As the film thickness grows, the role of the imaginary part tends to increase.

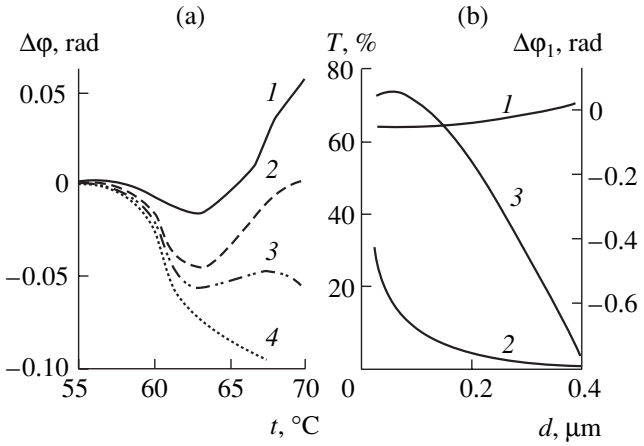

Fig. 1. (a) Temperature dependences of the phase change of radiation ($\lambda = 10.6$ μm) transmitted through VO_2 films with thicknesses $d = 0.05$ (*1*), 0.13 (*2*), 0.16 (*3*), and 0.2 μm (*4*); (b) plots of the radiation transmission coefficient T (*1*) before and (*2*) after the VO_2 phase transition and (*3*) phase change $\Delta\varphi_1$ upon the phase transition versus VO_2 film thickness d.

1063-7850/03/2902-0141$24.00 © 2003 MAIK "Nauka/Interperiodica"

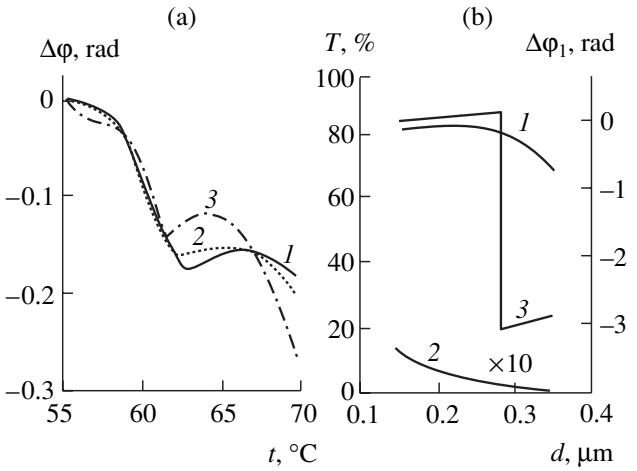

Fig. 2. (a) Temperature dependences of the phase change of the radiation with $\lambda = 10.6$ μm transmitted through four-layer interferometers involving VO_2 films with thicknesses $d = 0.18$ (*1*), 0.2 (*2*), and 0.27 μm (*3*); (b) plots of the radiation transmission coefficient T (*1*) before and (*2*) after the VO_2 phase transition and (*3*) phase change $\Delta\varphi_1$ upon the phase transition versus VO_2 film thickness d in the interferometer.

The characteristics of an optical switch can be optimized, for example, under the following conditions: a change in the transmitted radiation phase must not exceed $\pi/5 - \Delta\varphi_1 < 0.63$ rad, while the degree of modulation of the optical transmission coefficient upon the phase transition (defined as the coefficient $K = T(t_0)T(t_1)$) must exceed 50. Figure 1b shows the plots of the transmission coefficient of a VO_2 film before and after the phase transition and the phase change of the transmitted radiation versus VO_2 film thickness. As the film thickness is increased, the transmission coefficient of the film at temperatures below the phase transition increases, which is related to a clarification effect of a semiconducting VO_2 film with the optical thickness approaching $\lambda/4$. In contrast, the transmission coefficient of the same film upon the phase transition decreases as a result of increase in the absorption. For $d \approx 0.13$ μm, the change in the phase of the transmitted radiation as a result of the phase transition exhibits a minimum (Fig. 1a), while $\Delta\varphi$ upon the phase transition tends to zero (Fig. 1b). However, the coefficient of transmission of a film with this thickness changes upon the phase transition only by a factor of about ten, which is insufficient for most applications. At the same time, as can be seen from Fig. 1, the above conditions are satisfied in the interval of film thicknesses $0.3\ \mu\text{m} < d < 0.37\ \mu\text{m}$. Indeed, for $d = 0.37$ μm, the phase changes upon the phase transition only by $\Delta\varphi_1 = 0.6$ rad, while the transmission coefficient changes by a factor of $K = 70$.

An analogous optimization analysis performed for $\lambda = 3.4$ μm showed that optimum optical characteristics for this wavelength can be attained with film thicknesses in the intervals $0.2\ \mu\text{m} < d < 0.27\ \mu\text{m}$ and $0.29\ \mu\text{m} < d < 0.4\ \mu\text{m}$. In particular, for $d = 0.26$ and 0.3 μm, a change in the radiation phase upon the transition amounts to $\Delta\varphi_1 = 0.08$ and 0.05 rad, while $K = 460$ and 1100, respectively. Note that a VO_2 film thickness of 0.28 μm corresponds to an optical thickness of $\lambda/4$, and the resulting interference accounts for a jumplike increase in the phase shift up to 3.1 rad.

We have also calculated the phase shift as a function of the angle of incidence of the radiation. The results of these calculations showed that variation of the beam incidence angle within 5° for $\lambda = 10.6$ and 3.4 μm leads to phase distortions not exceeding 0.6 rad.

Using optical switches based on multilayer interferometers with VO_2 films as control elements, it is possible to obtain a much greater modulation coefficient as compared to that of a single VO_2 film (see, e.g., [1, 6]). Figure 2a shows the phase change of the transmitted radiation with $\lambda = 10.6$ μm as a function of the temperature for a four-layer interferometer of the following structure: ZnSe(0.5)–BaF_2(2.2)–VO_2(*d*)–ZnS(1.0)–Ge(substrate) (here and below, figures in parentheses indicate layer thicknesses in microns). As can be seen from these data, the $\Delta\varphi$ value does not change sign upon the VO_2 phase transition and increases with the VO_2 film thickness. For $d = 0.27$ μm, the change in the transmitted radiation phase upon transition is about 0.28 rad (i.e., does not exceed $\pi/10$). The transmission coefficient of the interferometer with such a film changes upon the phase transition (Fig. 2b) by a factor of 230 (from 80 to 0.35%). The maximum transmission of the interferometer before the phase transition is observed for a VO_2 film thickness of 0.25 μm. Further increase in the thickness d leads to a growth of the modulation coefficient (at the expense of a decrease in the transmission upon the phase transition), but this implies a decrease in the transmission coefficient before the phase transition and an increase in the phase shift. A jump in the phase shift observed for $d > 0.28$ is explained by the fact that the corresponding optical thickness exceeds $\lambda/4$.

For a radiation wavelength of 3.4 μm, the modeling was performed for an interferometer of the following structure: Ge(0.14)–ZnS(0.25)–VO_2(*d*)–ZnSe(0.17)–Ge(substrate). The results of these calculations showed that, for the VO_2 film thickness within $0.15\ \mu\text{m} < d < 0.24\ \mu\text{m}$ and $0.27\ \mu\text{m} < d < 0.29\ \mu\text{m}$, the transmission coefficient before the phase transition exceeds 50%, while the $\Delta\varphi_1$ value in the same interval of film thicknesses does not exceed 0.3 rad. Upon the phase transition, the transmission coefficient drops down to several tenths or hundredths of a percent, while the modulation coefficient reaches 1500.

Thus, optimization of the VO_2 film thickness in the optical switch provides for a minimum change in the phase of the transmitted infrared radiation, which does not exceed $\pi/5$ rad (in some cases, $\pi/10$ rad). At the same time, the transmission modulation coefficient upon the phase transition remains at a sufficiently high level (from 70 to 1500).

Acknowledgments. This study was supported by the International Scientific-Technological Center, grant no. 1454.

REFERENCES

1. F. C. Case, Appl. Opt. **30**, 4119 (1991).
2. O. P. Mikheeva and A. I. Sidorov, Opt. Zh. **68** (4), 48 (2001).
3. A. A. Bugaev, B. P. Zakharchenya, and F. A. Chudnovski, *Metal–Semiconductor Phase Transition and Its Applications* (Nauka, Leningrad, 1979).
4. W. Bruckner, H. Opperman, W. Retchel, *et al.*, *Vanadiumoxide* (Akademie-Verlag, Berlin, 1982).
5. O. P. Konovalova, A. I. Sidorov, and I. I. Shaganov, Opt. Zh. **65** (4), 20 (1998).
6. O. P. Konovalova, A. I. Sidorov, and I. I. Shaganov, Opt. Zh. **66** (5), 13 (1999).

Translated by P. Pozdeev

Technical Physics Letters, Vol. 29, No. 2, 2003, pp. 144–146. Translated from Pis'ma v Zhurnal Tekhnicheskoĭ Fiziki, Vol. 29, No. 4, 2003, pp. 33–38.

Magnetic Birefringence in a Suspension Containing Carbon Nanotubes

S. G. Polushin, V. A. Nikitin, A. N. Ponomarev, and E. I. Rjumtsev

Institute of Physics, St. Petersburg State University, St. Petersburg, Russia

e-mail: polushin@paloma.spbu.ru

Revised manuscript received October 3, 2002

Abstract—We have studied the magnetic birefringence in aqueous suspensions prepared from cathode deposits containing up to 5% of multi-walled carbon nanotubes and in suspensions of some other carbon materials. The magnetooptical effect observed in the suspensions of materials with nanotubes can be considered as a superposition of two contributions, one being related to the presence of graphite and graphitelike structures in suspension and the other, to the multi-walled nanotubes. The magnetic birefringence technique can be used to determine the content of multi-walled nanotubes and to obtain carbon materials enriched with nanotubes. © *2003 MAIK "Nauka/Interperiodica"*.

This study is devoted to carbon materials obtained by the method of plasma arc discharge between graphite electrodes in a helium atmosphere. Under these conditions, carbon nanostructures nucleate and grow on the cathode, in the region where the arc temperature reaches up to 4000 K. The material deposited on the cathode is characterized by a complicated structural and fractional composition, including graphitized structures of irregular shape, amorphous carbon, and polyhedral multi-walled carbon nanostructures. The main products of this synthesis are materials with a high content of multi-walled nanotubes appearing as separate rodlike inclusions imaged in the micrograph of Fig. 1.

The compositions of such carbon materials can be determined by a number of methods, each particular technique having disadvantages. This study aimed at checking for the efficacy of the method of dilute solutions, which has been previously successfully used for investigations of macromolecules [1], in application to the analysis of novel carbon materials.

The experimental setup included an electromagnet generating fields with a strength of up to 2 T, a 5-mW He–Ne laser, and a 10-mm-long cell with a volume of 1 cm^3. The light beam propagated perpendicularly to the magnetic field. The cell with a sample was placed between crossed polarizer and analyzer. The angle between the magnetic field direction and the polarization plane of the light was 45°. This is a typical experimental geometry used for studying the field induced birefringence. The magnetic birefringence Δn was measured by a compensation technique [2] using a modulator of the elliptical polarization of light.

The sample suspensions were prepared by sonication of a mechanically ground material in water with a surfactant additive (sodium dodecylsulfate). Upon mixing, the suspensions were allowed to stand for a time period of not less than 24 h prior to measurements. During this time, coarse particles (accounting for more than 95% of the total carbon material) were precipitated. The remaining suspension contained predominantly quasimolecular particles with a concentration on the order of 0.001 g/cm^3, which kept decreasing with time as a result of continuing sedimentation. The suspensions were transparent and exhibited a light gray tint.

Preliminarily, we have measured magnetic birefringence in the suspensions of carbon materials known to be free of nanotubes (amorphous carbon, graphite) and those synthesized in the electric arc under conditions leading to the formation of graphitelike structures without nanotubes (as confirmed by electron-microscopic investigations). It was established that the value of birefringence Δn in the suspensions of graphite and graphitelike structures was negative, increased in magnitude even in weak fields, and rapidly reached saturation (Fig. 2, curves *1–3*). This behavior can be related to the relatively large dimensions of these structures. As expected, neither aqueous solutions of pure sodium dodecylsulfate nor amorphous carbon suspensions with additives of the same surfactant exhibited a magnetooptical effect.

A qualitatively different character of the magnetic birefringence was observed in the suspensions prepared from cathode deposits containing multi-walled nanotubes. The presence of such nanotubes was confirmed by independent techniques, including electron microscopy (Fig. 1). For these suspensions, the value of birefringence in weak magnetic fields was also negative, while in strong fields the magnitude of Δn exhibits a quadratic dependence on the magnetic field strength (the Cotton–Mouton law) and tends to be positive. Since it was established that graphite nanostructures

1063-7850/03/2902-0144$24.00

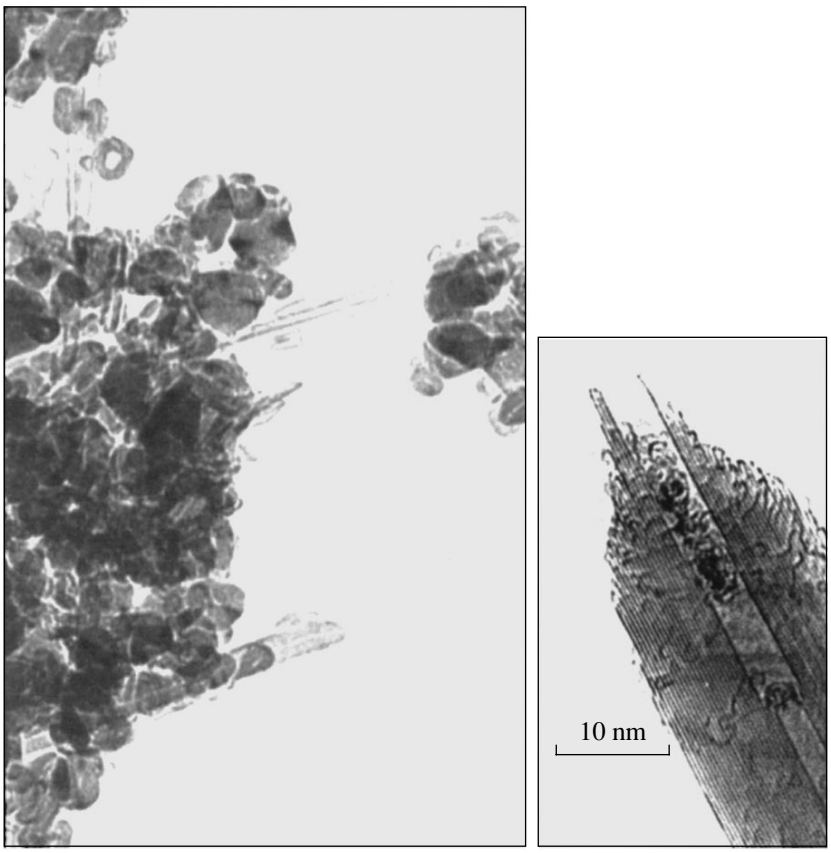

Fig. 1. Electron micrographs of a carbon material containing multi-walled nanotubes. The right-hand part shows an enlarged image of a nanotube with open inner channel.

exhibit negative magnetic birefringence, it was also suggested that these very structures are responsible for the initial portion of the Δn versus B^2 curve (Fig. 2). The quadratic branch can be related to another component of the mixture.

According to the Cotton–Mouton law, the magnetic birefringence of a molecular solution is described by the expression $K = \Delta n/CH^2$, where K is the Cotton–Mouton constant, C is the solution concentration, and H is the magnetic field strength. For molecules with an axial symmetry of the magnetic and optical properties, the Cotton–Mouton constant is related to the molecular parameters by the formula

$$K = 2\pi N_A(n^2 + 2)^2\Delta\gamma\Delta\chi/135kTnM,$$

where n is the refractive index of the solution, M is the molecular weight of the solvent, and $\Delta\gamma$ and $\Delta\chi$ are the optical and magnetic anisotropies of the molecule, respectively. Similar to giant molecules with a significant shape anisotropy, the nanotubes must possess a large positive optical and diamagnetic anisotropy. The product $\Delta\gamma\Delta\chi$ has to be positive and proportional to the shape anisotropy (i.e., to the ratio of length to diameter). Analogous behavior was experimentally observed for rigid rodlike macromolecules with aromatic cycles in the backbone [3].

In the suspensions of cathode deposits studied in our experiments, the fraction of multi-walled carbon nanotube in the suspended material did not exceed 5%,

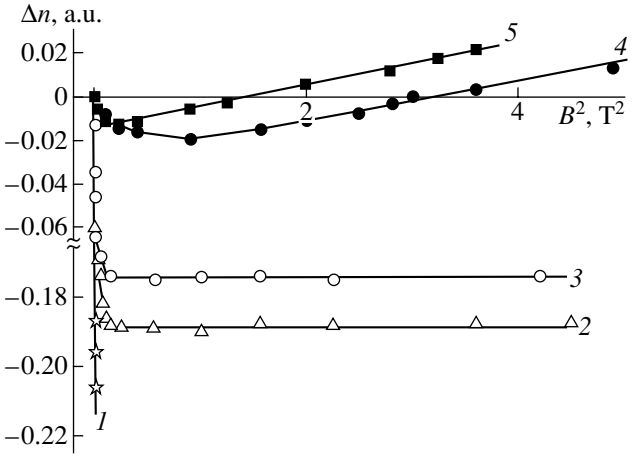

Fig. 2. The plots of magnetic-field-induced birefringence Δn versus squared magnetic induction B^2 for the aqueous suspensions of carbon materials: (*1–3*) suspension of graphite and graphitelike particles measured 1, 2, and 5 days after sample preparation; (*4, 5*) suspension of a cathode deposit containing up to 5% of multi-walled carbon nanotubes with a length to diameter ratio above 5, measured 3 and 6 days after preparation.

whereas the remaining part of the substance represented graphitelike nanostructures. In these mixtures, the total magnetooptical effect can be considered as a superposition of two contributions with opposite signs. In weak fields, the negative magnetic birefringence of graphitelike structures is dominating. As the field strength increases, the rapidly growing (quadratic in the field strength) birefringence component due to the multiwalled nanotubes begins to prevail (Fig. 2, curves *4* and *5*).

Thus, we have established a qualitative difference in the behavior of the magnetic birefringence in suspensions of carbon materials with and without multiwalled nanotubes. This phenomenon can serve as a basis of the method of determining the content of such nanotubes in carbon materials.

Sedimentation of the particles containing only graphitelike structures leads to a decrease in the negative birefringence component with time (Fig. 2, curves *1–3*). The effect observed in a suspension of materials containing nanotubes also varies with time (cf. curves *4* and *5*), but this is manifested by a shift of the Δn versus B^2 curves toward positive birefringence. This trend is indicative of an increase in the fraction of particles producing a positive contribution to the total birefringence. Thus, the suspension exhibits enrichment with nanotubes, which is related to a lower sedimentation rate of such particles as compared to that of the other material.

Acknowledgments. The authors are grateful to the Astrin Inc., the Fullerene Technologies Company, and the Radium Institute for kindly providing samples for this investigation.

REFERENCES

1. V. N. Tsvetkov, *Rigid Chain Polymers* (Nauka, Leningrad, 1986; Plenum Press, New York, 1989).
2. V. N. Tsvetkov, I. P. Kolomiets, A. V. Lezov, *et al.*, Vysokomol. Soedin., Ser. A **25**, 1327 (1983).
3. V. N. Tsvetkov, G. N. Kudryavtsev, E. I. Rjumtsev, *et al.*, Dokl. Akad. Nauk SSSR **224**, 398 (1975).

Translated by P. Pozdeev

Technical Physics Letters, Vol. 29, No. 2, 2003, pp. 147–150. Translated from Pis'ma v Zhurnal Tekhnicheskoĭ Fiziki, Vol. 29, No. 4, 2003, pp. 39–45.

A Method for Monitoring Thicknesses of Nanodimensional Bilayer Film Structures

A. I. Stognij, N. N. Novitskii, and O. M. Stukalov

"Zavod Transistor" State Unitary Enterprise, "Integral" Corporation, Minsk, Belarus

Institute of Solid State and Semiconductor Physics, National Academy of Sciences of Belarus, Minsk, Belarus

e-mail: stognij@ifttp.bas-net.by

Received September 16, 2002

Abstract—We describe an atomic force microscopy technique for rapidly monitoring the nanodimensional thicknesses of ultrathin mono- and bilayer films sputter deposited at oblique incidence onto a porous glass substrate with smooth areas between pores. Bilayer films were obtained using the second target arranged at an angle 10°–15° greater than that of the first target relative to the substrate. The images of such films clearly display the interfaces between pore edge and film, as well as between upper and lower layers of the film. This allows the total film thickness and the separate layer thicknesses to be determined by measuring the heights of steps between pore edge and layer surfaces on the sample relief cross section. *© 2003 MAIK "Nauka/Interperiodica".*

Thickness is the main parameter of thin films. Conventional methods used for directly determining film thicknesses are based on the measurement of height differences between the film–substrate interface and the film surface (or the film–film interface in multilayer structures). For this purpose, a cross section of the film sample structure was prepared by various means (e.g., by cleavage, scratching, or etching) and examined in a microscope [1, 2]. However, this approach can hardly be implemented for layers of nanodimensional thicknesses, where it would be difficult, besides measuring the positions of interfaces, to determine the influence of rough transition regions on the accuracy of measurements [3]. At the same time, nonuniform filling of the hills and valleys of a substrate relief on the initial film deposition stage introduces significant uncertainty into the calculations of film thicknesses based on indirect data (e.g., on the calibration curves of film thickness versus deposition time constructed for thicker films [4]).

As is known, nano- and subnanodimensional inhomogeneities of the surface relief can be successfully studied by atomic force microscopy [5]. As is demonstrated below, an atomic force microscope (AFM) allows a characteristic cross section image to be obtained for both mono- and bilayer film structures deposited onto a substrate surface exposing pores with sharp edges and smooth areas free of pores. Using these images, the layer thicknesses can be monitored by examining the general appearance or by measuring the height of steps on the sample relief cross section.

The sample film structures were studied and the film thicknesses evaluated with the aid of a Femtoskan-001 atomic-force microscope (AFM) (Advanced Technology Center, Moscow State University) with a 5×5 μm scanned field area. The AFM was operated in a contact regime using silicon cantilevers with a point radius of 10 nm, a cone angle of 20°, and a length of 50 μm (MicroMash Company, www.spmtips.com). The sample film structures were prepared using an ion beam deposition system described elsewhere [4, 6]. Metal films were deposited by sputtering the corresponding targets in an argon atmosphere. When depositing bilayer films, the second target was arranged at an angle 10°–15° greater than that of the first target relative to substrate. The sputtered material was deposited onto glass plates (Ilmglas type) with dimensions $22 \times 22 \times 0.2$ mm.

Figure 1a shows a typical AFM image of the initial glass substrate surface and the corresponding cross section profile measured along the line indicated on the image. As can be seen, the surface is continuous and the peak-to-peak height of the relief for some protrusions reaches 16 nm. Prior to film deposition, the glass surface was subjected to planarization through bombardment with 0.6-keV oxygen ions at a beam current density of 0.4 mA/cm^2 for 40 min. As a result of this treatment, the substrate acquires the relief imaged in Fig. 1b. The surface contains a certain number of pores, differing in shape and size, and areas (smoothened as compared to the initial glass surface) free of pores. The peak-to-peak height of the relief on the smooth areas does not exceed 3 nm over a distance of 1 μm (see Fig. 1b, profile *1* measured along line *1*). Deep pores exhibit sharp edges, as can be seen on the AFM images and the corresponding cross sections (see profile *2* measured along line *2*).

The surface relief formation on the samples under ion bombardment is governed by two factors. First, by the surface sputtering, which exposes the sites where bubbles (naturally formed in the glass during synthesis)

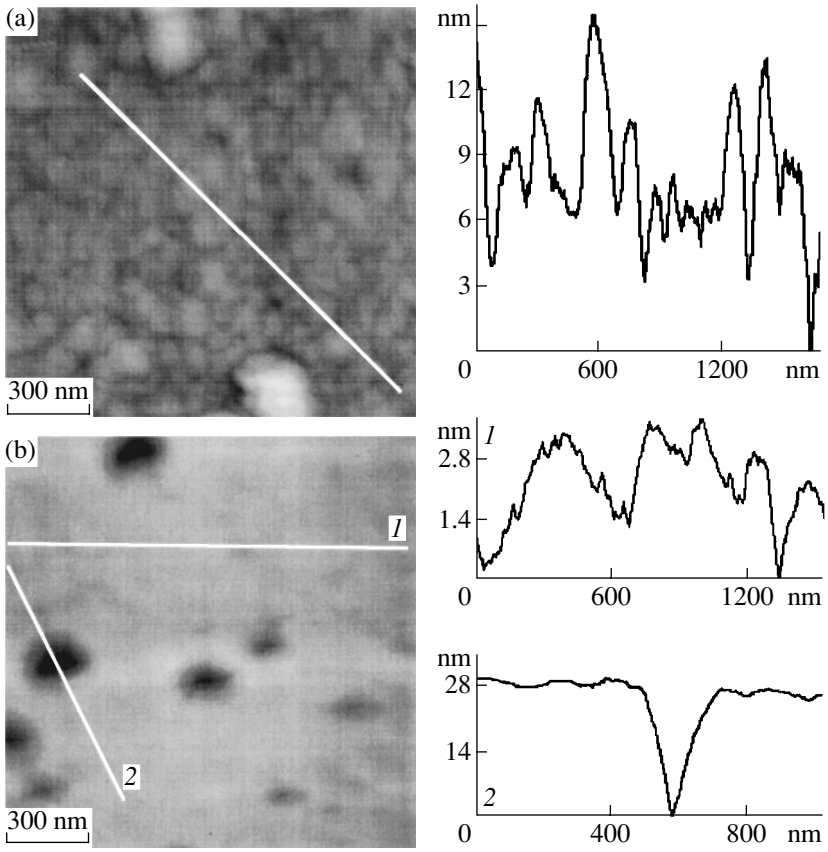

Fig. 1. AFM images of (a) an initial glass substrate and (b) a porous surface upon oxygen ion beam sputtering and the corresponding cross section measured along the indicated lines.

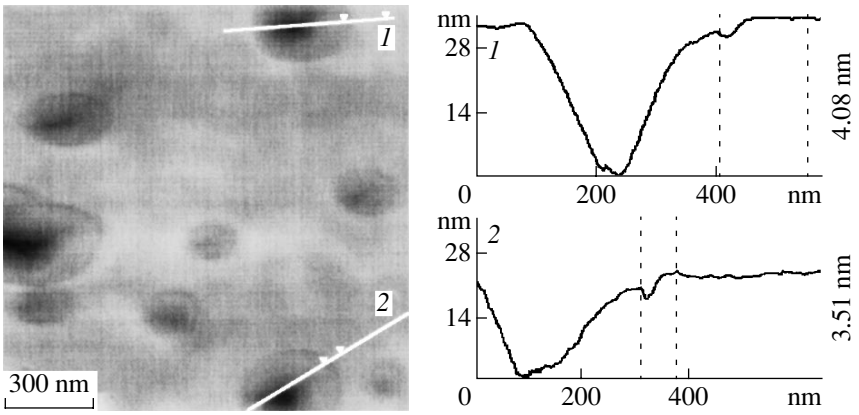

Fig. 2. An AFM image of a porous substrate surface coated with a gold film and the cross section measured along the indicated lines crossing open pores.

emerge at the surface thus opening pore [7]. The initial glass surface does not contain open pores, because special measures are taken to provide for their "healing" during the glass plate preparation. The second factor is smoothening of the initial surface relief as a result of prolonged bombardment with low-energy oxygen ions [4, 6].

Figure 2 gives an example of the AFM image of a gold film deposited onto a pretreated substrate surface. A comparison of Figs. 1 and 2 shows that pores revealed in the first case (see Fig. 1b) are more symmetric than those in the latter case, irrespective of the AFM scan direction. Additional steps observed in the relief cross section in the vicinity of pores (cf. Fig. 2 and

Fig. 1b) appeared as a result of gold deposition. The step size significantly exceeds the characteristic roughness dimensions on the areas of film and substrate free of pores. The step height (3.6 ± 0.5 nm) depends only slightly on the direction of the relief cross section in the vicinity of a pores, while the step width depends on this direction more significantly. In Fig. 2, maximum step widths are observed in the direction within the angle between lines *1* and *2*.

An analysis of the geometry of mutual arrangement of the target, substrate, and sputtered material flux (assuming that the latter flux is oriented in the direction determined by the condition that the angle of incidence of the primary beam is equal to the angle of preferential exit of the divergent beam of sputtered material [8]) shows that the direction determined by lines *1* and *2* in Fig. 2 is correlated with the direction of incidence of the sputtered material flux onto the substrate. The above results suggest that the step width depends on the direction of incidence of the sputtered material (determined by the mutual orientation of the target and substrate), while the step height corresponds to the film thickness. Previously, a gold film deposited under similar conditions was used as a passive layer in a study of the cobalt–copper interface [9]. Estimated from the deposition time, the gold film thickness (6 nm) was overstated as compared to the value determined by the step height. Taking into account the finite number of pores (Fig. 2), the reliability of a correlation between the step height and the film thickness can be increased by an analysis of this relation in the vicinity of pores of various shapes and dimensions.

Figure 3 shows the AFM image of a nickel–gold bilayer structure and the pore cross section profiles measured along the indicated lines. An increase in the total film structure thickness leads to a more asymmetric shape of pores as compared to those in Figs. 1 and 2. Moreover, the pore profiles measured along lines *1–3* in Fig. 3 display two steps with a total height of up to 21 nm. The upper step has a maximum height of 15.1 nm (on line *4*) and a minimum height of 12.2 nm (on line *2*). The height of the lower step varies from 6.4 to 7.1 nm. The cross section profile of a shallow pore measured along line *4* contains a single step, which is probably explained by a partial filling of shallow pores in the course of deposition of a thicker film.

The thickness of the bilayer structure presented in Fig. 3 can be estimated from an analysis of the AFM image. The total thickness of the bilayer structure does not exceed 22 nm; the upper (gold) film is 12–14 nm thick and the lower (nickel) film is 5–7 nm thick. An analogous nickel–gold bilayer structure, prepared with intermediate oxidation of the nickel layer, was deposited onto a magnesium doped gallium nitride with a *p*-type conductivity. As a result, we obtained an ohmic contact with a surface resistance of 5 Ω/□ and a transparency above 40% in the visible spectral range. The

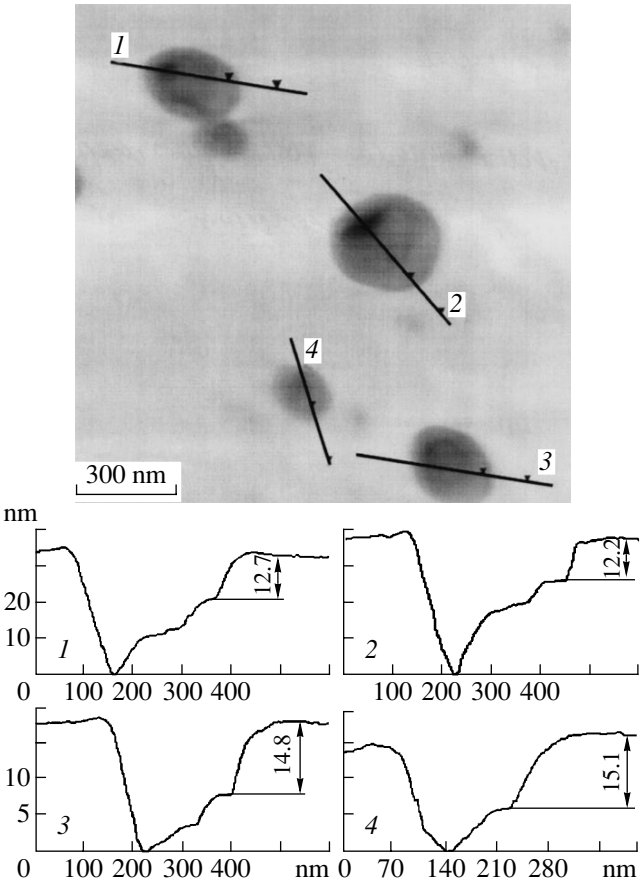

Fig. 3. An AFM images of a porous substrate coated with a nickel–gold bilayer film and the corresponding cross sections measured along the indicated lines crossing open pores.

parameters of these ohmic contacts were comparable to those reported in [10, 11].

It should be noted that the shape and resolution of the steps are determined primarily by the direction of incidence of the sputtered material during deposition of the first (lower) and second (upper) layers. Even during the analysis of a bilayer structure, the upper layer partly screens the step related to the lower layer in the cross section profile, which is caused by divergence of the deposited beam. This additional uncertainty of the AFM measurements can be evaluated by an analysis of the cross section profiles obtained for bilayer structures of various thicknesses. However, beginning with a three-layer structure, the uppermost layer screens the boundaries of several lower layers. This leads to difficulties in identification of the layer boundaries as determined only by the pore cross section relief.

Acknowledgments. The authors are grateful to Prof. M. Heuken (Vice-President of AIXTRON AG) for kindly providing gallium nitride samples and to Prof. G.P. Yablonskiĭ and E.V. Lutsenko (Institute of Physics, National Academy of Sciences of Belarus, Minsk) for fruitful discussions and constructive criticism.

This study was partly supported by the International Scientific-Technological Center, project no. B-176.

REFERENCES

1. L. C. Feldman and J. W. Mayer, *Fundamentals of Surface and Thin Film Analysis* (Elsevier Science Publishing, Amsterdam, 1986).
2. G. K.-B. Wehner, in *Methods of Surface Analysis*, Ed. by A. W. Czanderna (Elsevier, Amsterdam, 1975; Mir, Moscow, 1979).
3. V. S. Smentkowski, Prog. Surface Sci. **64**, 1 (2000).
4. A. I. Stognij, N. N. Novitski, and O. M. Stukalov, Pis'ma Zh. Tekh. Fiz. **28** (1), 39 (2002) [Tech. Phys. Lett. **28**, 17 (2002)].
5. A. A. Bukharaev, N. I. Nurgazizov, A. A. Mozhanova, and D. V. Ovchinnikov, Surface Sci. **482**, 1319 (2001).
6. A. I. Stognij, V. T. Svirin, S. D. Tushina, *et al.*, Prib. Tekh. Éksp. **44** (3), 151 (2001).
7. G. S. Khodakov and N. L. Kudryavtseva, *Physicochemical Principles of Glass Polishing* (Nauka, Moscow, 1985).
8. M. W. Thompson, Nucl. Instrum. Methods Phys. Res. B **18**, 411 (1987).
9. A. I. Stognij, N. N. Novitski, and O. M. Stukalov, *New Magnetic Materials for Microelectronics, Proc. 18th Int. Workshop Seminar* (Moscow, 2002), pp. 303–305.
10. J. K. Sheu, Y. K. Su, G. C. Chi, *et al.*, Appl. Phys. Lett. **74**, 2340 (1999).
11. Jin-Kuo Ho, Chang-Shyang Jong, Chien C. Chiu, *et al.*, Appl. Phys. Lett. **74**, 1275 (1999).

Translated by P. Pozdeev

Technical Physics Letters, Vol. 29, No. 2, 2003, pp. 151–153. Translated from Pis'ma v Zhurnal Tekhnicheskoĭ Fiziki, Vol. 29, No. 4, 2003, pp. 46–51.

Nanostructural Crack Arrest

V. A. Pozdnyakov

Bardin Institute of Ferrous Metals, State Scientific Center, Moscow, Russia

Received September 5, 2002

Abstract—The problem of brittle crack development in a nanocrystalline material has been theoretically studied. Expressions describing the conditions of crack stability are obtained. *© 2003 MAIK "Nauka/Interperiodica".*

The novel class of nanocrystalline materials (NCMs) has been extensively studied in the past decades [1, 2]. The main distinguishing features of the structure of NCMs are (i) ultimately small grain size and, accordingly, large volume fraction of a material occurring in the vicinity of the grain boundaries (GBs) and their junctions; (ii) hindered or suppressed dislocation mechanisms of the plastic deformation; and (iii) nonequilibrium state of GBs [1, 2]. Various anomalies in the deformation of NCMs related to dimensional effects have been discovered and studied [1–4].

GBs are the most important structural elements of NCMs, which determine to a considerable extent their macroscopic properties. Depending on the NCM technology (nanopowder compacting, mechanical alloying, nanocrystallization of amorphous alloys, intensive plastic straining), the resulting grain structure can occur in various nonequilibrium states characterized by different spectra of misorientation, defect types, and chemical compositions of GBs.

As is known, GBs may significantly influence the process of fracture in polycrystalline materials. Being the sites of stress concentration and reduced strength, GBs may facilitate crack nucleation and growth processes. NCMs possess high densities of GBs and their junctions and therefore must feature significantly more pronounced effects of GBs upon crack development as compared to those known in traditional materials.

Thomson *et al.* [5, 6] demonstrated that allowance for the discrete character of a crystal lattice in which a crack is developed gives rise to the so-called "lattice arrest" of the crack. According to this, there exists an interval of stresses close to the Griffiths stress where a crack can be stable.

Below, we consider the problem of a brittle crack development in NCMs and determine the effect of GBs and their junctions on the inter- and intragranular fracture. The possibility of realization of a "nanostructural arrest," a new effect possible in NCMs, is discussed.

Peculiarities of the brittle crack development in NCMs. The character of the crack development in a polycrystalline material and, hence, the conditions for realization of the inter- and intragranular fracture are determined by a relation between the energies of cohesive (γ_0) and grain-boundary (γ_e) fracture. Specific values of these energies are expressed as

$$\gamma_0 = 2\gamma, \quad \gamma_e = \eta(2\gamma + 2\gamma_s - \gamma_b), \tag{1}$$

where γ and γ_b are the specific energies of the free surface and GBs, respectively; γ_s is the energy of cleavage steps [7]; and η is the factor of nonuniformity of the fracture surface.

In usual polycrystalline materials, the contribution of GB junctions to the fracture energy is negligibly small and can be ignored in the fracture analysis [7]. The volume fraction of a material occurring in the region of GBs and their triple junctions grows with decreasing grain size. For NCMs, the volume fraction of such triple junctions becomes comparable with the volume fractions of GBs and intragranular material. Hence, the contribution of these junctions to the fracture energy can no longer be ignored.

For a random crack propagation path in a material, the effective fracture energy can be expressed as

$$\gamma_0^* = f_0\gamma_0 + f_b\gamma_e + f_j\gamma_j, \tag{2}$$

where f_0, f_b, and f_j are the fractions of the crack surface accounting for the intragranular material, GBs, and junctions, respectively; and γ_0, γ_b, and γ_j are the contributions from the corresponding structural components to the specific NCM fracture energy. A decisive factor in selecting the trajectory of the crack propagation (intragranular versus intergranular) is the relation between the partial specific fracture energies for the cracks propagating by these pathways.

If the plane of the crack propagation is perpendicular to the axis of the external stress σ and the crack apex deviates from the trajectory, the local stress coefficients k_1 and k_2 for a kinklike crack making an angle of θ with the main crack plane are [8]

$$\begin{aligned} k_1 &= \cos^3(\theta/2)K_1, \\ k_2 &= \sin(\theta/2)\cos^2(\theta/2)K_1, \quad K_1 = \zeta\sigma\sqrt{L}, \end{aligned} \tag{3}$$

1063-7850/03/2902-0151$24.00 © 2003 MAIK "Nauka/Interperiodica"

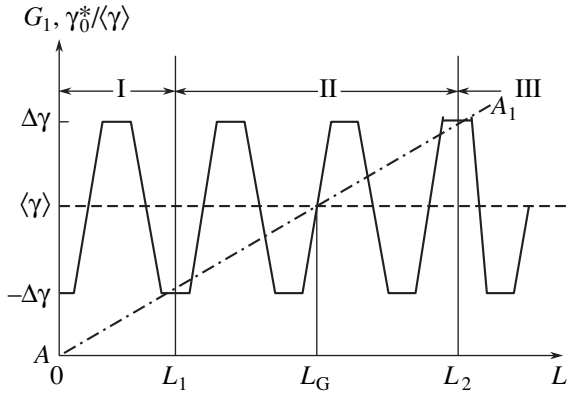

Plots of the energy dissipation rate G_1^* and specific fracture energy $\gamma_0^*/\langle\gamma\rangle$ versus crack pathlength (see the text for explanations).

where ζ is a numerical factor and L is the length of the main crack. Then, the condition for the crack propagation along a GB making an angle θ with the main plane (intergranular cracking) can be written as [8]

$$k_1^2 + k_2^2 \geq [2E\gamma_e/(1-\nu^2)], \quad (4)$$

where $E = 2\mu(1+\nu)$ is the Young modulus, ν is the Poisson ratio, and μ is the shear modulus. In contrast, for

$$K_1 \geq K_{1c} = [2E\gamma_0^*/(1-\nu^2)]^{1/2}, \quad (5)$$

the crack would propagate inside the grain to give rise to an intragranular type of fracture.

The intergranular fracture in NCMs is characterized by a large contribution of the linear tension of the crack surface to the total fracture energy. For a crack front bend or curvature with a small radius r, the fracture energy is

$$\gamma_e^* = \gamma_e + T/r, \quad (6)$$

where T is the linear tension at the crack front [9] and $2r \approx D$, D being the grain size.

A comparison of Eqs. (4) and (5) gives the condition for realization of the intragranular fracture, which actually appears as a mixed transintergranular fracture in NCMs due to a high volume fraction of the material in the GB region, during the straight crack propagation:

$$(\gamma_e^*/\gamma_0^*) \geq \cos^4(\theta_{\max}/2). \quad (7)$$

The reverse condition yields a local criterion of the intergranular fracture.

Nanostructural crack arrest. A high density of GBs and their junctions in NCMs hinders development of the purely intragranular fracture. The crack front, even for a straight crack trajectory, periodically passes via material in the grain bulk, GBs, and junctions, so that the fracture energy exhibits periodic variations. On a macroscopic scale, the intergranular fracture in NCMs can be considered as intragranular with a periodically varying fracture energy. Therefore, the specific fracture energy γ^* (fracture toughness G_c) is a periodic (quasiperiodic) function of the crack pathlength with a period approximately equal to the grain size D. Now let us consider the conditions for crack propagation in two- (2D) and three-dimensional (3D) approximations with allowance for the periodic variation of the fracture energy on the crack pathlength.

In a 2D model of cracking under planar straining conditions [10], the condition of crack propagation can be written in terms of reaching a critical rate G_{1c} of energy dissipation at the apex of a crack with a length of L:

$$G_1 = K_1^2(1-\nu^2)/E = \sigma^2\pi(1-\nu^2)L/E \geq G_{1c} = \gamma_0^*. \quad (8)$$

This yields a formula for the Griffiths crack length in a homogeneous continuum [10]

$$L_G = 4E\gamma_0^*/\pi(1-\nu^2)\sigma_f^2. \quad (9)$$

For $\gamma_0^* = \mu b/30$ (where b is the interatomic distance) and $\sigma_f = \mu/60$, this gives $L_G \approx 500b \gg D \approx 10$ nm.

Now let the effective fracture energy be a periodic function of the crack pathlength:

$$\gamma_0^*(L) = \langle\gamma\rangle + \Delta\gamma\sin(2\pi L/D), \quad (10)$$

where $\langle\gamma\rangle$ is the average value and $\Delta\gamma$ is the amplitude of oscillations of the fracture energy. For a crack of length L close to the Griffith value ($L = L_G + x$, $x \ll L_G$), Eqs. (8) and (10) yield a crack development condition (determined graphically as depicted in the figure) expressed through a dimensionless energy dissipation rate G_{1c}

$$G_1^* \equiv (\sigma^2 L/\sigma_G^2 L_G) = 1 + (\Delta\gamma/\langle\gamma\rangle)\cos(2\pi L/D). \quad (11)$$

In the plots of $G_1^*(L)$ and $\gamma_0^*(L)$, the points of intersection of the straight line AA_1 (representing $G_1^*(L)$ with the periodic profile of $\gamma_0^*(L)$ determine three possible scenarios of the crack development. In region I ($L < L_1$), cracks are unstable with respect to collapse, and in region III ($L > L_3$), with respect to dynamic propagation. In region II ($L_1 < L < L_2$, $L_2 - L_1 = \Delta L$), there are several thermodynamically stable (metastable) states for which $\Delta L/L_G \approx \Delta\gamma/\langle\gamma\rangle$.

Thus, for a periodically varying fracture energy γ_0^*, there appears a certain region of crack lengths (alternatively, for given crack length there appears a region of stresses $\sigma_1 < \sigma < \sigma_2$) in which the crack is stable (see figure).

In a 3D model, the change in the energy of an NCM body upon introduction of a disklike crack of radius r can be written as

$$\Delta E = 2\pi\gamma_e r^2 - (4\pi/3)r^3(\sigma^2/2E) + 2\pi r\Delta\Gamma\cos(2\pi r/D), \quad (12)$$

where $\Delta\Gamma$ is the amplitude of the fracture energy per unit crack front length. For $r = r^* + z$ ($z \ll r^*$), the force of resistance to the crack growth is

$$f_r = \frac{\partial\Delta E}{\partial r} = 4\pi\gamma_e r^*[2 + 3z/r^* + \pi(\Delta\Gamma/\gamma D)\sin 2\pi z/D]. \quad (13)$$

For the limiting stress ratio $Q = \sigma_2/\sigma_1$ in the lattice arrest interval, estimates yield (see [11] and references therein) $Q \le 1.05$–1.1, which indicates that the lattice arrest effect is small. For the proposed nanostructural arrest, we obtain

$$Q = (\sigma_2/\sigma_1) = 1 + \pi[\Delta\Gamma/\gamma_0^* D]. \quad (14)$$

For $\Delta\Gamma \approx \Delta\gamma D$ and $\Delta\gamma/\langle\gamma\rangle = 1.5$–$2$, this yields $Q = 5$–7 and implies that the effect can be significant. Thus, NCMs can feature the brittle crack propagation in a slow ("crawling" [6]) regime, whereby the crack front sequentially moves from one potential energy valley to another by forming kinklike cracks at the main crack front. Thus, high densities of GBs and their junctions can lead to some new effects in the development of cracks in nanocrystalline materials.

REFERENCES

1. H. Gleiter, Prog. Mater. Sci. **33** (4), 223 (1989).
2. R. A. Andrievskiĭ and A. M. Glezer, Fiz. Met. Metalloved. **89**, 91 (2000).
3. V. A. Pozdnyakov and A. M. Glezer, Pis'ma Zh. Tekh. Fiz. **21** (1), 31 (1995) [Tech. Phys. Lett. **21**, 13 (1995)].
4. V. A. Pozdnyakov and A. M. Glezer, Fiz. Tverd. Tela **44**, 705 (2002) [Phys. Solid State **44**, 732 (2002)].
5. R. Thomson, C. Hsieh, and V. Rana, J. Appl. Phys. **42**, 3154 (1971).
6. C. Hsieh and R. Thomson, J. Appl. Phys. **44**, 2051 (1973).
7. V. I. Trefilov, Yu. V. Mil'man, and V. A. Firstov, *Physical Principles of Strength of Refractory Metals* (Naukova Dumka, Kiev, 1975).
8. B. Cottrell and J. R. Rice, Int. J. Fract. **16** (2), 155 (1980).
9. A. G. Evans, Philos. Mag. **26**, 1327 (1972).
10. D. Broek, *Elementary Engineering Fracture Mechanics* (Noordhoff, Groningen, 1974; Vysshaya Shkola, Moscow, 1980).
11. A. A. Argon, Scr. Metall. **16** (3), 259 (1982).

Translated by P. Pozdeev

Technical Physics Letters, Vol. 29, No. 2, 2003, pp. 154–156. Translated from Pis'ma v Zhurnal Tekhnicheskoĭ Fiziki, Vol. 29, No. 4, 2003, pp. 52–57.

Determining the Energy Parameters of the Helium Accumulation Centers in Irradiated Boron Carbide from Thermodesorption Spectra

V. V. Svetukhin

Ul'yanovsk State University, Ul'yanovsk, Russia
e-mail: slava@sv.uven.ru

Received August 6, 2002

Abstract—A model for description of the thermodesorption spectra is proposed and used to determine the energy parameters of the centers of helium accumulation in neutron-irradiated boron carbide. It is shown that helium accumulation centers broken at 100–150°C are characterized by a breakage activation energy of 0.23 eV. These centers probably represent clusters or complexes of interstitial helium atoms. The helium accumulation centers broken at 800–1000°C have a breakage activation energy of 0.65–0.75 eV and probably represent helium–vacancy complexes (pores). *© 2003 MAIK "Nauka/Interperiodica".*

Despite extensive investigations of the process of radiation defect formation in boron carbide, the nature of such defects is still insufficiently understood: only defects of the helium–vacancy complex type can be considered as unambiguously identified [1]. The radiation-induced defect formation in boron carbide is related primarily to the production and accumulation of helium. Information concerning the defects related to helium can be extracted from experimental data on the helium thermodesorption from samples. These experiments are performed by heating an irradiated sample at a preset constant rate and measuring the rate of helium evolution from the sample. The resulting thermodesorption (TD) spectrum represents a plot of the gas evolution rate versus temperature.

Previously, Kovyrshin [2] studied the TD spectra of an irradiated B_4C powder and demonstrated the presence of helium accumulation centers of three types. The defect activation energies determined for these centers using a method proposed in [3], based on the TD peak temperatures, were equal to 0.3, 1.2, and 2.3 eV. However, this method can provide accurate data only based on a large number of measurements performed at various heating rates. The uncertainty of activation energies determined in [2] amounted to ~20%.

Below, a new method is proposed for determining the energy parameters from TD spectra measured at a single heating rate.

Let N be the concentration of helium atoms in accumulation centers of a certain type (e.g., clusters, complexes, or surface defects). In the range of temperatures employed in TD experiments, the probability of helium trapping by a defect is much smaller than the probability of detachment from this defect. The kinetics of helium loss from the tapping centers is described by the equation

$$\frac{dN(t)}{dt} = -g(T)N(t). \quad (1)$$

Let the temperature be increased at a constant rate β, so that

$$T = T_0 + \beta t. \quad (2)$$

Using this expression, it is possible to replace time with the temperature in Eq. (1):

$$\frac{dN(T)}{dT} = -\frac{g(T)}{\beta}N(T). \quad (3)$$

The temperature dependence of the kinetic factor g is expressed as

$$g(T) = g_0 \exp\left(-\frac{E_a}{kT}\right), \quad (4)$$

where E_a the activation energy for helium detachment from the defect; the preexponential factor g_0 is proportional to the concentration of centers N_c and depends on the geometry of these centers.

The solution to Eq. (3) can be written in the following form:

$$N(T) = N(T_0)\exp\left(-\int_{T_0}^{T}\frac{g(T_1)}{\beta}dT_1\right), \quad (5)$$

where T_0 is the heating start temperature and $N(T_0)$ is the initial concentration of helium at $T = T_0$.

In order to describe a TD spectrum, we have to determine the rate of gas evolution as a function of the

temperature, $\frac{dN}{dt} = \beta\frac{dN}{dT}$. Substituting expressions (5) and (4) into Eq. (3), we obtain

$$\frac{dN(T)}{dT} = \frac{N(T_0)g_0}{\beta}\exp\left(-\frac{E_a}{kT} - \int_{T_0}^{T}\frac{g(T_1)}{\beta}dT_1\right). \quad (6)$$

With neglect of the rate of helium evolution at temperatures below T_0, expression (6) can be rewritten as

$$\frac{dN(T)}{dT} = \frac{N(T_0)g_0}{\beta} \times \exp\left\{-\frac{E_a}{kT} - \frac{E_a g_0}{k\beta}\left[\frac{kT}{E_a}\exp\left(-\frac{E_a}{kT}\right) - Ei(1, E_a/kT)\right]\right\}, \quad (7)$$

where $Ei(1, x)$ is the Airy function. Expression (7) has a maximum at the temperature

$$T_{\max} = \frac{E_a}{2kLambert\left(\frac{1}{2}\sqrt{\frac{E_a g_0}{k\beta}}\right)}, \quad (8)$$

where $Lambert(x)$ is the Lambert function. Formula (8) yields a relation between the activation energy, the TD peak temperature, the kinetic coefficient g_0, and the heating rate β:

$$E_a = kT_{\max}Lambert\left(\frac{g_0 T_{\max}}{\beta}\right). \quad (9)$$

Another useful relation is

$$\frac{g_0}{\beta} = \frac{E_a}{kT_{\max}^2}\exp\left(\frac{E_a}{kT_{\max}}\right). \quad (10)$$

Substituting this formula into Eq. (7), we obtain a final expression for the TD spectrum:

$$\frac{dN(T)}{dT} = N(T_0)\frac{E_a}{kT_{\max}^2}\exp\left\{\frac{E_a}{k}\left(\frac{1}{T_{\max}} - \frac{1}{T}\right)\right\} \times \exp\left\{-\frac{E_a T}{kT_{\max}^2}\exp\left(\frac{E_a}{k}\left(\frac{1}{T_{\max}} - \frac{1}{T}\right)\right)\right\} \times \exp\left\{\frac{E_a^2}{k^2T_{\max}^2}Ei(1, E_a/kT)\exp\left(\frac{E_a}{kT_{\max}}\right)\right\}. \quad (11)$$

This expression provides for a convenient description of the results of TD measurements, since $T_{\max}$ is readily determined from the experimental spectrum. Upon normalization of the TD intensity to unity, the only fitting parameter is the activation energy. The proposed description is more accurate as compared to the method developed in [3], where determination of the activation energy involves both measurements of the TD peaks at various heating rates and description of the TD curve shape.

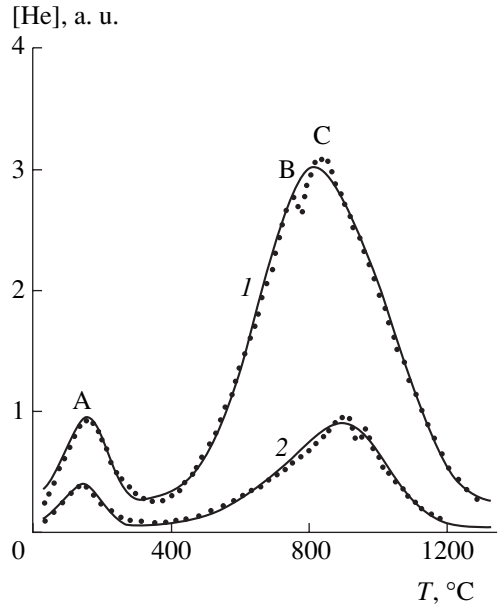

TD spectra of helium in boron carbide irradiated with neutrons to a total fluence of (*1*) 9×10^{19} cm^{-2} and (*2*) 1.2×10^{19} cm^{-2}: points represent the experimental data obtained at a heating rate of 0.3 K/s [2], solid curves show the results of calculations using formula (11).

Formula (11) was used to process the TD spectra of helium in irradiated boron carbide reported in [2]. The results obtained for samples irradiated with neutrons to a total fluence of 1.2×10^{19} and 9×10^{19} cm^{-2} are presented in the figure. The low-temperature TD peak is well described by formula (11) with an activation energy of $E_A = 0.23$ eV. The high-temperature peak, having a complicated shape, can be satisfactorily described assuming that it represents a superposition of two components with the activation energies $E_B = 0.65$ eV and $E_C = 0.75$ eV. The solid curves show the total helium evolution rates from centers of the A, B, and C types, calculated by formula (11) with the activation energies indicated above.

The close values of the activation energies and the temperature intervals of helium desorption (defect breakage) observed for the centers of types B and C suggest that these centers possess related structures. Probably, centers B and C have close compositions but differ in dimensions or geometry (spatial arrangement). In this interpretation, it is expedient not to distinguish between the helium accumulation centers of types B and C and consider these defects jointly as a single type characterized by an activation energy of 0.65–0.75 eV.

Thus, it is suggested that the TD spectra reveal defects of two types. An analogous situation was observed in the TD spectra of silicon carbide implanted with helium ions [4], where the peak observed at lower temperatures was attributed to the breakage of clusters composed of interstitial helium atoms, while the high-temperature peak (also possessing a complicated structure) was explained by helium liberation from helium–vacancy complexes (pores). Assuming that the nature of defects in boron carbide is analogous to that in silicon carbide, the value of $E_A = 0.23$ eV corresponds to the activation energy of detachment of a helium atom from a cluster or complex of interstitial helium atoms, while $E_B = 0.65$–0.75 eV corresponds to the activation energy of the helium yield from helium–vacancy pores.

REFERENCES

1. V. I. Shcherbak, V. I. Tarasikov, V. N. Bykov, and V. A. Rudenko, Atom. Énerg. **60** (3), 190 (1986).
2. V. G. Kovyrshin, Atom. Énerg. **53** (2), 112 (1982).
3. A. C. Damask and G. J. Dienes, *Point Defects in Metals* (Gordon and Breach, New York, 1963; Mir, Moscow, 1966).
4. E. Oliviero, A. van Veen, A. V. Fedorov, *et al.*, Nucl. Instrum. Methods Phys. Res. B **186**, 223 (2000).

Translated by P. Pozdeev

Technical Physics Letters, Vol. 29, No. 2, 2003, pp. 157–159. Translated from Pis'ma v Zhurnal Tekhnicheskoĭ Fiziki, Vol. 29, No. 4, 2003, pp. 58–62.

Critical Velocities of a Twisted Domain Wall in Very Thin Magnetic Films

G. E. Khodenkov

Institute of Electronic Control Computers, Moscow, Russia

e-mail: angeline@mtu-net.ru

Received September 6, 2002

Abstract—An integro-differential variant of the Slonczewski equations has been formulated so as to take into account the effect of a nonlocal magnetostatic field on the structure of twisted domain walls (TDWs) in films of very small (below DW width) thicknesses. Apart from the features specific to magnetic multilayer films, the limiting TDW velocity in this range of film thicknesses is very low (despite the small DW twist) and the TDW dynamics has a predominantly precessional character. For film thicknesses above the DW width, a maximum peak velocity determined by numerical methods has proved to be 20% higher than the well-known Walker's value. *© 2003 MAIK "Nauka/Interperiodica".*

This communication addresses the dynamics of twisted domain walls (TDWs) inherent in magnetic films of small thicknesses possessing a perpendicular anisotropy with a quality factor of $Q > 1$ (see [1]). Such films are considered as promising media for a system of perpendicular data recording with increased (compared to the conventional parallel mode) density intended for hard disks (see, e.g., [2]). Theoretical results obtained in this field, besides their immediate implications, may provide an estimate of continuum limits for the corresponding magnetic multilayer systems extensively studied now. Naturally, the DW types in multilayer systems exhibit a greater diversity (see, e.g., [3, 4]); moreover the DW dynamics in the range of extremely small layer thicknesses can be determined by factors not taken into account in the continuum approximation.

Let us consider magnetic films with thicknesses h in the interval $a < h < \Lambda$. For the sake of convenience, this interval is divided below into two:

$$\text{(a)}\quad a < h < \Delta \equiv \sqrt{A/K}, \tag{1a}$$

$$\text{(b)}\quad \Delta \le h \le \Lambda \equiv \sqrt{A/2\pi M^2} \equiv \sqrt{Q}\Delta, \tag{1b}$$

where a is the lattice constant; Δ and Λ ($\Delta < \Lambda$) are the Bloch DW and the Bloch linewidth, respectively; A, $K > 0$ are the inhomogeneous exchange and uniaxial anisotropy constants, respectively; and M is the magnetization. In region (1b), the inhomogeneous part of the exchange interaction does not admit large twist angles in the DW structure. According to the results of variational calculations [5], this structure is close to that of a one-dimensional Bloch DW (an analytical theory of TDWs was developed in [6, 7]). In region (1a), the situation is generally the same, but the magnetostatic energy can no longer be approximated by a one-dimensional expression $2\pi M_n^2$ (n is the normal to the DW plane) applicable in case (1b). Below, the effect of a nonlocal magnetostatic field on the TDW structure will be described using an integro-differential variant of the Slonczewski equations formulated so as to apply to both (1a) and (1b) intervals.

For the azimuthal angle $\psi(z)$ of the magnetization vector at the TDW center, the usual Slonczewski equation [1] is generalized to

$$V = -\varepsilon^2\psi''(z) + \cos\psi(z) \times \left[\int_{-1}^{1} G_\delta(z - z_1)\sin\psi(z_1)\,dz_1 - H_\delta(z)\right] \tag{2}$$

with the boundary conditions $\psi'(z = \pm 1) = 0$ on both film surfaces. Here, V is the TDW velocity normalized to $2V_w$ ($V_w = 2\pi M\gamma\Delta$ is Walker's velocity), $\gamma > 0$ is the gyromagnetic ratio, z is the dimensionless coordinate (related to $h/2$, so that $-1 < z < 1$), and $\varepsilon = 2\Lambda/h$ and $\delta = 2\Delta/h$ are important parameters of the theory determining the character of solutions of Eq. (2).

It is necessary to make some comments on the origin of the integral kernel in Eq. (2),

$$G_\delta(z) = \ln(1 + \delta^2/z^2)/2\pi\delta, \tag{3}$$

the more so that other representations can be encountered as well (see, e.g., [8]). Consider a contribution to the magnetostatic interaction energy expressed as

$$\int_{-h/2}^{h/2} dz\,dz_1 \int_{-\infty}^{\infty} dy\,dy_1 \frac{\partial M_y(y, z)}{\partial y}\frac{\partial M_y(y_1, z_1)}{\partial y_1} \times \ln\frac{1}{\sqrt{(z - z_1)^2 + (y - y_1)^2}},$$

1063-7850/03/2902-0157$24.00

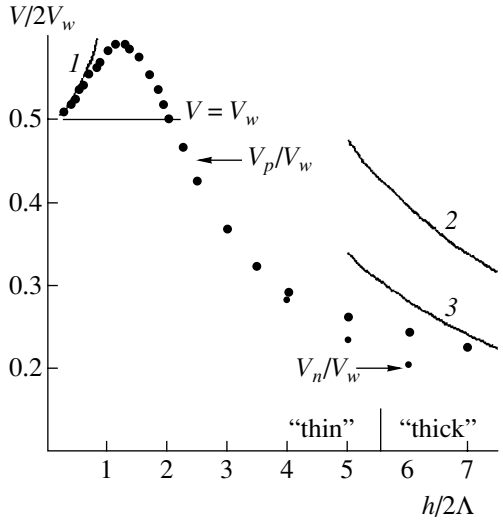

Figure.

where $M_y(y, z) = M\sin\theta(y)\sin\psi(z) \approx M\sin\psi(z)/\cosh(y/\Delta)$ is the magnetization component perpendicular to the DW planes, written in the approximation used in deriving the Slonczewski equations [1]. The magnetic dipole proportional to $\sim\frac{\partial}{\partial y}\frac{1}{\cosh y\Delta}$ can be represented via the δ function as $\delta(y + \Delta) - \delta(y - \Delta)$, which leads to expression (3). Note that kernel (3) coincides with the kernel of the integro-differential equation for a Neél DW in thin permalloy films [9] and, in contrast to the case of [8], exhibits the correct asymptotic behavior $G_\delta(z \longrightarrow \infty) \longrightarrow 1/z^2$ corresponding to the field of a linear dipole. In region (1b), $\lim_{\delta \to 0} G_\delta(z) = \delta(z)$ and Eq. (2) transforms into the well-known differential equation [1]. A demagnetizing film (responsible for the twist) from poles on the film surface exhibits no divergence upon averaging over the DW width:

$$H_\delta(z) = \frac{1}{4}\ln\frac{(1+z)^2 + \delta^2}{(1-z)^2 + \delta^2}. \qquad (4)$$

Let us first consider the region of ultimately small thicknesses (1a), where the condition $\delta = 2\Delta/h \geq 1$ allows the coefficients in Eq. (2) to be expanded into series in $1/\delta$:

$$G_\delta(z) \longrightarrow [2\pi\ln\delta - \ln z^2 + z^2/\delta^2]/2\pi\delta + O(1/\delta^5),$$
$$H_\delta(z) \longrightarrow z/\delta^2 + O(1/\delta^4). \qquad (5)$$

Let us introduce the parameter $\lambda = 1/\varepsilon^2 \ll 1$ ($\varepsilon = 2\Lambda/h$) and (by analogy with [7]) seek for a solution to Eq. (2) in the form of series $\psi(z) = \psi_0 + \lambda\psi_1(z) + \ldots$ and $V = V_0 + \lambda V_1 + \ldots$. The zero-order equation $\psi_0''(z) = 0$ together with the boundary conditions $\psi_0'(\pm 1) = 0$ shows that the zero-order solution ψ_0 is a constant (influencing the subsequent approximations). In the first-order approximation, we obtain the following equation:

$$\psi_1'' = -V_0 - \frac{z}{\delta^2}\cos\psi_0$$
$$+ \left[\frac{2\ln\delta}{\pi\delta} - \frac{1}{2\pi\delta}\int_{-1}^{1}\ln(z - z_1)^2 dz_1\right]\sin\psi_0\cos\psi_0. \qquad (6)$$

Integrating Eq. (6) in the interval $-1 < z < 1$ and taking into account that $\psi_1'(\pm 1) = 0$, we obtain an expression for the DW velocity in the first-order approximation (upon selecting a DW with $0 < \psi_0 < \pi/4$):

$$V = \sin\psi_0\cos\psi_0(2\ln\delta + 3 - 2\ln 2)/\pi\delta. \qquad (7)$$

Thus, the peak velocity V_p (analogous to Walker's velocity: in Eq. (7), $\psi_0 = \pi/4$) in the limit of weak influence of the magnetic dipole interaction is small $\sim V_w\ln\delta/\delta$. The contribution due to twist (reflected by the second term on the right-hand side of (6)) is very small ($\sim\lambda/\delta^2$). If the driving field strength exceeds V_p/μ (where μ is the DW mobility), the TDW dynamics acquire a precession character. It should be noted, however, that the above results can miss some factors specific to region (1a) (see, e.g., [3, 4]), effects of the magnetoelastic interactions [10, 11], and a change in the damping parameter [12].

In concluding, let us consider the TDW dynamics in region (1b) of the film thicknesses ($\delta < 1$), where Eq. (2) transforms into an ordinary differential equation. In contrast to the variational calculation [5], a numerical solution for kernel (3) was obtained by method of relaxation or (in certain cases) shooting.

For region (1b), the results of calculations of the limiting peak velocity V_p and the nucleation velocity V_n at which the first horizontal Bloch line (HBL) is generated within the TDW (with neglect of a small hysteresis [1]) are depicted by points in the figure. At $\varepsilon \sim 1$, the velocity V_p exhibits a clearly pronounced maximum, being greater than Walker's value approximately by 20%. This is much greater as compared to the values reported in [5] (see also [1, Fig. 17.4]). The solid curve *1* in the figure represents a theoretical curve corresponding to [7]

$$V/V_w = [1 + (1 + \ln 2)/6\varepsilon^2], \qquad (8)$$

which agrees satisfactorily with the results of our numerical calculation. Note that the limiting value of the angle $\psi(z)$ obtained in [7] (upon substituting $\psi = \pi/4$ and $C_2 = 0$ into [7, Eq. (13a)]) also agrees (to within a few percent) with our calculation. Hubert [5] introduced a critical value of $\varepsilon = 0.18$ ($h/\Lambda \sim 11$) below which no HBL nucleation takes place (indicated by the thin/thick mark in the figure). The results of calculations indicate that the HBL nucleation ceases in the

films with somewhat greater values of ε ($\varepsilon \geq 0.25$). The solid curve *2* in the figure represents the plot of $V_p/V_m = 9.5\Lambda/h$ according to Slonczewski [1], representing "thick" films, and curve *3* refers to the result $V_h/V_w = 6.8\Lambda/h$ obtained in [13].

REFERENCES

1. A. P. Malozemoff and J. C. Slonczewski, *Magnetic Domain Walls in Bubble Materials* (Academic, New York, 1979; Mir, Moscow, 1982).
2. A. Hubert and R. Schaefer, *Magnetic Domains. The Analysis of Microstructures* (Springer-Verlag, Berlin, 1998).
3. M. Labrune and J. Miltat, J. Magn. Magn. Mater. **151**, 231 (1995).
4. V. V. Kostyuchenko, Fiz. Tverd. Tela **44**, 93 (2002) [Phys. Solid State **44**, 98 (2002)].
5. A. Hubert, J. Appl. Phys. **46**, 2276 (1975).
6. A. P. Tankeev and O. G. Strashnikov, Fiz. Met. Metalloved. **53**, 257 (1982).
7. G. E. Khodenkov, Fiz. Met. Metalloved. **5**, 37 (1984).
8. T. Fujii, K. Kumosaki, and M. Inoue, Jpn. J. Appl. Phys. **19**, 1913 (1980).
9. A. Hubert, *Theorie der Domanenwande in Geordneten Medien* (Springer-Verlag, Berlin, 1974; Mir, Moscow, 1977).
10. A. L. Sukstanskii and V. V. Tarasenko, Zh. Éksp. Teor Fiz. **112** (4), 76 (1997) [JETP **85**, 804 (1997)].
11. K. V. Lamonova, A. L. Sukstanskii, and V. N. Vargukhin, Phys. Rev. B **60**, 10262 (1999).
12. L. Berger, J. Appl. Phys. **90**, 4632 (2001).
13. G. E. Khodenkov, Fiz. Tverd. Tela **33**, 2286 (1991) [Sov. Phys. Solid State **33**, 1288 (1991)].

Translated by P. Pozdeev

Technical Physics Letters, Vol. 29, No. 2, 2003, pp. 160–163. Translated from Pis'ma v Zhurnal Tekhnicheskoĭ Fiziki, Vol. 29, No. 4, 2003, pp. 63–70.

On the Possibility of Increasing the Automodulation Threshold in a Gyro-Oscillator with Backward-Wave and Coupled Electrodynamic Systems

A. A. Koronovskiĭ[a] and A. E. Khramov[b]*

[a] *Saratov State University, Saratov, Russia*
[b] *State Scientific Center "College," Saratov, Russia*
* *e-mail: aeh@cas.ssu.runnet.ru*

Received July 29, 2002

Abstract—We have studied the possibility of increasing the onset threshold for automodulation caused by a growth in the beam current in gyro-backward-wave tubes. It is shown that, by using a coupled electrodynamic system, it is possible to significantly shift the region of threshold currents for the automodulation onset so as to increase the output power in a singe-frequency generation regime. © *2003 MAIK "Nauka/Interperiodica".*

In the past decade, problems related to generation and amplification of high-frequency (HF) radiation via interaction of helical electron beams with traveling wave tubes have received much attention [1–7]. The interaction of such an electron beam with an opposite wave in a gyro-backward-wave tube (gyro-BWT) provides for the possibility of creating an oscillator with the working frequency readily controlled by changing the longitudinal electron velocity or a static magnetic field [1, 8].

Unfortunately, gyro-BWTs are characterized by relatively low efficiencies, with a maximum on the order of 20% [7]. This is related to certain features of the interaction between oscillating electrons in the beam and the HF field in the interaction space, whereby the HF power is carried in the direction opposite to the beam and the oscillating electrons exhibit bunching in a strong output field. After rapidly bunching, the beam exhibits a rapid spreading, not transferring its energy to the field within this short period of time, and then a secondary phase bunch is formed along the system. As a result, gyro-BWTs are characterized by multihump current and field distribution profiles, which is explained by the multiple re-bunching of the electron beam. Accordingly, an increase in the system length or the beam current rapidly give rise to automodulation of the output signal and the generation spectrum becomes multifrequency [5, 7, 9].

In order to increase the efficiency and output power (determined by the working beam current) while retaining a single-mode generation regime, it is necessary to modify the field distribution along the system so as to provide that the field strength would be small at the output and had a single maximum in the vicinity of a collector, where the phase bunch of electrons could transfer a considerable part of its energy to the field. One possible way of solving this problem consists in providing conditions for a distributed power transfer by means of identical coupled waveguide systems (CWSs), with the electron beam passing through one of these systems [10].

Below, we will analyze the possibility of increasing the region of single-frequency generation in gyro-BWT with CWSs.

A nonstationary system of equations describing the gyro-BWT–CWS dynamics is as follows. The field amplitudes in two weakly coupled waveguide systems with the electron beam propagating through one (for definiteness, the first) of these are described by the equations (see, e.g., [7, 9])

$$\frac{\partial F_1}{\partial \tau} - \frac{\partial F_1}{\partial \xi} - \alpha_1 F_2 = -I_1, \quad (1)$$

$$\frac{\partial F_2}{\partial \tau} - \frac{\partial F_2}{\partial \xi} - \alpha_2 F_1 = 0, \quad (2)$$

where $F_{1,2}$ are the slowly varying complex dimensionless field amplitudes in the first and second CWSs, respectively; ξ and τ are the dimensionless longitudinal coordinate and time, respectively; and $\alpha_{1,2}$ are the coupling parameters. Note that the identity of the systems $|\alpha_1| = |\alpha_2| = \hat{\alpha}$ and the law of conservation of the power flux for $I_1 = 0$ imply that $\alpha_1 = -\alpha_2^* = j\hat{\alpha}$.

The amplitude I_1 of the HF beam current passing through one of the CWSs is defined as $I_1 = \frac{1}{2\pi}\int_0^{2\pi} \beta\, d\theta_0$, where $\beta = r\exp(j\theta)$ is the complex trajectory radius of

electrons in the helical beam. This radius is determined from the equation of motion [7]

$$\frac{d\beta}{d\xi} - j\mu(1-|\beta|^2)\beta = F_1, \quad (3)$$

where μ is the parameter of nonisochronicity of the oscillating electrons [7, 11]. Equations (1)–(3) have to be solved with the following initial and boundary conditions:

$$F(\xi = A) = 0, \quad F(\tau = 0) = f^0(\xi), \\ \beta(\xi = 0) = \exp(j\theta_0), \quad \theta_0 \in [0, 2\pi], \quad (4)$$

where A is the dimensionless length of the system. Expressions for the dimensionless quantities were introduced and simplifying assumptions underlying the proposed model were considered in detail elsewhere [7, 11].

The control parameters of the model are the system length A, the nonisochronicity parameter μ, and the coupling parameter $\hat{\alpha}$. In a system with a constant beam current I_0, the variation of A at a constant μ corresponds to a change in the system length l. At a constant length l, A is varied at the expense of current I_0 and the product μA remains constant.

Let us consider the gyro-BWT–CWS start conditions. Figure 1a shows plots of the parameter μ for which the gyro-BWT exhibits autoexcitation with steady-state generation versus the coupling coefficient $\hat{\alpha}$ for three values of the system length A. The value of μ was normalized to μ_0 corresponding to gyro-BWT excitation at $\hat{\alpha} = 0$. As can be seen from these curves, the introduction of coupling leads to an increase in the value of μ corresponding to the onset of autoexcitation as compared to the case of $\hat{\alpha} = 0$. Note that the $\mu(\hat{\alpha})$ plots appear as curves with a single maximum. As the system length A grows, the relative value of the "starting" parameter $\mu(\hat{\alpha})/\mu_0$ tends to decrease: the greater the A value, the lower lies the corresponding curve in the region of large $\hat{\alpha}$ values.

Let us consider the factors responsible for this behavior of gyro-BWT–CWS in the start regime. The system of Eqs. (1)–(3) can be written in the form corresponding to coupled waves:

$$\frac{\partial F_S}{\partial \tau} - \frac{\partial F_S}{\partial \xi} = -I_1 \exp[j\hat{\alpha}\xi], \quad (5)$$

$$\frac{\partial F_F}{\partial \tau} - \frac{\partial F_F}{\partial \xi} = -I_1 \exp[-j\hat{\alpha}\xi], \quad (6)$$

$$\frac{d\beta}{d\xi} - j\mu(1-|\beta|^2)\beta \\ = \frac{1}{2}(F_S \exp[-j\hat{\alpha}\xi] - F_F \exp[j\hat{\alpha}\xi]), \quad (7)$$

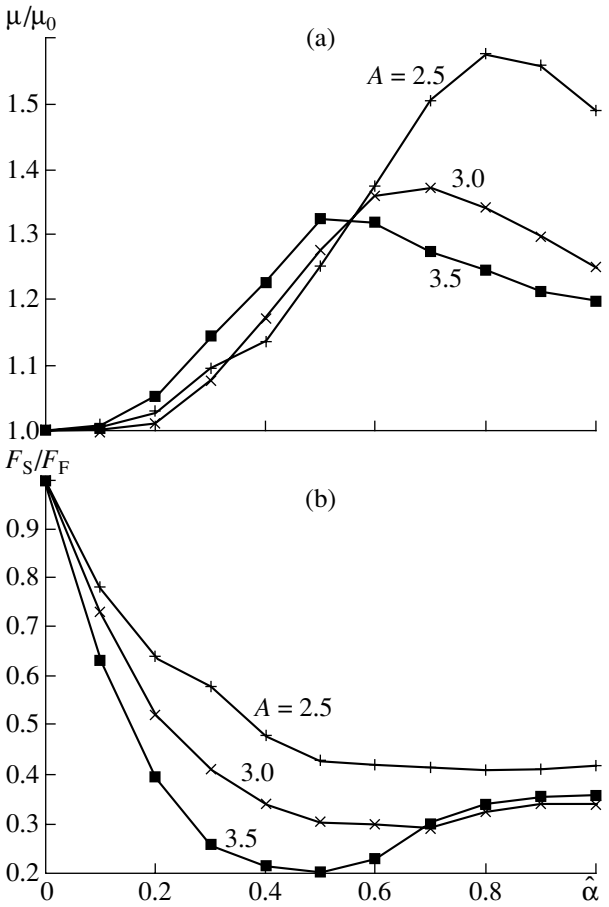

Fig. 1. Plots of (a) the nonisochronicity parameter μ for which the gyro-BWT exhibits autoexcitation and (b) the ratio of amplitudes F_S/F_F of the slow and fast normal waves at the system output (near the gyro-BWT autoexcitation threshold) versus the coupling coefficient $\mu(\hat{\alpha})$ for various values of the system length A.

where $F_S = F_1 + F_2$ is the amplitude of a "slow" normal wave (with the propagation constant $\beta_S = \beta_0 + \hat{\alpha}$, where β_0 is the propagation constant of the opposite wave at a "cold" synchronicity) and $F_F = F_2 - F_1$ is the amplitude of a "fast" ($\beta_F = \beta_0 - \hat{\alpha}$) normal wave in the coupled system.

Figure 1b shows plots of the ratio of amplitudes of the slow and fast normal waves (F_S/F_F) at the system output ($\xi = 0$) near the gyro-BWT autoexcitation threshold versus the coupling coefficient $\hat{\alpha}$ for various interaction space lengths A. A comparison of Figs. 1a and 1b leads to the conclusion that the maximum increase in the starting value of the nonisochronicity μ corresponds to minimum values of the F_S/F_F ration. This implies that an increase in the coupling coefficient leads to preferential excitation of the fast wave in the coupled electrodynamic systems, whereby the beam selectively interacts with the normal waves. The coupling resistance of each normal wave is half that of the

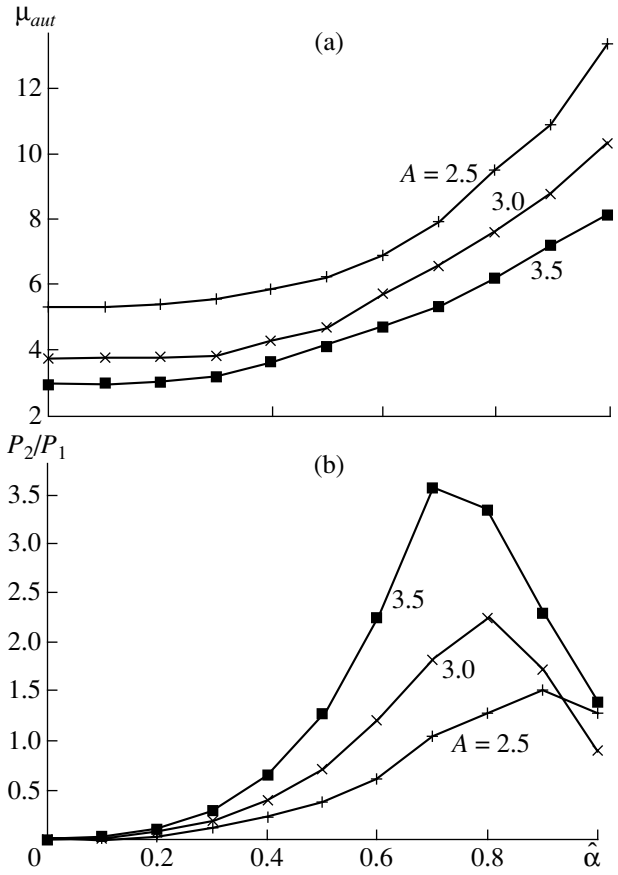

Fig. 2. Plots of (a) the parameter μ_{aut} corresponding to the onset of automodulation and (b) the ratio P_1/P_2 of the power fluxes in waveguide systems without and with the beam (near the gyro-BWT autoexcitation threshold) versus the coupling coefficient $\hat{\alpha}$ for various interaction space lengths A.

gyro-BWT with a single electrodynamic system (i.e., for $\hat{\alpha} = 0$). Therefore, the autoexcitation of a gyro-BWT with CWS requires an increase in the beam current as compared to that in the system with $\hat{\alpha} = 0$. In other words, excitation of the gyro-BWT (at a fixed system length A) requires an increase in the nonisochronicity parameter μ of the oscillating electrons.

Now let us study the boundary of the region of automodulation of the output signal in a gyro-BWT with CWS. Figure 2a shows plots of the parameter μ_{aut} corresponding to the onset of automodulation versus the coupling coefficient $\hat{\alpha} \approx 1.0$ for various interaction space lengths A. As can be seen from these data, the values of μ_{aut} significantly increase upon the introduction of coupling. The maximum relative growth is approximately the same for various A values: for example, $\mu_{aut}/\mu_{aut}(\hat{\alpha} = 0) \approx 2.52$, 2.77, and 2.76 for $A = 2.5$, 3.0, and 3.5, respectively.

It should also be noted that gyro-BWT–CWSs exhibit a change in the character of the automodulation onset. For $\hat{\alpha} = 0$, the automodulation starts "rigidly", possessing a finite amplitude already at $\mu = \mu_{aut}(\hat{\alpha} = 0)$. After the introduction of coupling ($\hat{\alpha} > 0.2$–0.4), the automodulation arises softly, starting with zero amplitude at the boundary $\mu = \mu_{aut}(\hat{\alpha})$ of the automodulation region and increasing in amplitude with the parameter μ.

Let us consider the factors responsible for this behavior of the automodulation region for gyro-BWT–CWSs. As is well known [9, 12], the appearance of the automodulation regimes in microwave devices with prolonged interaction is related to the formation of an additional distributed feedback in the system, whereby a helical electron beam bunched in a strong field arrives at a collector end of the system ($\xi = A$) in a re-bunched state with a velocity of $v_\parallel$; a field excited by the bunched beam current propagates at a velocity of v_g (v_g is the group velocity of the opposite electromagnetic wave in the waveguide) toward the input end of the system ($\xi = 0$); grouped in a weak field, the beam now excites a strong field in which the helical electron beam is re-bunched. As a result, the whole pattern is repeated in time with a period of $T \sim 2A(1/v_\parallel + 1/v_g)$, and the value of $T/2$ can be considered as a characteristic delay time of the additional feedback chain.

Upon the introduction of coupling between the two electrodynamic systems, the above additional feedback is suppressed, because the power of the opposite wave propagating with a group velocity v_g is now partly transferred to the system without helical beam. As a result, the boundary of the automodulation region shifts toward greater values of the nonisochronicity parameter μ (i.e., toward greater beam currents). This is illustrated in Fig. 2b, which shows plots of the ratio P_2/P_1 of the power fluxes in waveguide systems without and with the beam versus the coupling coefficient $\hat{\alpha} \in (0.0, 0.7)$. As can be seen from these data, an increase in the coupling coefficient leads to a rapid growth in the power "pumped" from the first to second system, so that $\sqrt{P_2/P_1} \sim \exp[\gamma\hat{\alpha}]$, where $\gamma = 1.2$–1.8 depending on the system length. For large coupling coefficients ($\hat{\alpha} > 0.7$), the power flux P_2 exhibits saturation. However, the value of $\mu_{aut}(\hat{\alpha})$ keeps increasing, because a significant power transfer from the opposite wave in the system with helical beam already begins close to the input ($\xi = A$), thus also favoring breakage of the additional feedback and causing a shift of the automodulation region.

Note that, simultaneously with the growth in $\hat{\alpha}$, the system with CWS exhibits an increase (by a factor of 1.2–1.4) in efficiency of the stationary generation regime, with a maximum reached at $\hat{\alpha} \approx 0.5$–0.6. This is related to fact that the field distribution established in the first waveguide system is optimum for the effective energy transfer from oscillating electrons in the helical beam.

Thus, the introduction of coupled waveguide systems into a gyro-BWT allows the boundaries of the regions of autoexcitation and automodulation to be shifted toward higher values of the beam current, which provides for a greater output power in a single-frequency generation regime.

Acknowledgments. This study was supported by the Russian Foundation for Basic Research, project nos. 01-02-17392 and 02-02-16351.

REFERENCES

1. K. L. Felch, B. G. Danly, H. R. Jory, *et al.*, Proc. IEEE **87** (5), 752 (1999).
2. J. Rodgers, H. Guo, G. S. Nusinovich, and V. L. Granatstein, IEEE Trans. Plasma Sci. **PS-48**, 2434 (2001).
3. G. S. Nusinovich, W. Chen, and V. L. Granatstein, Phys. Plasmas **8**, 631 (2001).
4. G. S. Nusinovich, O. V. Sinitsyn, and A. Kesar, Phys. Plasmas **8**, 3427 (2001).
5. G. S. Nusinovich, A. N. Vlasov, and T. M. Antonsen, Phys. Rev. Lett. **87**, 218301-1 (2001).
6. D. I. Trubetskov and A. E. Khramov, Pis'ma Zh. Tekh. Fiz. **28** (18), 34 (2002) [Tech. Phys. Lett. **28**, 767 (2002)].
7. A. Yu. Dmitriev, D. I. Trubetskov, and A. P. Chetverikov, Izv. Vyssh. Uchebn. Zaved., Radiofiz. **34** (9), 595 (1991).
8. Z. G. Chen and H. Döring, Int. J. Infrared Millim. Waves **5**, 691 (1984).
9. D. I. Trubetskov and A. P. Chetverikov, Izv. Vyssh. Uchebn. Zaved., Prikl. Nelineĭnaya Din. **2** (5), 3 (1994).
10. V. A. Isaev, V. L. Fisher, and A. P. Chetverikov, in *Lectures on Microwave Electronics and Radiophysics: Proceedings of 7th Winter School-Workshop of Engineers* (Saratovskiĭ Univ., Saratov, 1986), Part 2, p. 2.
11. A. Yu. Dmitriev, A. E. Konevets, L. A. Pishchik, *et al.*, in *Lectures on Microwave Electronics and Radiophysics: Proceedings of 7th Winter School-Workshop of Engineers* (Saratovskiĭ Univ., Saratov, 1986), Part 3, p. 61.
12. N. S. Ginzburg, S. P. Kuznetsov, and T. N. Fedoseeva, Izv. Vyssh. Uchebn. Zaved., Radiofiz. **21**, 1037 (1978).

Translated by P. Pozdeev

Technical Physics Letters, Vol. 29, No. 2, 2003, pp. 164–167. Translated from Pis'ma v Zhurnal Tekhnicheskoĭ Fiziki, Vol. 29, No. 4, 2003, pp. 71–80.

On the Synthesis of Radiation Spectrum in a Sectioned Relativistic Backward Wave Tube

N. S. Ginzburg, R. M. Rozental', and A. S. Sergeev

Institute of Applied Physics, Russian Academy of Sciences, Nizhni Novgorod, Russia

e-mail: rrz@appl.sci-nnov.ru

Received August 21, 2002

Abstract—We have studied the possibility of controlling the radiation spectrum of a high-power relativistic backward wave tube (BWT) by varying the period of its delay system. For a BWT comprising several sections with different corrugation periods, two- and three-mode generation regimes with commensurate amplitudes of spectral components have been found, the separation of which can be controlled by changing the corrugation period. It is shown that, for a sufficiently large detuning, such a configuration of the interaction space makes possible the generation of noiselike chaotic signals with separated or overlapping spectra. In the latter case, the width of the radiation spectrum is almost twice that of a regular BWT of the same length. © *2003 MAIK "Nauka/Interperiodica".*

The ability to generate high-power microwave radiation with a complicated spectrum is of practical interest in applications such as plasma heating and various communication and sounding systems. In connection with this, several methods for generating such radiation are extensively elaborated at present. Recently, we have realized generation in the automodulation regimes using a high-power backward wave tube (BWT) [1, 2]. Dumbrajs *et al.* [3, 4] modeled a two-frequency generation regime in a gyrotron operating in a millimeter wavelength range. However, the latter project is aimed at the simultaneous excitation of two modes with different transverse field structures, which may complicate practical use of such oscillators. Yang *et al.* [5] experimentally realized the two-frequency regime using an oscillator of the Cherenkov type by simultaneously pumping two electrodynamic systems with parallel electron beams. In the case of pulsed relativistic beams, an obvious disadvantage of this scheme is the necessity of synchronizing the beams and subsequent multiplexing of the output radiation.

We have studied the possibility of generating multifrequency signals using relativistic BWTs with an electrodynamic system pumped by a single beam. Below, we demonstrate that a regime of generation at several close frequencies with the same transverse field structure can be rather simply realized in a sectioned system with a stepwise variation of the synchronism detuning between the beam and the working wave. In the case of high-power relativistic BWTs with the electrodynamic systems representing sections of a corrugated waveguide, a stepwise change of the synchronism can be provided by variation of the corrugation period.

Let us consider a BWT model with an electrodynamic system in the form of a round corrugated waveguide excited by a tubular electron beam. In the approximation of relatively small changes in the electron energy in the course of the interaction, the dynamics of this BWT with a variable synchronism detuning are described by a system of self-consistent equations (cf. [6])

$$\frac{\partial A}{\partial \tau} - \frac{\partial A}{\partial \zeta} = -\frac{1}{\pi}\int_0^{2\pi} e^{-i\theta} d\theta_0,$$
$$\frac{\partial \theta}{\partial \zeta} = u + \Delta(\zeta)\frac{\partial u}{\partial \zeta} = -\mathrm{Re}\{Ae^{i\theta}\} \qquad (1)$$

with the initial and boundary conditions

$$A|_{\tau=0} = A_0(\zeta), \quad A|_{\zeta=L} = 0, \quad \theta|_{\zeta=0} = \theta_0 \in [0, 2\pi),$$
$$u|_{\zeta=0} = 0.$$

Equations (1) are written in terms of the following normalized variables: $\zeta = C\omega z/v_0\gamma_0^2$ is the longitudinal coordinate; L is the dimensionless length of the interaction space (in the same normalization); $\tau = C\omega(t - z/v_0)/\gamma_0^2(1 + v_0/v_{gr})$ is the time variable; $A = \gamma_0 eE_z/C^2\omega m v_0$ is the dimensionless amplitude of the synchronous spatial (–1)th harmonic of the radiation field; $\theta = \omega t + hz - \int_0^z \bar{h}(z)dz$ are the electron phases relative to the synchronous field harmonic; $\bar{h}(z) = 2\pi/d(z)$; $d(z)$ is the variable corrugation period; h is the modulus of the longitudinal wavenumber of the main spatial har-

monic; $u = (1 - \gamma/\gamma_0)/\beta_0^2 C$ is the relative variation of the electron energy;

$$\Delta(\zeta) \equiv \frac{\gamma_0^2 v_0}{\omega C}\left(\bar{h}(z) - h - \frac{\omega}{v_0}\right)$$

is the variable detuning of the synchronism between electron and the working wave; $C = (\gamma_0^3 eJ|Z|/2m v_0^2)^{1/3}$ is the Pierce parameter; $|Z|$ is the coupling impedance of the slow-wave harmonic [7]; J is the beam current; $\gamma = (1 - v^2/c^2)^{-1/2}$ is the relativistic mass factor of electrons; ω is the frequency of perfect synchronism (selected as the carrier frequency); v_0 is the initial longitudinal velocity of electrons; and $\beta_0 = v_0/c$.

The efficiency of the system is determined as $\eta = (\gamma_0 + 1)\gamma_0^{-1} C\tilde{\eta}$, where

$$\tilde{\eta} = (2\pi)^{-1}\int_0^{2\pi} u d\theta_0$$

is the reduced efficiency (the upper bar denotes averaging over time series). In deriving the system of equations (1), it was assumed that the wavenumber of the main spatial harmonic, the group velocity of the working wave v_{gr}, and the coupling impedance in various sections are the same. In addition, we employed a linear approximation of the dispersion characteristic of the electrodynamic system in the working frequency range.

For $\Delta(\zeta) \equiv$ const, the system of equations (1) describes the dynamics of a regular BWT [6, 8], in which case the system behavior is determined by a single parameter L (dimensionless length of the interaction space). The oscillator starts at $L \approx 2$ and changes the generation regime from stationary to a periodic automodulation (with a period of $T_{AM} \approx 1.5L$) at $L \geq 3$; as the interaction length grows further ($L \geq 5.5$), a stochastic automodulation regime is established. Note that the distance Δf between spectral components in the regime of periodic automodulation is restricted to the interval in which this regime is realized: $1/\Delta f = T_{AM}$. Both the amplitudes of satellite waves and the number of spectral components may significantly vary depending on the parameter L.

The introduction of a detuning step at the boundary of regular sections opens additional possibilities for the generation of multifrequency signals. Let the change of detuning in a two-section BWT be set in the following form: $\Delta(\zeta) = \Delta_1\chi(\zeta - L_1)$, where Δ_1 is the detuning step at the boundary between two sections, L_1 is the length of the first section, and $\chi(\zeta)$ is the Heaviside function. It should be emphasized that, from the standpoint of the interaction of electrons with the synchronous wave, a transition between sections can be considered as jumplike provided that the length is small as compared to the inverse increment. On the other hand, a change in the corrugation period can be adiabatic from the standpoint of electrodynamics, whereby the number of corrugation periods contained in the transition region is sufficiently large to eliminate significant reflections from this region. The results of modeling showed that a sufficiently large synchronism detuning between the two sections makes possible the generation at two separated frequencies. For two-frequency operation, the optimum total system length is $L = 6$–6.5. Since an unperturbed beam enters the first section, the length of this section is limited from below by a start length of the regular BWT and from above, by the length over which a stable generation regime loses stability.

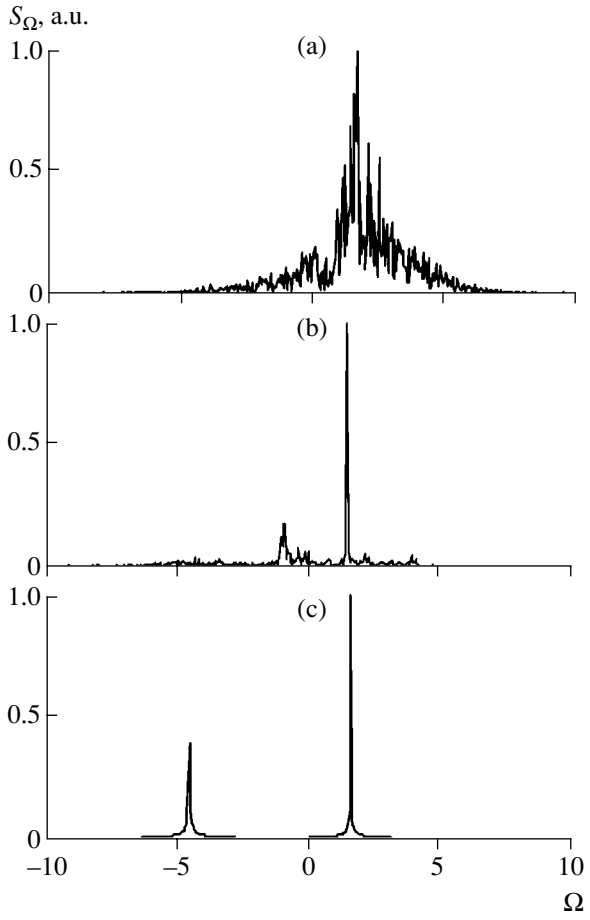

Fig. 1. Generation spectra of a two-section BWT ($L_1 = 2.4$, $L_2 = 1.5L_1$) for $\Delta_1 = -2$ (a), –4 (b), and –8 (c).

Figure 1 shows the spectra of an output signal of a two-section BWT with $L_1 = 2.4$ and $L_2 = 3.6$ observed as the negative synchronism detuning of the second section with respect to the first one sequentially increases in absolute value. At a relatively small detuning (Fig. 1a), the generation spectrum is almost identical to that of a regular BWT with the corresponding length (chaotic generation with continuous spectrum). An increase in the detuning leads to breakdown of the chaotic automodulation regime and establishing of a two-frequency regime with a relatively low level of the

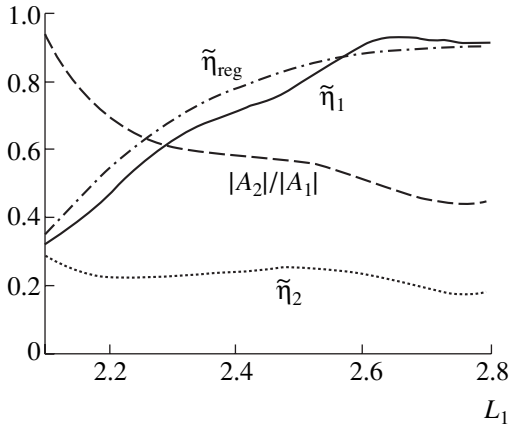

Fig. 2. Plots of the reduced efficiencies $\tilde{\eta}_{1,2}$ for a two-section BWT ($\Delta_1 = -10$) and the ratio of amplitudes of the spectral components $|A_2|/|A_1|$ versus the length of the first section in comparison to the reduced efficiency ($\tilde{\eta}_{reg}$) of a regular BWT as a function of its length.

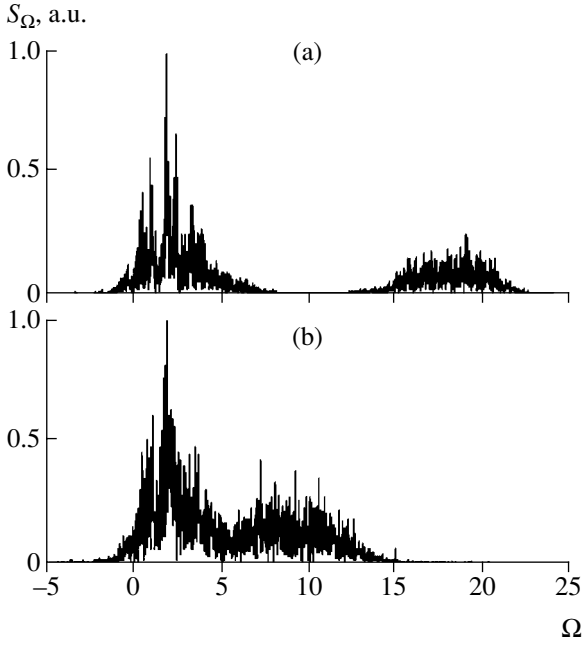

Fig. 3. Generation spectra of a two-section BWT ($L_1 = 6.3$; $L_2 = 11.7$) operating on an automodulation regime: (a) $\Delta_1 = 15$, separated spectra; (b) $\Delta_1 = 6$, overlapping spectra.

second spectral component (Fig. 1b). Further increase in the detuning is accompanied by an increase in the amplitude of the second signal (Fig. 1c), while the frequency difference in his model exhibits infinite growth in proportion to Δ_1. Analogous processes take pace for the positive values of the synchronism detuning between sections.

For the two-frequency generation regime, the reduced efficiency can be determined from the condition of conservation of the power flux in the form of $\tilde{\eta} = \tilde{\eta}_1 + \tilde{\eta}_2$, where $\tilde{\eta}_{1,2} = |A_{1,2}|^2/4$ is the relative energy yield from the electron beam in each section, and $A_{1,2}$ are the amplitudes of the spectral components. Figure 2 presents the plots of reduced efficiency ($\tilde{\eta}_{1,2}$) for both BWT sections and the ratio ($|A_2|/|A_1|$) of the amplitudes of the spectral components versus the length of the first section. The plots were constructed for a sufficiently large negative step in the synchronism detuning ($\Delta = -10$) and an optimum length of the second section (corresponding to maximum signal). As can be seen from Fig. 2, the efficiency of the second section is relatively small, because the electron beam entering this section is characterized by a significant energy scatter acquired after interaction with the first section. At the same time, the efficiency of the first section differs only slightly from that of a homogeneous BWT of the same length. Although radiation from the second section enters the first section, the frequency of this radiation is strongly shifted relative to the working frequency of the first section and this field is not synchronized with the electron flux. Thus, at a large frequency difference between sections, the influence of the second section on the first one is relatively small as compared to the reverse effect. For this reason, the efficiency of the second section $\tilde{\eta}_2$ exhibits a significant increase only in the region where the length of the first section is close to the start value, which is related to a decrease in the efficiency of generation in the first section, leading to a decrease in the effective scatter of electrons with respect to the energies and phases at the entrance of the second section. The amplitude of the second frequency component may even exceed that of the main frequency, which makes it possible to obtain a two-frequency signal with an arbitrary ratio of the component amplitudes.

It should be emphasized that it is possible, by increasing the total length of the interaction space and varying the lengths of sections in the delay system, to realize combinations of various dynamic regimes. For example, the first section can generate in a one-frequency regime, while the second operates in a regime of periodic or stochastic automodulation with a central frequency shifted relative to that of the first section. Naturally, it is also possible to provide for a regime whereby both sections generate chaotic signals with separated frequencies. Figure 3 shows the generation spectra of a two-section BWT with $L = 18$ operating in the regimes with separated (Fig. 3a) and overlapping spectra (Fig. 3b). In the latter case, the total width of the spectrum is about one and half that of a regular BWT of the corresponding length (Fig. 4b), while the efficiency is about 70% of that for a regular BWT.

The results of modeling showed that, from the standpoint of expanding the spectrum, a more favorable situation is observed when detuning in the first section is constant and that in the second section varies accord-

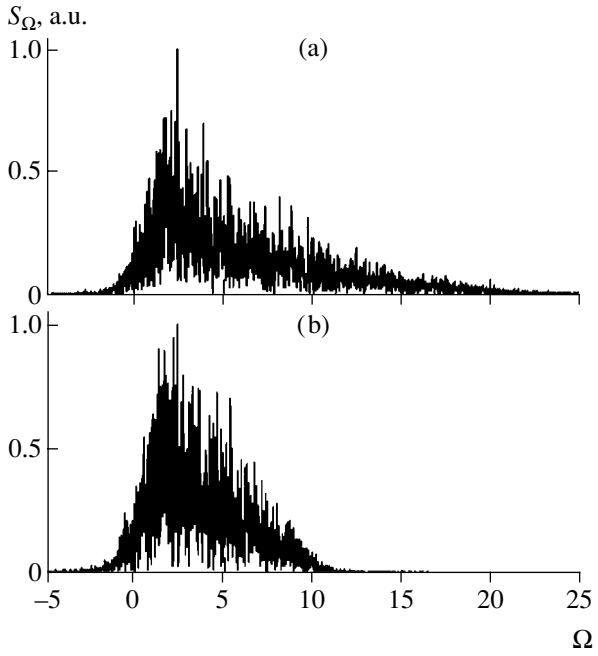

Fig. 4. Generation spectra of (a) a two-section BWT ($L_1 = 6$; $L_2 = 12$) with a linear variation of the synchronism detuning parameter in the second section for $\Delta_1 = 10$ and (b) a regular BWT of the same length.

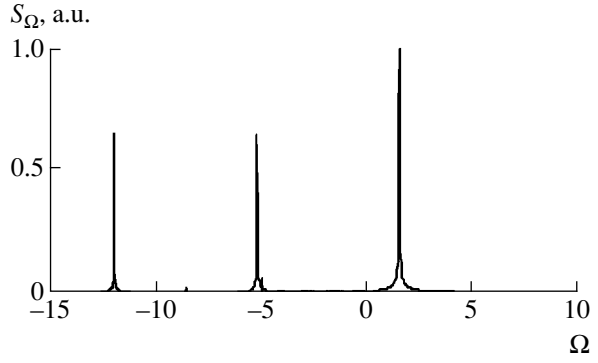

Fig. 5. Generation spectra of a three-section BWT ($L_1 = 2.2$; $L_2 = 2.9$, $L_3 = 2.9$) for $\Delta_1 = -8$, $\Delta_2 = -14$.

ing to a linear law $\Delta(\zeta) = \chi(\zeta - L_1)\Delta_1(\zeta - L_1)/L$. As can be seen from Fig. 4a, this provides for an almost two-fold increase in the width of the spectrum, at an efficiency retained on a level of 95% of that for a regular BWT.

In conclusion, it should be noted that, by increasing the number of sections, it is possible to generate linear spectra comprising a large number of individual frequencies. For example, Fig. 5 shows the generation spectrum of a three-section BWT in which the change in the detuning was preset as $\Delta(\zeta) = \Delta_1\chi(\zeta - L_1) + (\Delta_2 - \Delta_1)\chi(\xi - L_2)$, where $L_{1,2}$ are the coordinates of the boundaries of the first and second sections and $\Delta_{1,2}$ are the changes in the synchronism detuning relative to the first section. In a certain region of parameters, the frequencies of each component can be controlled independently of the other components.

Thus, the results of our analysis show that there are broad possibilities for the synthesis of generation spectra in high-power relativistic BWTs. We are planning to realize these possibilities based on a microsecond accelerator of the Saturn type (Institute of Applied Physics, Nizhni Novgorod) [9].

Acknowledgments. The authors are grateful to N.F. Kovalev and N.I. Zaitsev for stimulating discussions.

This study was supported by the Russian Foundation for Basic Research, project no. 00-02-16412a.

REFERENCES

1. N. S. Ginzburg, N. I. Zaĭtsev, E. V. Ilyakov, *et al.*, Pis'ma Zh. Tekh. Fiz. **24** (20), 66 (1998) [Tech. Phys. Lett. **24**, 816 (1998)].
2. N. S. Ginzburg, N. I. Zaĭtsev, E. V. Ilyakov, *et al.*, Zh. Tekh. Fiz. **71** (11), 73 (2001) [Tech. Phys. **46**, 1420 (2001)].
3. O. Dumbrajs, Int. J. Infrared Millim. Waves **18** (11), 211 (1997).
4. O. Dumbrajs *et al.*, IEEE Trans. Plasma Sci. **PS-27,** 327 (1999).
5. Z. Yang, Z. Liang, B. Zhang, *et al.*, Int. J. Infrared Millim. Waves **20** (1), 83 (1999).
6. N. S. Ginzburg, S. P. Kuznetsov, and T. N. Fedoseeva, Izv. Vyssh. Uchebn. Zaved., Radiofiz. **21**, 1037 (1978).
7. N. F. Kovalev, Élektron. Tekh. Ser. 1: Élektron. SVCh, No. 3, 102 (1978).
8. N. S. Ginzburg and S. P. Kuznetsov, in *Relativistic Microwave Electronics. Problems in Increasing Radiation Power and Frequency* (IPF AN SSSR, Gor'kiĭ, 1981), pp. 101–144.
9. N. I. Zaĭtsev, E. V. Ilyakov, G. S. Korablev, *et al.*, Prib. Tekh. Éksp. **38** (3), 138 (1995).

Translated by P. Pozdeev

Technical Physics Letters, Vol. 29, No. 2, 2003, pp. 168–170. Translated from Pis'ma v Zhurnal Tekhnicheskoĭ Fiziki, Vol. 29, No. 4, 2003, pp. 81–85.

Synthesis and Investigation of Boron-Doped Fullerene and Scandium-Containing Fullerene

G. N. Churilov, A. S. Alikhanyan, M. I. Nikitin, G. A. Glushchenko, N. G. Vnukova, N. V. Bulina, and A. L. Emelina

Kirensky Institute of Physics, Siberian Division, Russian Academy of Sciences, Krasnoyarsk, Russia

e-mail: churilov@iph.krasn.ru

Kurnakov Institute of General and Inorganic Chemistry, Russian Academy of Sciences, Moscow, Russia

Received August 21, 2002

Abstract—We report on the plasmachemical synthesis of fullerene derivatives containing boron and scandium. The synthesis was conducted at atmospheric pressure in a carbon–helium plasma jet generated by an RF arc. © *2003 MAIK "Nauka/Interperiodica".*

Originally, $C_{(60-x)}B_x$ (x = 1–6) molecules were observed by Smalley *et al.* [1] in the gas phase. Muhr *et al.* [2] succeeded in isolating a very small amount of born-containing heterofullerenes from a soot sythesized by the Krätschmer–Haffman method using graphite rods with boron, boron nitride, or boron carbide additives. Boron-containing fragments of the C_nB type (with n = 59, 69, 87, 89, 91, 93, and 95) were identified by mass spectrometry. Scandium-containing endohedral fullerenes were also repeatedly synthesized in negligibly small amounts. For example, Sc_2C_{66} was reported by Wang *et al.* [3]. The product was isolated in an amount of 2 mg from 800 g of a fullerene-containing soot, which corresponds to a total yield of 0.0025 at. %.

We have studied the possibility of obtaining endohedral fullerenes and heterofullerenes using a method realized in a setup described previously [4]. This reactor significantly differs from the conventional Krätschmer setup in that the synthesis is conducted at atmospheric pressure in an arc-generated carbon–helium plasma jet. The plasma jet length reaches about 75 cm at an arc current of 500 A. The temperature varies from 5000 K near the external electrode to 2000 K in the arc tail. Thus, the reactor allows particles of a working substance to stay for a sufficiently long time in the carbon plasma jet, so as to ensure complete atomization of the material. We have conducted the fullerene synthesis with introduction of Sc and B under these conditions.

The initial metallic powder of Sc_2O_3 was charged into a channel in the central electrode [4]. The fullerene-containing soot was treated with benzene in a Soxhlet apparatus, filtered, and evaporation dried. The quantitative content of metal in fullerene was determined using a special setup [5]. According to the data of elemental mass spectrometry and emission spectroscopy, the content of Sc in fullerene was 0.0016 at. %. Figure 1 shows fragments of the emission spectra displaying a Sc peak at 424.683 nm.

The synthesis of boron-containing fullerenes was performed by introducing a B_2O_3 powder into the carbon–helium plasma jet using a special device [6]. The emission spectra of the boron-containing soot and fullerene samples contained a characteristic boron line at 249.773 nm. The relative boron peak intensities in these samples were 183 and 121 units at a background intensity on the order of 40 units. According to the results of mass-spectroscopic measurements, which coincided with the emission spectroscopy data, the rel-

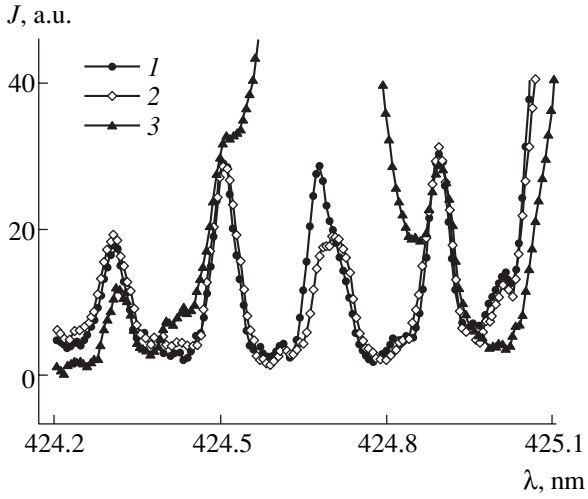

Fig. 1. Emission spectra of samples measured in an argon flow: (*1*) Sc-containing fullerene; (*2*) blank spectrum (discharge without sample introduction); (*3*) Sc-containing fullerene soot.

ative amount of boron-containing fullerenes in the fullerene mixture exceeded 11%.

The benzene extract from a fullerene-containing soot was analyzed on an MI-1201 mass spectrometer modified for high-temperature measurements [7]. The sample was evaporated from a stainless-steel effusion cell and ionized by electron impact at an energy of 60–80 eV.

At temperatures below 515 K, the relatively low vapor pressure of $C_{59}B$ (as compared to that of C_{60}) and insufficiently high resolution of the instrument did not allow us to detect the peaks of ions with $m/e = 718$ and 719 corresponding to $C_{59}B$ molecules. However, the ion current intensity significantly increased with the temperature. This allowed the entrance slit width of the electrometric amplifier to be reduced so as to increase the instrument resolution and obtain a mass spectrum in the region of $m/e = 720$ (Fig. 2). The presence of ions with $m/e = 718$ and 719, together with a ratio of the ion currents characteristic of the boron isotope composition, is evidence for the presence of $C_{59}B$ molecules in the gas phase. This is additionally confirmed by the character of variation of the ratio of $C_{59}B^+$ ion currents with $m/e = 718$–719 and that with $m/e = 720$–723 corresponding to the carbon isotope composition in C_{60} molecules (a contribution of the boron-containing ions with $m/e \geq 720$ is very small). Inside each group, the ion current intensity ratio remains constant during the temperature variation (to within the experimental error), while consistently changing for the ions of various groups. The temperature variation of the relative intensity of $C_{59}B^+$ ($m/e = 719$) and C_{60}^+ ($m/e = 720$) ion currents is presented in the table and can be analytically described by the equation $\log\{I(C_{59}B^+)/I(C_{60}^+)\} = -(1.68 \pm 0.70)/T + (1.85 \pm 0.92)$.

In the region of masses corresponding to C_{70}, the ion peaks were resolved much worse than the peaks of $C_{59}B$ and C_{60}. Nevertheless, even distorted peaks are indicative of the presence of C_{70} and $C_{69}B$ molecules in the gas phase.

At a constant temperature of 790 K, the current of $C_{59}B^+$ ions decreases in intensity with time (relative to that of C_{60}^+) and eventually virtually complete disappears. This can be explained either by a decrease in the activity of $C_{59}B$ in a solid solution of this compound in C_{60} or by diffusion limitations of the $C_{59}B$ flow toward the sample surface. Distinguishing between the two factors requires additional investigation. However, we have

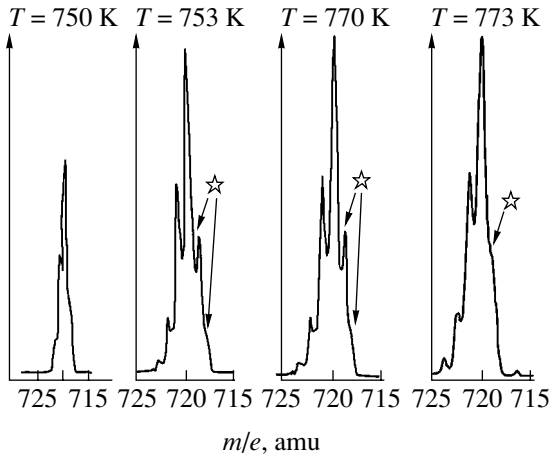

Fig. 2. Temperature variation of a fragment of the mass spectrum of a fullerene extract synthesized upon boron introduction. Stars indicate the peaks corresponding to $C_{59}B$ molecules.

determined the saturated vapor pressure and the parameters of sublimation for $C_{59}B$, assuming equal (unity) activities of $C_{59}B$ and C_{60}. For $a(C_{59}B) = a(C_{60})$, we can approximately take $I(C_{59}B^+)/I(C_{60}^+) \sim p(C_{59}B)/p(C_{60}) = p°(C_{59}B)/p°(C_{60})$. With an allowance for the known temperature dependence of the saturated vapor pressure of C_{60}, $\log\{p°(C_{60})\,[\text{Pa}]\} = -(9.154 \pm 1.50)/T + (8.28 \pm 0.2)$ [7], this yields $\log\{p°(C_{59}B)\,[\text{atm}]\} = -(10838 \pm 166)/T + (5.12 \pm 0.73)$, $\Delta_s H_T^\circ = 208 \pm 18$ kJ/mol, and $\Delta_s S_T^\circ = 98 \pm 18$ J/(mol K).

The greater enthalpy of sublimation obtained for $C_{59}B$ as compared to that for C_{60} can be explained by the fact that the former molecular possesses a dipole moment and, hence, features a stronger intermolecular interaction.

Thus, we have synthesized scandium- and boron-containing fullerenes using a plasmachemical reactor operating at atmospheric pressure. The synthesized fullerenes were studied by emission spectroscopy and mass spectrometry. The results of these measurements confirmed the formation of scandium-containing fullerenes. The content of Sc in the product is very small, amounting to 0.0016 at. %. The formation of boron-doped fullerene was also confirmed. The relative content of this compound in the fullerene mixture exceeds 11%. Thus, the case with boron shows that het-

Temperature variation of the ratio of $C_{59}B^+$ and C_{60}^+ ion currents in the mass spectrum of a boron-doped fullerene

T, K	719	753	769	770	790	773	757
$\log\{I(C_{59}B^+)/I(C_{60}^+)\}$	0.495	0.377	0.238	0.279	0.299	0.418	0.408

erofullerenes can readily form in a carbon–helium plasma jet at atmospheric pressure.

Acknowledgments. This study was supported by the INTAS Foundation (grant no. 01-2399), the Federal Targeted Program "Research and Development in Selected Directions of Science and Technology" (Controlled Synthesis of Fullerenes and Other Atomic Clusters), and the Ministry of Education of the Russian Federation (Scientific Research of Young Scientists, project no. 184; and Scientific-Technological Program, project no. 201.05.01.001).

REFERENCES

1. R. E. Smalley, G. S. Hammond, and V. J. Kuck, ACS Symp. Series **481**, 141 (1992).
2. H.-J. Muhr, R. Nesper, B. Schyder, *et al.*, Chem. Phys. Lett. **249**, 399 (1996).
3. C. Wang, T. Kai, T. Tomiyama, *et al.*, Nature **408**, 426 (2000).
4. G. N. Churilov, Prib. Tekh. Éksp. **43** (1), 5 (2000) [Instrum. Sci. Technol. **43**, 1 (2000)].
5. A. G. Sukovatyi, G. N. Churilov, and S. S. Mal'tseva, Prib. Tekh. Éksp. **41** (5), 137 (1998) [Instrum. Sci. Technol. **41**, 719 (1998)].
6. G. N. Churilov, V. A. Lopatin, P. V. Novikov, and N. G. Vnukova, Prib. Tekh. Éksp. **44** (4), 105 (2001) [Instrum. Sci. Technol. **44**, 519 (2001)].
7. A. L. Emelina, M. I. Nikitin, A. S. Alikhanyan, *et al.*, Zh. Neorg. Khim. **45** (10), 1565 (2000) [Russ. J. Inorg. Chem. **45**, 1565 (2000)].

Translated by P. Pozdeev

Technical Physics Letters, Vol. 29, No. 2, 2003, pp. 171–174. Translated from Pis'ma v Zhurnal Tekhnicheskoĭ Fiziki, Vol. 29, No. 4, 2003, pp. 86–94.

A Comment on the Measurement of Efficiency of the Electron Beam Formation in an Open Discharge

A. R. Sorokin

Institute of Semiconductor Physics, Siberian Division, Russian Academy of Sciences, Novosibirsk, 630090 Russia

e-mail: ars@isp.nsc.ru

Revised manuscript received September 10, 2002

Abstract—Methods used for the measurement of the efficiency of the electron beam formation in an open discharge are critically analyzed. It is shown that a high efficiency determined as the ratio of the beam current to the total current, $\eta = j_e/j$, can serve neither as evidence for one of the open discharge mechanisms nor as a true criterion of the energy efficiency of the beam formation. Under typical open discharge conditions, when electrons in the entire discharge gap occur in the runaway regime, the η value is close to the geometric transparency of the anode grid and is independent of the coefficient of electron emission (γ) from the cathode. It is also demonstrated that recent experiments reported by P.A. Bokhan and D.E. Zakrevsky [Tech. Phys. Lett. **28**, 74 (2002)] do not prove the photoelectron nature of the discharge studied but, on the contrary, confirm once again that the open discharge is not induced by photoelectrons. © *2003 MAIK "Nauka/Interperiodica".*

In the author's opinion, the question concerning the measurement of efficiency referred to in the heading has received much attention in connection with the active discussion about the mechanism of open discharge (OD): the point is whether the OD is maintained due to the cathode photoexcitation from the drift space behind the anode grid [1–4] or it is due to the cathode being bombarded with fast heavy particles [5–8]. The discussion was animated by publication [2], describing experiments in which the photoelectron-maintained (as believed by the authors of [2]) OD showed "an extremely high electron beam generation efficiency: for p_{He} = 8.5–9 Torr and an electron beam current density of j_e = 5–7 mA/cm^2, the efficiency reaches η = 98.3%." Note that the efficiency η was determined in [2] as the ratio of the collector current j_e to the total current j.

Below, the problem concerning the methods used for measuring the efficiency (briefly addressed in [7, 8]) will be considered from the most general standpoint and the experiments reported in [2] will be given an interpretation different from that proposed by the authors. The working gas in all cases is helium.

1. First, consider the case of an OD with a usual anode grid. We will use slightly modified reasoning of [9]. Let equal numbers of ions and electrons ($N_i = N_e$) be generated as a result of the ionization processes in the discharge gap. A fraction k of these electrons, accelerated to a velocity sufficiently high to reach the collector in a field ensuring the "runaway" of electrons [$E/p > (E/p)_{cr}$ = 150 V/(cm Torr)], will join the electron beam together with the electrons produced in the γ-processes on the cathode. For the parameter η, this yields

$$\eta = j_e/j = \mu(kN_i + \gamma N_i)(\gamma N_i + N_i)^{-1} = \mu\xi, \quad (1)$$

where $j = j_e + j_a$, j_a is the anode grid current and μ is the geometric transparency of the grid.

Now let us consider typical pulsed OD regimes for which the potential or field strength distributions in the discharge gap have been measured [3, 10]. Note that the residual field behind the region of the cathode potential fall can exceed the $(E/p)_{cr}$ value by one order of magnitude [3], which implies that all electrons generated within the gap volume can occur in the regime of continuous acceleration. Therefore, the coefficient k can be close to unity and $\eta \approx \mu$, which is usually observed under the optimum OD conditions; it is important to note that η in this case is independent of the γ value. For the simplest discharge featuring weakly distorted field, the current to the grid wires is small and $\eta \approx \xi$ [11].

All the recent attempts at proving the photoelectron nature of the OD reduce to the following algorithm: once the ion- and atom-induced electron emission from the cathode cannot provide for the required level, this role is a priori performed by photoemission (the real contribution of which is difficult to determine). The estimates and calculations either ignored the atom-induced electron emission [12] or determined the value of ξ in Eq. (1) by the formula $\xi = \gamma N_i(\gamma N_i + N_i)^{-1} = \gamma(\gamma + 1)^{-1}$ [4], that is, with neglect of the flux of electrons generated in the gap volume (k = 0) and thus understating the calculated η value (a different, most general approach to solving this problem has been developed, e.g., in [7, 8]). Note also that it is incorrect to compare the parameter η directly to the efficiency of

1063-7850/03/2902-0171$24.00

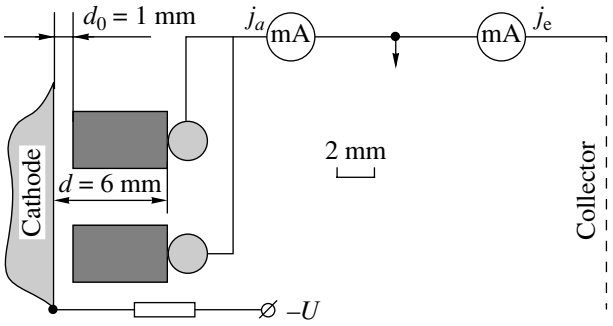

Fig. 1. Schematic diagram of the fragment of a discharge cell used in the experiments reported in [2]: several flat quartz plates supporting molybdenum rods (anode) are arranged near (d_0 = 1 mm) a stainless steel cathode.

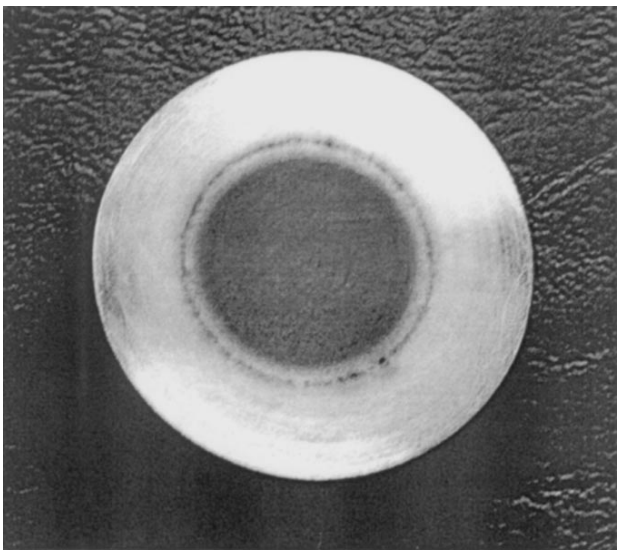

Fig. 2. An autograph on the surface of a duralumin cathode with a diameter of 25 mm, operated in a plane-parallel discharge gap filled with a He : O_2 mixture (100 : 1) at $p \approx$ 1 Torr and $U \approx 20$ kV. The cathode was covered with 3-mm-thick glass plate (spaced by 1 mm from the cathode surface) with a 22-mm-diameter hole. The image displays traces of erosion in the form of a ring with the same diameter (22 mm).

traditional electron guns with anode plasma [13, 14], for which the efficiency is measured with the aid of calorimeters, thus taking into account the beam energy rather than the current. These values would mean the same only if the OD were actually of photoelectron nature.

2. All of what was said above concerning the efficiency measurements fully applies to the experiments [2] with continuous discharge in a device of the type depicted in Fig. 1, which immediately casts doubt on the conclusion [2] that $\eta = 98.3\%$ "can be provided (at an anode voltage of 2.5–3 kV) only by the photoelectron emission mechanism." Indeed, a usual discharge with anode plasma at $U = 2.4$ kV provides for an energy efficiency of 70% [14], but this efficiency (as noted above) cannot be compared to the parameter η. In addition, note that η in the OD can be close to unity ($\eta \approx \xi \approx 1$) is by no means new and was previously demonstrated under the conditions when the current to the grid wires is small, as in the initial low-current stage of a pulsed discharge [15, Fig. 1] or even in the stage of maximum current in the simplest discharge [11].

Moreover, note that, in the discharge gap geometry depicted in Fig. 1, the collector current may contain a contribution due to the direct discharge (including a low-voltage form) passing from the main discharge region immediately to the collector.

Let us turn to comments on the experimental results presented in [2, Fig. 2] (for $p = 8.3$ Torr). When the voltage is small, a discharge initiated in the cavities between quartz plates is not influenced by these cavities. According to the pattern of field lines and electron trajectories, the discharge occupies (as usually [13, 16]) only a small central part of the cathode in the front of each cavity. As the voltage U (and the current) increases, the volume charge begins to distort the field in the interelectrode gap and the cathode area occupied by the discharge tends to grow. This process, together with the growth in γ, is accompanied by a rapid increase in the total current j.

As the voltage U grows further, the increase in current slows down, while the onset of processes on the walls of the cavities, where negative charges (screening the field at the cathode as in the case of a hollow cathode) begin to deposit, can even somewhat decrease the total current j [2, Fig. 2]. The process of plasma displacement from the cavities proceeds [17] and the main part of the applied voltage drops in the near-anode region, from which a discharge takes place immediately to the collector (under constrained conditions, the discharge proceeds via longer pathways [18]). This is favored by effective charging of the surface of quartz plates directly from the cathode (due to edge effects). This is illustrated by the autograph (obtained under somewhat different conditions) in Fig. 2, where the central cathode spot (formed due to the metal oxidation) corresponds to the main discharge region and exhibits no traces of erosion. A denser discharge (with evidence of significant erosion of the cathode surface) charging the edge surface of a hole in a glass plate did not influence overall stability of the discharge. Eventually, the maximum current was limited by a spark discharge at these sites, which was accompanied by a significant erosion of the cathode.

Now it will be demonstrated that the results of experiments reported in [2] lead directly to a conclusion that only a small part of the applied voltage drops in the near-cathode region. As pointed out in [2], "a deep suppression of the ion current to cathode results in that the total current density in the open discharge is lower by more than three orders of magnitude than that in the anomalous discharge ($j_{AD} = 2.5 \times 10^{-12} p^2 U^3$ [19]."

Indeed, according to this formula, the maximum of j = 1.2 mA/cm^2 (observed at U = 640 V [2, Fig. 2]) must correspond to U = 190 V, which is in fact much lower than 640 V. However, the formula must involve the value of a cathode fall U_{cf} [19], rather than the voltage U applied to the gap, as was adopted in [2]. As demonstrated in [19] for a broad range of conditions of the usual OD with a gap width d and a cathode fall length $l_{cf} \le d$, the discharge current in a quasistationary regime corresponds to anomalous discharge current j_{AD}. In the case under consideration, according to [20], for j = 1.2 mA/cm^2 we obtain l_{cf} = 0.75 mm (which is smaller than d_0 = 1 mm in Fig. 1). Therefore, the discharge current developed in the near-cathode region of length $\sim d_0$ must correspond to a cathode fall of U_{cf} = 190 V. The remaining part of the applied voltage (ΔU = 450 V) drops across the near-anode region from which the current to collector is transferred both by the electron beam and by direct discharge. The second buildup of the current, observed when the voltage increases above $U >$ 2–3 kV (see [2, Fig. 3]), can be a result of the onset of a denser plasma penetrating into the cavities [17, 18]. Note that, in a high-voltage discharge with a hollow cathode, the plasma potential in a cathode cavity relative to the cathode amounts to 100–400 V [18]. The main part of the applied voltage (i.e., that forming the electron beam) drops in front of the cathode cavity [18].

Not let us turn to the parameter η which exhibits a sharp drop at $U <$ 850 V (see [2, Fig. 2]). This result is not surprising, since the fastest electrons in these experiments can reach the collector if the penetration depth $l_N = 0.02p^{-1}U$ [Torr V] [21] is greater than the distance between cathode and collector (2.8 cm), that is, for $U >$ 1.2 kV. However, a significant collector current in [2] was observed immediately under the near-threshold discharge initiation conditions (U_{th} = 440 V) for which l_N = 1 cm, which is also indicative of a direct discharge to collector developed from a near-anode region or from the region of negative space charge carried out by the electron beam. Here, it should be also taken into account that the average field strength in the gap (d = 6 mm) reaches a critical level at $U_{cr} = (E/p)_{cr}pd$ = 750 V.

Thus, in measuring the electron beam current, we should take into account the possibility that the collector detects a direct discharge current in addition to the beam current. Upon the charge separation in the field at the cathode surface, after the γ-processes or the ionization events within the discharge gap, the motion of charges (electrons and ions) toward an external current source will be registered as a collector current for all electrons striking the collector, even if these electrons have acquired a negligibly small velocity on their pathway.

Finally, let us discuss (albeit not for the first time) the question originally formulated in [5]: why are high voltages necessary for the photoelectron discharge? As is known, the maximum fraction of the discharge energy spent for excitation of the resonance He line (from which a maximum photoemission effect has to be expected [22]) corresponds to $(E/p)_{opt}$ = 65 V/(cm Torr) [23]. Under the conditions studied (d = 6 mm, p = 8.3 Torr), the optimum voltage is U_{opt} = 320 V < U_{th} = 440 V. For U_{opt}, or close to this, the photoelectron discharge (believed to be initiated and maintained due to photoelectron emission [24]) must increase up to a level [6] determined by the "3/2 power" law: $j = 2.34 \times 10^{-6}U^{3/2}d^{-2}$. In particular, for $U = U_{th}$ = 2 kV, this yields 60 mA/cm^2 or 0.6 A/cm^2, which is two orders of magnitude higher than the level attained in [2]. Moreover, as U increases far above U_{opt}, the medium becomes more and more transparent for the electron beam (for U = 2 kV, I_N = 5 cm). Therefore, the efficiency of photoexcitation and, hence, the photoelectron-induced discharge current must drop rather than grow (as in the experiment). From the standpoint of the traditional notion about the glow discharge, the increase in the current with the voltage U is readily explained by the total emission from the cathode increasing due to a growth in the energy of ions (as well as of atoms) and their flux from the near-anode plasma [7, 8, 13].

3. The qualitative pattern of the experiments reported in [2], as outlined above, may differ in some details from the true situation. In order to refine this pattern, one must at least know the true distribution of the potential (or field strength) in the discharge gap. Nevertheless, the most general points of the analysis (based on the experimental data only) will always be retained. These are as follows. Under the optimum OD conditions, the parameter η is independent of γ, which follows from the results of measurements of the field strength in the gap [3]. High values of the working voltages in the OD studied are very far from the optimum conditions for the effective photoemission from the cathode [22, 23]. The small total current observed in the experiments reported in [2] and, on the contrary, the relatively large collector currents (especially at low voltages, when the electron beam does not reach the collector), are indicative of the voltage drop being concentrated mainly in the near-anode region. A direct discharge from this region to the collector was mistaken in [2] as the electron beam current.

Finally, a small value of the voltage drop in the d_0 region at the cathode makes a high energy efficiency unattainable for any value of the photoemission coefficient. Low fields can feature avalanche development (up to five electrons in each at 190 V [23]) and an insignificant atom-induced electron emission. The small current observed in the experiments is evidence of a weak feedback and, hence, of the absence of any significant contribution due to photoemission.

Thus, it was demonstrated that (i) a high efficiency of the electron beam formation determined as the ratio of the beam current to the total current can serve neither as evidence for one of the open discharge mechanisms nor as a true criterion of the energy efficiency of the

electron beam formation. The results of experiments reported in [2] do not prove the photoelectron nature of the discharge studied but, on the contrary, confirm once again the earlier conclusion of the author of this letter that the open discharge is not of a photoelectron nature.

Comments on the calculations of the emission coefficient γ [4, 25] and on the role of compensation currents in the OD [4] are planned as separate publications.

Acknowledgments. The author is grateful to S.G. Rautian and his Seminar and to A.M. Shalagin and D.A. Shapiro for support of this study.

REFERENCES

1. A. P. Bokhan and P. A. Bokhan, Pis'ma Zh. Tekh. Fiz. **27** (6), 7 (2001) [Tech. Phys. Lett. **27**, 220 (2001)].
2. A. P. Bokhan and D. E. Zakrevsky, Pis'ma Zh. Tekh. Fiz. **28** (2), 74 (2002) [Tech. Phys. Lett. **28**, 73 (2002)].
3. G. V. Kolbychev and I. V. Ptashnik, Opt. Atmos. Okeana **12** (11), 1070 (1999).
4. G. V. Kolbychev, Opt. Atmos. Okeana **14** (11), 1056 (2001).
5. A. R. Sorokin, Pis'ma Zh. Tekh. Fiz. **21** (20), 37 (1995) [Tech. Phys. Lett. **21**, 832 (1995)].
6. A. R. Sorokin, Zh. Tekh. Fiz. **68** (3), 33 (1998) [Tech. Phys. **43**, 296 (1998)].
7. A. R. Sorokin, Opt. Atmos. Okeana **14** (11), 1062 (2001).
8. A. R. Sorokin, Pis'ma Zh. Tekh. Fiz. **28** (9), 14 (2002) [Tech. Phys. Lett. **28**, 361 (2002)].
9. G. V. Kolbychev and E. A. Samyshkin, Zh. Tekh. Fiz. **51** (10), 2032 (1981) [Sov. Phys. Tech. Phys. **26**, 1185 (1981)].
10. V. P. Demkin, B. V. Korolev, and S. V. Mel'nichuk, Fiz. Plazmy **21**, 81 (1995) [Plasma Phys. Rep. **21**, 76 (1995)].
11. A. R. Sorokin, Pis'ma Zh. Tekh. Fiz. **22** (13), 17 (1996) [Tech. Phys. Lett. **22**, 526 (1996)].
12. S. V. Arlantsev, B. L. Borovich, V. V. Buchanov, *et al.*, J. Russ. Laser Res. **16** (2), 99 (1995).
13. M. A. Zav'yalov, Yu. E. Kreĭndel', A. A. Novikov, and L. P. Shanturin, *Plasma Processes in Electron Guns* (Énergoatomizdat, Moscow, 1989).
14. Z. Yu, J. J. Rocca, and G. J. Collins, J. Appl. Phys. **54** (1), 131 (1983).
15. G. V. Kolbychev, Opt. Atmos. Okeana **6** (6), 635 (1993).
16. I. V. Vagner, É. I. Bolgov, *et al.*, Avtom. Svarka, No. 12, 27 (1972).
17. B. I. Moskalev, *Hollow Cathode Discharge* (Énergiya, Moscow, 1969).
18. Yu. E. Kreĭndel', *Plasma Electron Sources* (Atomizdat, Moscow, 1977).
19. K. A. Klimenko and Yu. D. Korolev, Zh. Tekh. Fiz. **60** (9), 138 (1990) [Sov. Phys. Tech. Phys. **35**, 1084 (1990)].
20. Yu. P. Raĭzer, *Gas Discharge Physics* (Nauka, Moscow, 1987).
21. A. A. Kudryavtsev and L. D. Tsendin, Pis'ma Zh. Tekh. Fiz. **27** (7), 46 (2001) [Tech. Phys. Lett. **27**, 284 (2001)].
22. B. N. Klyarfel'd and B. I. Moskalev, Zh. Tekh. Fiz. **39** (6), 1066 (1969) [Sov. Phys. Tech. Phys. **14**, 800 (1969)].
23. V. Yu. Baranov, V. M. Borisov, F. I. Vysikaĭlo, *et al.*, *Energy Balance and Excitation Rates for Individual Levels in F_2:Xe:He Mixtures* (Inst. At. Énergii, Moscow, 1979), Preprint No. 3080.
24. G. V. Kolbychev, P. D. Kolbycheva, and I. V. Ptashnik, Zh. Tekh. Fiz. **66** (2), 59 (1996) [Tech. Phys. **41**, 144 (1996)].
25. A. R. Sorokin, Pis'ma Zh. Tekh. Fiz. **26** (24), 89 (2000) [Tech. Phys. Lett. **26**, 1114 (2000)].

Translated by P. Pozdeev

Technical Physics Letters, Vol. 29, No. 2, 2003, pp. 85–87. Translated from Pis'ma v Zhurnal Tekhnicheskoĭ Fiziki, Vol. 29, No. 3, 2003, pp. 1–7.

Variation of the Yield Stress and Latent Strain Energy in the Course of Plastic Deformation of a Neutron-Irradiated Chromium–Nickel Steel

O. P. Maksimkin and M. N. Gusev

Institute of Nuclear Physics, State Nuclear Center of the Republic of Kazakhstan, Almaty, Kazakhstan

Received July 2, 2002

Abstract—The laws of variation of the flow stress (σ) and latent strain energy (E_s) in the course of plastic deformation have been studied in the samples of a titanium-doped chromium–nickel steel (12Kh18N10T grade) before and after neutron irradiation to a dose of 5×10^{22} m^{-2} (neutron energy $E > 0.1$ MeV). The E_s versus σ curve can be divided into several characteristic regions, the first of which is described by a relation of the type $E_s \sim E_0 + k\sigma^2$ (E_0 and k being certain coefficients). It is established that neutron irradiation shifts the E_s versus σ curve toward smaller latent energies. © *2003 MAIK "Nauka/Interperiodica".*

Introduction. A defect structure, which is formed and evolved in the course of irradiation and/or plastic deformation of metal crystals, is the "carrier" of a latent strain energy E_s. Behavior of the E_s value is related to changes in many important properties (physical, mechanical, chemical) of metals and alloys, as well to the features of structural and phase transformations taking place in these materials [1]. In particular, it was suggested that the ability of a material to accumulate and dissipate mechanical energy supplied from outside may determine the laws and degree of strain hardening [2]. On the other hand, a defect structure influences the level of internal stresses in a crystal, and, hence, E_s at any instant of plastic deformation must be related to the flow stress σ. This relation has been considered, for example, in [3], where it is shown that $E_s \sim \sigma^2$. However, the problem is still far from being completely solved for real materials (especially, for polycrystals) containing radiation-induced defects.

Experimental. We have studied the process of energy accumulation and dissipation in the course of plastic deformation of unirradiated and irradiated metals and alloys. The experiments were performed in a specially designed setup combining a differential Calvet calorimeter with a microtesting machine [4], which made it possible to measure simultaneously a stress–strain diagram (plotted as the loading force F versus elongation Δl) and a DSC thermogram (plotted as the heat evolution rate dQ/dt versus time t). Previously, this setup was used to study the energy accumulation and dissipation in the course of tensile tests of iron and niobium [5] and a titanium-doped chromium–nickel austenite steel (12Kh18N10T grade) [6].

In this paper, we report on the results of investigation of samples of 12Kh18N10T steel with dimensions $10 \times 3.5 \times 0.3$ mm prepared by austenization for 30 min at 1323 K in vacuum, followed by cooling in water. The samples were tested in the initial (unirradiated) state and after neutron irradiation to a total fluence of 5×10^{22} m^{-2} (neutron energy $E > 0.1$ MeV; the sample temperature during irradiation did not exceed 330 K). Both unirradiated and neutron-irradiated samples were uniaxially stretched at a rate of 8.3×10^{-4} s^{-1} inside a microcalorimeter cell in the temperature range from 293 to 473 K. The simultaneously measured stress–strain diagrams and DSC thermograms were used to determine the deformation work $A = \int F\,dl$, the dissipated heat $Q = \int (dQ/dt)dt$, and the total latent energy $E_s = A - Q$.

Upon treating the DSC thermograms as described in detail elsewhere [7], we calculated the energy characteristic A, Q, and E_s as functions of the applied stress σ (the error of determining E_s did not exceed 15%). These experimental data were used to plot the E_s versus σ_1 plots, where σ_1 is the true stress defined as $\sigma_1 = F_1/S_1$. The true stress was determined using an empirical relation established previously between the current cross section S_i and the corresponding relative elongation δ_i,

$$S_i = S_0 - A\delta_i - B\exp\left(\frac{\delta_0 - \delta_i}{\delta}\right),$$

where δ_0 and δ are the uniform and total deformation, respectively; S_0 is the initial sample cross section; and A and B are constant coefficients. Deviation of the value of σ_1, calculated using this formula, from the stress measured in a control experiment (where the current sample width and thickness were measured directly) did not exceed 5% in the uniform deformation range

1063-7850/03/2902-0085$24.00

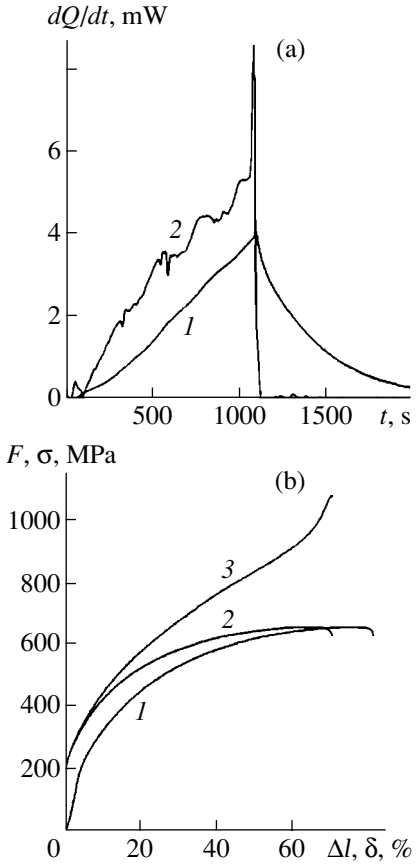

Fig. 1. Typical experimental and recalculated curves for unirradiated 12Kh18N10T stainless steel samples tensile tested at 293 K: (a) primary (*1*) and restored (*2*) DSC thermograms; (b) stress–strain diagrams plotted as (*1*) load F versus total elongation Δl, (*2*) effective stress σ versus residual strain δ, and (*3*) true stress σ_1 versus residual strain δ.

(below, we omit the subscript and denote the true stress by σ).

Results and discussion. Figure 1 shows a primary DSC thermogram (distorted because of a delay in the calorimeter response) measured in the course of the calorimetric run, the corresponding true thermogram (restored as described in [7]), the experimental F versus Δl curve, and the stress–strain diagram (σ versus δ) calculated with allowance for a change in the sample cross section. The values of strength and plasticity parameters, as well as the energy characteristics of strain determined using the experimental results for 12Kh18N10T steel, are presented in the table. As can be seen from these data, the neutron-irradiated steel samples accumulate a significantly lower energy and dissipate a greater energy than do the initial (unirradiated) samples. This behavior is in agreement with our previous results [6]. As can also be seen from Fig. 1, the true flow stress increases until the sample exhibits fracture, which is reflected by a high peak of heat evolution in the DSC thermogram. As the degree of sample deformation increases, the rate of latent energy accumulation decreases; after local strain development, almost no energy is accumulated in the material.

Figure 2 shows the plots of specific latent energy E_s versus flow stress σ. As can be seen, the curves corresponding to the initial and irradiated samples are similar, but the latter curve is shifted toward lower E_s values (downward the energy axis). An analysis of the $E_s = f(\sigma)$ function showed that the uniform deformation range can be divided into several characteristic regions, the first of which (corresponding to small deformations and stresses) is described by a relation of the type

$$E_s = E_0 + k\sigma^2, \quad (1)$$

where E_0 and k are coefficients which can be assigned a certain physical meaning.

It is most probable that the absolute value of E_0 characterizes the internal energy of a polycrystal, which is related to a structural state of the initial (undeformed) material, the development of grain boundaries, and the morphology and concentration of defects in the crystal lattice. The numerical value of E_0 can be determined using the experimental curve of $E_s = f(\sigma)$, through extrapolation of the approximating parabola to intersection with the ordinate axis ($\sigma = 0$). It was found (see table) that unirradiated steel tensile tested at various temperatures in the interval from 293 to 473 K is char-

Mechanical and energy characteristics of 12Kh18N10T steel before and after neutron irradiation (total fluence, 5×10^{22} m^{-2})

Sample state and test temperature, K		$\sigma_{0.2}$, MPa	σ_u, MPa	δ_0, %	δ, %	A, MJ/m^3	Q, MJ/m^3	E_s, MJ/m^3	$k \times 10^{-4}$	$\lvert E_0 \rvert$, MJ/m^3
Initial	298	18	660	65	70	410	310	100	1.5	6
Irradiated		440	720	53	61	405	332	73	1.4	25
Initial	423	140	440	34	37	140	90	50	1.8	5
Irradiated		330	530	37	42	200	152	48	1.8	18
Initial	473	140	470	33	36	142	96	46	2.0	5
Irradiated		320	500	29	34	162	119	43	2.0	16

Note: the values of k refer to region 1 in Fig. 2.

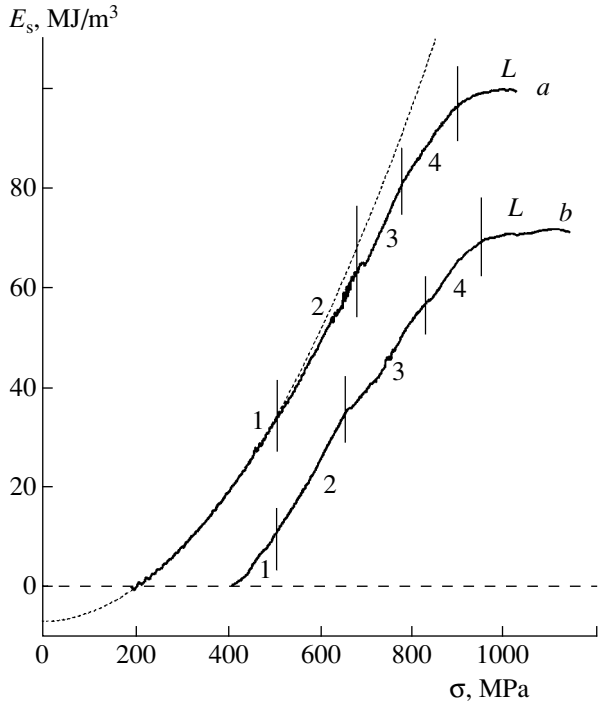

Fig. 2. Plots of the latent strain energy E_s versus flow stress σ for (*a*) initial and (*b*) neutron-irradiated 12Kh18N10T steel tensile tested at 293 K. Dashed curve represents the approximating parabola for region 1; region *L* corresponds to the state of local strain development.

acterized by very close E_0 values. This fact may be evidence of the structural sensitivity of the E_0 value. At the same time, the E_0 values of irradiated samples decrease with increasing temperature. This is probably related to partial annealing of the radiation defects in the course of heating the sample up to the temperature of tensile testing. Note that a quadratic dependence of the stored energy on the flow stress in the early stage of deformation was also observed in our experiments with pure copper (both unirradiated and neutron-irradiated to a dose of 2×10^{24} m^{-2}) [10].

The curves of $E_s = f(\sigma)$ for both initial and neutron-irradiated samples of 12Kh18N10T steel (Fig. 2) reveal four characteristic regions in the range of stresses below ultimate strength. This does not contradict the existing notions about plastic flow stages, whereby various dislocation structures sequentially form and dominate in the strained material [1]. As can be seen from Fig. 2, the E_s versus σ curve for the irradiated steel is shifted by ~20 MJ/m^3 toward lower energies, which is probably related to an additional latent energy related to the radiation-induced defects.

Another noteworthy experimental fact is the presence of certain features in the temperature variation of parameter *k* in the first region separated on the $E_s = f(\sigma)$ curve (see table). The higher the temperature of testing, the greater the *k* value. The temperature sensitivity of *k* can be related to an increase in the stacking fault energy with increasing temperature known in stainless steels [8, 9].

Conclusion. We have experimentally studied the relationship between the latent strain energy E_s and the flow stress σ of 12Kh18N10T stainless steel samples continuously strained inside a calorimetric cell after austenization and neutron irradiation to a total fluence of 5×10^{22} m^{-2}. It is established that the $E_s(\sigma)$ curve can be divided into several characteristic regions, the first of which is described by a relation of the type $E_s \sim k\sigma^2$.

REFERENCES

1. M. A. Bol'shanina and V. E. Panin, Latent Strain Energy, in *Investigations in Solid State Physics* (Akademizdat, Moscow, 1957).
2. V. V. Rybin, *Large Plastic Deformations and Fracture of Metals* (Metallurgiya, Moscow, 1986).
3. J. Friedel, *Dislocations* (Oxford, 1964; Mir, Moscow, 1967).
4. O. P. Maksimkin, Preprint 94-02 (Physicotechnical Institute, Natl. Acad. Sci., Kazakhstan, Almaty, 1994).
5. O. P. Maksimkin and M. N. Gusev, Pis'ma Zh. Tekh. Fiz. **27** (24), 85 (2001) [Tech. Phys. Lett. **27**, 1065 (2001)].
6. Sh. Sh. Ibragimov, O. P. Maksimkin, and A. V. Bolotov, At. Energ. **66** (6), 430 (1989).
7. I. V. Astaf'ev and O. P. Maksimkin, Zavod. Lab., No. 1, 44 (1994).
8. Yu. N. Petrov, *Defects and Diffusionless Transformations in Steel* (Naukova Dumka, Kiev, 1972), p. 101.
9. O. P. Maksimkin and M. N. Gusev, in *Effects of Radiation on Materials: Proceedings of the 20th International Symposium (ASTM Spec. Tech. Publ. 1405)* (ASTM, 2001), pp. 813–824.

Translated by P. Pozdeev

Technical Physics Letters, Vol. 29, No. 2, 2003, pp. 88–89. Translated from Pis'ma v Zhurnal Tekhnicheskoĭ Fiziki, Vol. 29, No. 3, 2003, pp. 8–12.

Determining Defect Complex Formation Parameters from Isochronous Annealing Curves

S. V. Bulyarskiĭ and V. V. Svetukhin

Ul'yanovsk State University, Ul'yanovsk, Russia

e-mail: slava@sv.uven.ru

Received August 6, 2002

Abstract—Parameters of the defect complex formation in semiconductors can be determined from the experimental curves of isochronous annealing. By processing data on the annealing of Au–Fe complexes in silicon, estimates are obtained for the complex formation energy (0.8 eV) and the activation energy of iron diffusion (0.9 eV). © *2003 MAIK "Nauka/Interperiodica".*

The process of defect complex formation may cause degradation of semiconductor devices, but it can also be used as a means of controlling the material properties. For these reasons, investigation of the complex formation process and determination of the nature of complexes are important tasks for research in semiconductors.

It is rather a common situation when a complex (K) is formed by two defects (A and B). The process corresponds to the scheme A + B $\rightleftharpoons$ K and is described by a system of kinetic equations

$$\begin{cases} \dot{N}_\mathrm{K} = -gN_\mathrm{K} + cN_\mathrm{A}N_\mathrm{B}, \\ \dot{N}_\mathrm{A} = gN_\mathrm{K} - cN_\mathrm{A}N_\mathrm{B}, \\ \dot{N}_\mathrm{B} = gN_\mathrm{K} - cN_\mathrm{A}N_\mathrm{B}, \end{cases} \tag{1}$$

where g is the complex decay rate constant, c is the complex formation rate constant, and N_K, N_A, and N_B are the concentrations of complexes K and component species of the A and B types, respectively.

Solving the system of Eqs. (1) with the initial conditions

$$N_\mathrm{A}(t=0) = N_\mathrm{A}^0, \quad N_\mathrm{B}(t=0) = N_\mathrm{B}^0, \quad N_\mathrm{K}(t=0) = N_\mathrm{K}^0 \tag{2}$$

yields the concentration of complexes as a function of the time [1]

$$N_\mathrm{K}(t) = N_\mathrm{K}^\mathrm{eq} + \frac{1}{\frac{c}{\lambda}(1-\exp\{\lambda t\}) + \frac{1}{N_\mathrm{K}^0 - N_\mathrm{K}^\mathrm{eq}}\exp\{\lambda t\}}, \tag{3}$$

where $\lambda = g + c[N_\mathrm{A}^0 + N_\mathrm{B}^0 + 2(N_\mathrm{K}^0 - N_\mathrm{K}^\mathrm{eq})]$. Note that the variables in Eqs. (1) also obey the condition of conservation of the total number of species A and B:

$$\begin{aligned} N_\mathrm{A}^\mathrm{tot} &= N_\mathrm{A}^0 + N_\mathrm{K}^0 = N_\mathrm{A}(t) + N_\mathrm{K}(t), \\ N_\mathrm{B}^\mathrm{tot} &= N_\mathrm{B}^0 + N_\mathrm{K}^0 = N_\mathrm{B}(t) + N_\mathrm{K}(t). \end{aligned} \tag{4}$$

The concentration of complexes increases with the time to approach the equilibrium value N_K^eq determined by the formulas

$$\begin{aligned} N_\mathrm{K}^\mathrm{eq} &= \frac{1}{2}\left(\frac{g}{c} + N_\mathrm{A}^\mathrm{tot} + N_\mathrm{B}^\mathrm{tot} - \sqrt{D}\right), \\ D &= \left(\frac{g}{c} + N_\mathrm{A}^\mathrm{tot} + N_\mathrm{B}^\mathrm{tot}\right)^2 - 4N_\mathrm{A}^\mathrm{tot}N_\mathrm{B}^\mathrm{tot}. \end{aligned} \tag{5}$$

The equilibrium solution (5) must coincide with the result of thermal cycling [1] described by the equation

$$\begin{aligned} N_\mathrm{K}^\mathrm{eq} &= Z\frac{N_\mathrm{A}^\mathrm{eq}N_\mathrm{B}^\mathrm{eq}}{N}\exp\left\{-\frac{G_\mathrm{K}}{kT}\right\} \\ &= Z\frac{(N_\mathrm{A}^\mathrm{tot} - N_\mathrm{K}^\mathrm{eq})(N_\mathrm{B}^\mathrm{tot} - N_\mathrm{K}^\mathrm{eq})}{N}\exp\left\{-\frac{G_\mathrm{K}}{kT}\right\}, \end{aligned} \tag{6}$$

where N is the concentration of lattice cites occupied by the defects, Z is the number of equivalent orientations of the complex, G_K is the Gibbs free energy of the complex formation. The latter quantity is related to the enthalpy (H_K) and entropy (S_K) of defect formation as $G_\mathrm{K} = H_\mathrm{K} - S_\mathrm{K}T$.

A solution of Eq. (6) coincides with the equilibrium defect concentration (5), provided that

$$\frac{c}{g} = \frac{Z}{N}\exp\left\{-\frac{G_\mathrm{K}}{kT}\right\}. \tag{7}$$

This useful formula established a relation between the kinetic coefficients determining the formation and

decay of the complexes studied. Condition (7) is satisfied, for example, with the kinetic coefficients in the following form:

$$c(T) = A_c \exp\left(-\frac{E_c}{kT}\right), \quad (8)$$

$$g(T) = A_g \exp\left(-\frac{E_g}{kT}\right), \quad (9)$$

where E_c and E_g are the activation energies for the complex formation and decay, respectively. In the case when the complex formation process is controlled by diffusion, the coefficient c is related to the coefficients of diffusion of the components: $c = 4\pi R_0(D_A + D_B)$, where R_0 is the effective interaction radius. Under these conditions, E_c in expression (8) coincides with the activation energy for the component possessing maximum mobility.

In practice, the process of complex formation can be conveniently studied using the curves of isochronous annealing representing the concentration of complexes as a function of the annealing temperature at a fixed duration of the treatment. An expression describing the isochronous annealing curve can be obtained from formulas (3) and (5), by fixing the time t and considering N_K as the function of the temperature.

Assuming that the initial concentration of one component is much greater than that of the other, expressions (3) and (5) can be simplified to

$$N_K(T) = N_K^{eq}(T) + (N_K^0 - N_K^{eq}(T)) \times \exp\left(-C\exp\left(-\frac{E_c}{kT}\right)\right), \quad (10)$$

$$N_K^{eq}(T) = \frac{A}{1 + B\exp\left(-\frac{H_k}{kT}\right)}, \quad (11)$$

where A, B, and C are constant coefficients.

An analysis of Eqs. (7) and (8) shows that the isochronous annealing curve, as reflecting the complex formation process, has a dome shape limited by decay of the complexes in the high-temperature region and by diffusion of the most mobile component in the low-temperature region. In the high-temperature region, the concentration of complexes coincides with the equilibrium value. Using the approximation $N_K^{eq} \cong A/B\exp(H_K/kT)$ and describing the high-temperature "tail" of the isochronous annealing curve by formula (10), it is possible to determine the enthalpy (free energy) of the complex formation H_K. Then, expression (11) describing the high-temperature part of the isochronous annealing curve in more detail yields the coefficients A and B. Upon substituting the values of A, B, and H_K determined in this way into formulas (7) and (8), we can evaluate the activation energy E_c of diffusion of the most mobile component of the complex, which is calculated as the slope of the plot of

$$\ln\left(\ln\left(\frac{N_K^0 - N_K^{eq}(T)}{N_K(T) - N_K^{eq}(T)}\right)\right) \text{ versus } 1/kT.$$

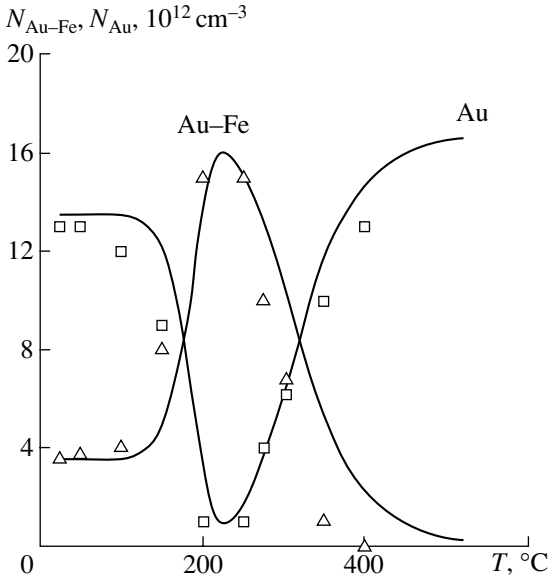

Isochronous annealing of Au–Fe complexes in silicon: solid curves show the concentrations of defect complexes ($N_{Au–Fe}$) and gold atoms (N_{Au}) calculated using formulas (10) and (11); symbols represent the corresponding experimental data [2].

An example of the curve of isochronous annealing of Au–Fe complexes in silicon is presented in the figure together with the results of data processing according to the proposed method. The curve describing variation of the Au–Fe complexes is supplemented by the atomic concentration profile of gold. The treatment of these data gave the enthalpy of Au–Fe complex formation ($H_K \approx -0.8$ eV) and the diffusion activation energy for one of the components ($E_c \approx 0.9$ eV). The latter value coincides with the known activation energy for iron diffusion in silicon.

REFERENCES

1. V. V. Svetukhin and S. V. Bulyarskiĭ, Izv. Ross. Akad. Nauk, Neorg. Mater. **33**, 246 (1997).
2. V. S. Vavilov, V. F. Kiselev, and B. N. Mukashev, *Defects in the Bulk and on the Surface of Silicon* (Nauka, Moscow, 1990).

Translated by P. Pozdeev

Technical Physics Letters, Vol. 29, No. 2, 2003, pp. 90–91. Translated from Pis'ma v Zhurnal Tekhnicheskoĭ Fiziki, Vol. 29, No. 3, 2003, pp. 13–17.

Estimating Substrate Temperature from the Character of the Field-Ion Image of an Adsorbed Molecule

S. V. Zaĭtsev

Institute of Theoretical and Experimental Physics, State Scientific Center of the Russian Federation, Moscow, Russia

e-mail: Sergey.Zaitsev@itep.ru

Received July 2, 2002

Abstract—Separate molecules possessing high dipole moments (water, naphthalene) were deposited from the gas phase onto a conducting sample under the action of an inhomogeneous electric field perpendicular to the substrate surface. It was established that the character of the image of adsorbed molecules observed with a field-ion microscope depends on the substrate temperature and the electric field strength. Using this phenomenon, it is possible to estimate the temperature of adsorbed molecules (and of the substrate) by examining their images or to solve the reverse problem of identifying molecules adsorbed at the known substrate temperature and electric field strength. It is suggested to explain the observed effects by considering an adsorbed molecule as a gyroscope exhibiting nutation. The unique local character of this method makes it a promising tool for nanotechnology and for the investigation of fine thermal effects on solid surfaces. *© 2003 MAIK "Nauka/Interperiodica".*

Miniaturization is one of the most important trends in advanced technologies. It can be expected that the development of nanotechnology will make possible the solution of many global technical problems. The progress in this field stipulates, in particular, the development of more and more local techniques for temperature measurements. For example, researchers in Japan suggested using a gallium-filled carbon nanotube as a nanothermometer [1]. This device was completely synthesized in a single technological cycle. The gallium column, moving inside the carbon nanotube in response to the temperature variations in the interval from 50 to 500°C, was observed in a scanning tunneling microscope. The length of this thermometer was about 10 μm and the diameter was as small as 75 nm.

Below, it is demonstrated that the dimensions of a nanothermometer can be significantly decreased by using a single molecule as a temperature probe. In addition, this will decrease disturbances of the temperature field of the nanoobject being studied, which are unavoidably caused by any probe. The smaller the number of elements in a subsystem studied, the greater the possible relative fluctuations. For this reason, it is not possible to judge the temperature of a gas by observing a single free molecule. In contrast, each molecule in a solid is confined in the crystal lattice and, hence, is much more strongly bound to the system and involved in a high-rate energy exchange with the surrounding molecules. Therefore, "time-averaged" observations of a single molecule in this case allow the whole sample temperature to be determined. Unfortunately, monitoring the amplitude and frequency of oscillations of a single molecule inside a solid is still beyond our possibilities.

However, molecules adsorbed on a solid surface occur under special conditions and possess rotational degrees of freedom in addition to the vibrational ones. On the one hand, this allows an adsorbed molecule to effectively exchange energy with the substrate; on the other hand, this renders the molecule observable and allows us to estimate the amplitude and frequency of the molecular oscillations. In this study, such estimates were obtained by using field-ion microscopy techniques [2].

The experiments were performed using samples in the form of microscopic points with an apical diameter ranging from 50 to 1000 nm. The points were made of tungsten, molybdenum, or stainless steel by the method described elsewhere [3]. The vacuum chamber of a field-ion microscope was filled with helium to a pressure of 10^{-3} Pa. Then, a trace amount of molecules possessing a relatively large dipole moment (e.g., water or naphthalene) was admitted into the chamber and a gradually increasing positive potential was applied to the metal point. The molecules with a large dipole moment, occurring in a strongly inhomogeneous electric field in the vicinity of the metal point, were effectively attracted to the metal surface. When such a molecule is adsorbed on the surface, the local field strength at the free dangling end of the molecule is stronger than the average field strength on the metal surface. As a result, atoms of the imaging gas (helium) are ionized in the region of stronger field, after which the positive helium ions move to a grounded screen and form an image of the adsorbed molecule. An assembly of microchannel plates (ion–electron converter multipliers) mounted in front of the screen enhanced the image brightness by a factor of 10^8.

1063-7850/03/2902-0090$24.00

Typically, a molecule is imaged by a simple bright spot on the screen. However, when the electric potential applied to the point is smoothly adjusted close to a minimum level necessary to hold a molecule at the metal surface, the image becomes more complicated. Figure 1 shows a field-ion image of a water molecule adsorbed on a microscopic point at room temperature. If the potential is fixed and the sample is cooled (by admitting coolant into a special vessel in thermal contact with the point holder) from room temperature to the liquid nitrogen temperature, the image exhibits stepwise variation by passing via a sequence of stable states. Unfortunately, the exact temperatures at which these transitions take place are still not determined, because the temperature of the point tip established in the course of these transient processes is unknown. However, a comparison of Fig. 1 (room temperature) and Fig. 2 (liquid nitrogen temperature) reveals clear differences between the two images. In particular, a characteristic sign is the presence or absence of a bright spot at the center of the image.

The simplest explanation of the phenomenon observed can probably be provided by considering an adsorbed molecule as a gyroscope with one fixed point. When the frequencies of rotations about the molecular axis and the normal to the substrate surface are multiples of each other, there arises a gyroscopic nutation effect [4]. According to this, the free end of a rotating gyroscope in certain points occurs in the topmost position (to yield the brightest image), while at the other points it takes the lowest position. However, by no means can all experimental observations be rationalized using this simplest model. Evidently, a more adequate quantum-chemical model has to be developed that would describe vibrations of a molecule adsorbed on a substrate and exchanging energy quanta with the surface.

The above phenomenon can be of interest from the standpoint of both basic knowledge and applications. There is a unique possibility of monitoring elementary processes. In this context, it is important to determine the frequencies of molecular vibrations and study the problem of electromagnetic energy dissipation (involving the energy conversion from thermal to electromagnetic). It is not excluded that specially selected monomolecular films exposed to electric field will allow us to control the process of electromagnetic energy absorption and emission by solid surfaces. Possible practical applications include temperature monitoring in nanodimensional structures.

Additional possibilities would be offered by a database concerning the images of various molecules adsorbed at exactly known temperatures and electric field strengths. In particular, this will provide a means of nondestructive visual identification of the chemical nature of separate molecules. In the near future, this approach in combination with advanced field-ion and atomic-probe facilities will make possible detailed investigations of the response of individual molecules and submonolayer films to temperature variations and other physical factors (laser radiation, low-energy particle bombardment, etc.).

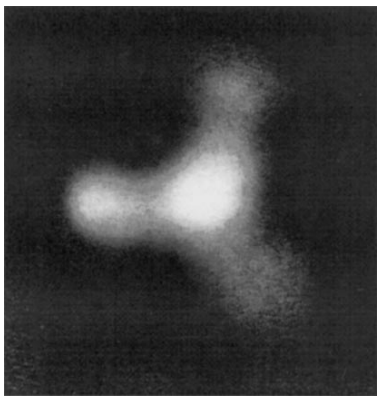

Fig. 1. Field-ion image of an adsorbed water molecule at room temperature.

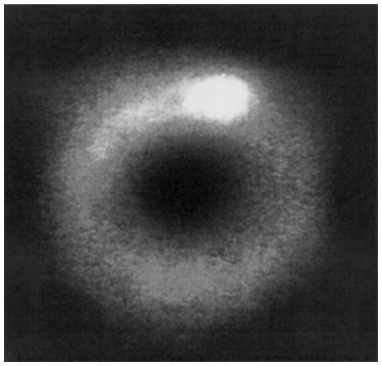

Fig. 2. Field-ion image of an adsorbed water molecule at liquid nitrogen temperature.

REFERENCES

1. Yihua Gao and Yoshio Bando, Nature **415**, 599 (2002).
2. M. K. Miller and G. D. W. Smith, *Atom Probe Microanalysis: Principles and Applications to Material Problems* (Materials Research Society, Pittsburgh, 1989; Mir, Moscow, 1993).
3. S. V. Zaĭtsev and A. V. Karpov, Prib. Tekh. Éksp. **43** (4), 144 (2000).
4. L. D. Landau and E. M. Lifshitz, *Course of Theoretical Physics*, Vol. 1: *Mechanics* (Nauka, Moscow, 1982; Pergamon Press, New York, 1988).

Translated by P. Pozdeev

Technical Physics Letters, Vol. 29, No. 2, 2003, pp. 92–94. Translated from Pis'ma v Zhurnal Tekhnicheskoĭ Fiziki, Vol. 29, No. 3, 2003, pp. 18–23.

The Diffusion Coefficient of Brownian Particles in a Rapidly Fluctuating Periodic Potential Field

A. A. Dubkov

Nizhni Novgorod State University, Nizhni Novgorod, Russia

e-mail: dubkov@rf.unn.ru

Received July 15, 2002

Abstract—An exact formula describing the effective coefficient of diffusion for Brownian particles in a rapidly fluctuating periodic potential field is derived. It is shown that, irrespective of the particular form of the potential, the particle migration is accelerated as compared to the case of free diffusion. The values of diffusion coefficients for several particular potential profiles are calculated. *© 2003 MAIK "Nauka/Interperiodica".*

Malakhov [1] showed that the diffusion of Brownian particles in a rapidly fluctuating periodic potential field can be accelerated as compared to the case of free diffusion. However, an exact formula for the effective coefficient of diffusion (D_{eff}) was obtained only for a sawtooth potential profile. This study aimed at deriving an exact relation for D_{eff} in an arbitrary periodic potential.

Let us consider, following [1], the Langevin equation for the coordinate of a Brownian particle moving in a fluctuating periodic field $U(x)$ under conditions of overdamping:

$$\frac{dx}{dt} = -\frac{dU(x)}{dx}\zeta(t) + \xi(t). \quad (1)$$

Here, $\xi(t)$ and $\zeta(t)$ are statistically independent Gaussian white noise functions with zero means, $\langle\xi(t)\rangle = \langle\zeta(t)\rangle = 0$ and the intensities D and D_ζ, respectively: $\langle\xi(t)\xi(t+\tau)\rangle = D\delta(\tau)$ and $\langle\zeta(t)\zeta(t+\tau)\rangle = D_\zeta\delta(\tau)$. In what follows, the potential $U(x)$ is considered as an even function of period L, and the origin of coordinates is placed at one of the points of minimum.

According to [2–4], the effective coefficient of diffusion is defined as the limit

$$D_{\text{eff}} = \lim_{t\to\infty}\frac{\langle x^2(t)\rangle}{t} = \lim_{t\to\infty}\frac{d}{dt}\langle x^2(t)\rangle. \quad (2)$$

The Fokker–Planck equation for the probability density $W(x, t)$ of the Brownian particle coordinate satisfying Eq. (1) can be written as

$$\frac{\partial W}{\partial t} = \frac{D_\zeta}{2}\frac{\partial}{\partial x}U'(x)\frac{\partial}{\partial x}U'(x)W + \frac{D}{2}\frac{\partial^2 W}{\partial x^2}. \quad (3)$$

Being interested only in the asymptotic behavior of the mean square coordinate, we can set the initial condition to Eq. (3) in an arbitrary manner. Let all Brownian particles at the time $t = 0$ be situated at the origin: $W(x, 0) = \delta(x)$. Then, owing to the even potential $U(x)$, the diffusion at $t > 0$ will proceed symmetrically in both directions of the Ox axis, and the probability flux at $x = 0$ and $\langle x(t)\rangle$ will be equal to zero. This implies that D_{eff} can be calculated by placing a reflecting screen at the origin and considering diffusion only in the direction of positive x.

It is convenient to introduce Laplace transform of the probability density,

$$Y(x, s) = \int_0^\infty W(x, t)e^{-st}dt,$$

which allows Eq. (3) to be written in the form of an ordinary second-order differential equation for $Y(x, s)$:

$$\frac{D_\zeta}{2}\frac{d}{dx}U'(x)\frac{d}{dx}U'(x)Y + \frac{D}{2}\frac{d^2Y}{dx^2} - sY = 0 \quad (x > 0), \quad (4)$$

supplemented by the normalization condition

$$\int_0^\infty Y(x, s)dx = \frac{1}{s}. \quad (5)$$

According to Floquet's theorem (see [5, p. 110]), linear homogeneous Eq. (4) with periodic coefficients has a solution of the type

$$Y(x, s) = e^{-\mu(s)x}\Phi(x, s), \quad (6)$$

where $\Phi(x, s)$ is a periodic function of x (with the same period L) and $\mu(s)$ is a characteristic exponent. For $s = 0$, Eq. (4) has a purely periodic solution. This implies that $\mu(s) \longrightarrow 0$ as $s \longrightarrow 0$. Note also that, according to formula (6),

$$Y(L, s) = e^{-\mu(s)L}Y(0, s). \quad (7)$$

Using the limiting theorems for Laplace's trans-

form, definition (2) can be written as

$$D_{\text{eff}} = \lim_{s \to 0} s^2 \overline{x_s^2}, \tag{8}$$

where

$$\begin{aligned} \overline{x_s^2} &= \int_0^\infty x^2 Y(x, s)dx = \int_0^\infty x^2 e^{-\mu x}\Phi(x, s)dx \\ &= \frac{\partial^2}{\partial \mu^2}\int_0^\infty e^{-\mu x}\Phi(x, s)dx. \end{aligned} \tag{9}$$

Since expression (9) enters into the limit (8), it will be sufficient to find an approximate value of this integral for $s \longrightarrow 0$ (i.e., for $\mu \longrightarrow 0$). Taking into account the periodicity of the function $\Phi(x, s)$ and the normalization condition (5), we obtain

$$\begin{aligned} \frac{1}{s} &= \int_0^\infty e^{-\mu x}\Phi(x, s)dx = \sum_{n=0}^{\infty}\int_{nL}^{(n+1)L} e^{-\mu x}\Phi(x, s)dx \\ &= \int_0^L e^{-\mu x}\Phi(x, s)dx \sum_{n=0}^{\infty} e^{-\mu nL} = \frac{1}{1 - e^{-\mu L}} \\ &\times \int_0^L e^{-\mu x}\Phi(x, s)dx \simeq \frac{1}{\mu L}\int_0^L e^{-\mu x}\Phi(x, s)dx, \end{aligned}$$

which yields

$$\overline{x_s^2} \simeq \frac{2}{\mu^3 L}\int_0^L e^{-\mu x}\Phi(x, s)dx \simeq \frac{2}{s\mu^2}. \tag{10}$$

Substituting approximation (10) into limit (8) leads to a new expression for the effective diffusion coefficient:

$$D_{\text{eff}} = 2\lim_{s \to 0}\frac{s}{\mu^2(s)}, \tag{11}$$

which reduces the problem to determining the characteristic exponent μ in the solution to Eq. (4). Calculating this value presents certain difficulties, because the procedure is based on the condition that an infinitely large determinant tends to zero [5]. However, in the case under consideration, the value of $\mu(s)$ is determined directly from relation (7).

Introducing a new variable

$$Z(x, s) = \sqrt{D + D_\zeta[U'(x)]^2}\,Y(x, s), \tag{12}$$

we can rewrite Eq. (4) in a self-conjugated form

$$\frac{1}{2}\sqrt{D + D_\zeta[U'(x)]^2}\frac{d}{dx}\sqrt{D + D_\zeta[U'(x)]^2}\frac{dZ}{dx} - sZ = 0. \tag{13}$$

By substituting an independent variable

$$u = \int_0^x \frac{dy}{\sqrt{D + D_\zeta[U'(y)]^2}},$$

Eq. (13) can be reduced to a linear equation with constant coefficients and, hence, readily solved. In the region of $x > 0$, a bounded solution to Eq. (13) is as follows:

$$Z(x, s) = C_0(s)\exp\left\{-\sqrt{2s}\int_0^x \frac{dy}{\sqrt{D + D_\zeta[U'(y)]^2}}\right\}, \tag{14}$$

where $C_0(s)$ is a constant quantity determined from the normalization condition (5). Since the factor at $Y(x, s)$ in expression (12) for the new variable is a periodic function, the characteristic exponent of solution (14) must coincide with $\mu(s)$. Using a relation analogous to formula (7) for $Z(x, s)$ expressed in the form of (14), we obtain

$$\mu(s) = \frac{\sqrt{2s}}{L}\int_0^L \frac{dy}{\sqrt{D + D_\zeta[U'(y)]^2}}.$$

Substituting this expression for $\mu(s)$ into relation (11), we obtain an exact formula for the effective diffusion coefficient of Brownian particles in the field of an arbitrary periodic potential $U(x)$:

$$D_{\text{eff}} = D\left[\frac{1}{L}\int_0^L \frac{dx}{\sqrt{1 + D_\zeta[U'(x)]^2/D}}\right]^{-2}. \tag{15}$$

As can be seen from formula (15), $D_{\text{eff}} > D$ for a $U(x)$ profile of any shape, which means that the diffusion of particles is accelerated as compared to the case of $U(x) = 0$. This result fully confirms the aforementioned assumption made in [1]. Note that, in contrast to the case of a constant periodic field [2–4], the effective diffusion coefficient is determined by the slope $U'(x)$ of the potential barrier rather than by the barrier height.

Let us consider some particular types of the $U(x)$ profile. For a sawtooth profile $U(x) = 2E|x|/L$ ($|x| \le L/2$), we immediately arrive at the exact result obtained by Malakhov [1]:

$$D_{\text{eff}} = D + D_\zeta\frac{4E^2}{L^2}. \tag{16}$$

For a sinusoidal potential $U(x) = E\sin^2(\pi x/L)$, formula (15) yields

$$D_{\text{eff}} = \frac{\pi^2 D(1 + \gamma^2)}{4\mathbf{K}^2(\gamma/\sqrt{1 + \gamma^2})}, \quad \gamma = \frac{\pi E}{L}\sqrt{\frac{D_\zeta}{D}}, \tag{17}$$

where $\mathbf{K}(k)$ is the complete elliptic integral of the first kind ($0 < k < 1$). For the modulating noise of a low-

intensity D_ζ ($\gamma \ll 1$), expression (17) transforms to

$$D_{\text{eff}} \simeq D + D_\zeta \frac{\pi^2 E^2}{2L^2}. \quad (18)$$

Formula (18) coincides with the approximate result obtained in [1] assuming a Gaussian probability density function $W(x, t)$. In the opposite case of $\gamma \gg 1$, we can use an asymptotic formula for the elliptic integral [6],

$$\mathbf{K}(k) \simeq \ln \frac{4}{\sqrt{1-k^2}} \quad (k \longrightarrow 1),$$

for which expression (17) yields

$$D_{\text{eff}} \simeq \frac{D(\pi\gamma)^2}{4\ln^2\gamma} \sim \frac{D_\zeta}{\ln^2 D_\zeta}. \quad (19)$$

According to this result, the effective diffusion coefficient increases with the modulating noise intensity D_ζ, but slower as compared to the case of a linear law (16).

In conclusion, it should be noted that the exact expression (15) can be written in a more "physical" form:

$$D_{\text{eff}} = \frac{L^2}{\tau(0)}, \quad (20)$$

where $\tau(0)$ is the mean first-passage time of the boundary $x = L$ for the Brownian particles starting at the reflecting boundary ($x = 0$). Previously, formula (20) was obtained by Weaver [3] for diffusion in a constant periodic field.

The above results, confirming the possibility of accelerating diffusion by means of rapid stochastic modulation of the field with a given spatial period, can be of interest for modern diffusion technologies employed in the synthesis of materials for solid state electronics.

Acknowledgments. This study was supported by the Russian Foundation for Basic Research (project nos. 00-15-96620 and 02-02-17517), the INTAS Foundation (grant no. 2001-0450), and the Federal Program "Universities of Russia" (project UR.01.01.008).

REFERENCES

1. A. N. Malakhov, Pis'ma Zh. Tekh. Fiz. **24** (21), 9 (1998) [Tech. Phys. Lett. **24**, 833 (1998)].
2. R. Festa and E. G. d'Agliano, Physica A **90**, 229 (1978).
3. D. L. Weaver, Physica A **98**, 359 (1979).
4. S. Yu. Medvedev and A. I. Saichev, Radiotekh. Élektron. (Moscow) **24**, 2058 (1979).
5. E. Kamke, *Gewöhnliche Differentialgleichungen* (Academie Verlag, Leipzig, 1959; Nauka, Moscow, 1976).
6. G. A. Korn and T. M. Korn, *Mathematical Handbook for Scientists and Engineers* (McGraw-Hill, New York, 1961; Nauka, Moscow, 1973).

Translated by P. Pozdeev

Technical Physics Letters, Vol. 29, No. 2, 2003, pp. 95–96. Translated from Pis'ma v Zhurnal Tekhnicheskoĭ Fiziki, Vol. 29, No. 3, 2003, pp. 24–28.

Tensoresistive Effects in Tin-Doped Silicon under Static and Dynamic Pressure Conditions

O. O. Mamatkarimov and R. Kh. Khamidov

National University of Uzbekistan, Tashkent, Uzbekistan

Received August 14, 2002

Abstract—Tensoresistive effects under static and dynamic pressure conditions have been studied in single crystal silicon doped with tin. For undoped silicon (KEF 15 grade), the change in the current under pressure relative to the initial value is 5–8%. For samples of *n*-Si⟨Sn⟩, the corresponding changes amount to 25–30% under static pressure and to 55–60% under pulsed pressure conditions. The results are interpreted in terms of variation of the local internal mechanical stresses created by the impurity atoms. © *2003 MAIK "Nauka/Interperiodica".*

The creation of pressure-sensitive solid state electronic devices with preset working characteristics requires a material possessing low resistivity in combination with a sufficiently high strain gauge factor. In practice, this problem can be solved by doping silicon with an impurity, which can increase the tensoresistive response of the initial semiconductor material while decreasing (or at least not increasing) the resistivity. As is known [1], isovalent impurity atoms occupy the lattice sites in silicon and do not change the density of charge carriers. However, the presence of such an impurity can modify the physicochemical properties of the initial material.

Recently [2], it was demonstrated that doping silicon with impurities creating deep levels in the forbidden band renders the material more sensitive with respect to external factors. In particular, an increased tensoresistive effect in a doped material is related to a pressure-induced shift in the energy position of these deep levels relative to the allowed energy bands. However, since the isovalent impurities (including Sn) do not change the electrical properties of silicon, the tensoresistive effect observed in Si⟨Sn⟩ cannot be explained by the aforementioned shift of deep energy levels.

In this context, we have studied the tensoresistive effect in tin-doped silicon under external pressure applied in various regimes. The samples, prepared by introducing tin in the course of growing silicon single crystals, had a resistivity of 15 Ω cm. The experiments were performed in a setup described elsewhere [3].

Figure 1 presents experimental data on the pressure-induced variation of the current at various temperatures (curves *1*', *2*') and the carrier mobility (curve *3*') in tin-doped silicon in comparison to the values observed in the undoped material (curves *1–3*, respectively). As can be seen from these data, the carrier mobility is, irrespective of the temperature, almost independent of hydrostatic pressure both in the undoped silicon and in Si⟨Sn⟩. However, a relative pressure-induced change in the current for the tin-doped silicon amounts to I_P/I_0 = 25–30% and is temperature-dependent. The higher the temperature, the lower the relative current variation with increasing pressure.

Previously [4], it was shown that the strain gauge factor of silicon doped with impurities creating deep levels in the forbidden band decreases with increasing temperature. It was suggested that the observed variation of the tensoresistive response with the temperature was due to a change in the degree of occupation of the deep levels. However, the change in the pressure sensi-

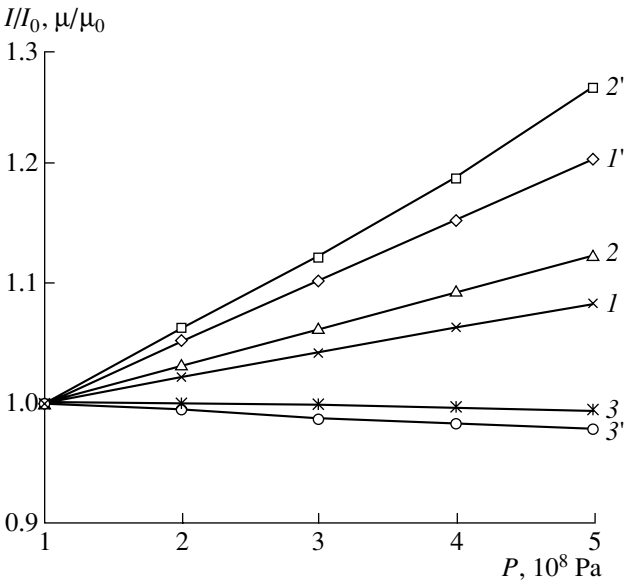

Fig. 1. Plots of the pressure-induced variation of (*1*, *2*, *1*', *2*') current at T = 313 (*1*, *1*') and 263 K (*2*, *2*') and (*3*, *3*') room-temperature carrier mobility in the (*1–3*) undoped Si and (*1*'–*3*') Si⟨Sn⟩ samples.

1063-7850/03/2902-0095$24.00 © 2003 MAIK "Nauka/Interperiodica"

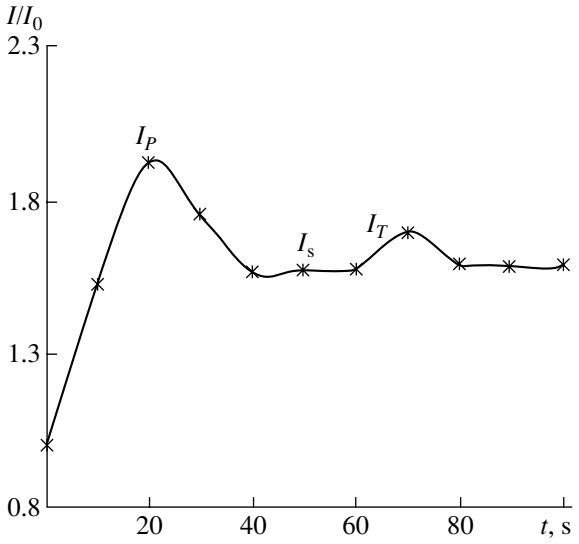

Fig. 2. Current kinetics in an Si⟨Sn⟩ sample under the action of an applied pressure pulse ($P = 5 \times 10^8$ Pa, $dP/dt = 2 \times 10^8$ Pa/s) and heating ($\Delta T = 8$ K): (I_P) pressure-pulse-induced variation; (I_s) stationary level; (I_T) temperature-induced variation.

tivity observed in the case of tin-doped silicon cannot be explained in this way, because tin, being an isovalent impurity, does not create deep impurity energy levels. We believe that the tensoresistive effect is most probably related to a change in the level of local internal elastic stresses. This hypothesis is consistent with the temperature variation of currents presented in Fig. 1. Indeed, growing temperature leads to an increase in the average distance between silicon and impurity (tin) atoms, which partly relieves the internal elastic stresses.

In order to study the dynamic tensoresistive effect in tin-doped silicon, the samples of *n*-Si⟨Sn⟩ were subjected to pressure pulses with a pressure buildup rate of 2×10^8 Pa/s. Experimental data obtained under these conditions showed that the relative change in the current for *n*-Si⟨Sn⟩ samples under pulsed pressure reaches 80–85%, in which the pure contribution due to the pressure pulse amounts to about 20%. This change cannot be explained only by the pressure-induced temperature variations.

In order to elucidate the mechanism of the dynamic tensoresistive effect observed in *n*-Si⟨Sn⟩, we performed the following series of experiments. A nichrome coil wound on the sample holder allowed the sample temperature to be controlled at a constant pressure, and a copper–constantan thermocouple glued to a sample allowed the temperature variations to be monitored. The results of measurements showed that pulsed variation of the applied pressure P from 0 to 5×10^8 Pa at a rate of 2×10^8 Pa/s leads to an increase in the sample temperature by $\Delta T = 8$ K, while the current in the sample grows by 20% relative to the static level (see the first peak in Fig. 2). After termination of the pressure pulse, the sample temperature decreases to the initial level and remains unchanged as the applied pressure is maintained at a constant level of 5×10^8 Pa. The current also decreases to I_s (Fig. 2) and then remains unchanged. Then, the sample was heated by $\Delta T = 8$ K using the nichrome coil, but the current through the sample changed only by 5% (see the second peak in Fig. 2). Thus, changes in the current that can be related to the pressure-induced temperature variations are insignificant.

The presence of isovalent impurity atoms in crystals is known to generate internal elastic stresses [1]. Therefore, the dynamic tensoresistive effect observed in our *n*-Si⟨Sn⟩ samples can be due to the buildup of elastic stresses under the action of applied pulsed pressure. This can result in the breakage of stressed valence bonds and the production of additional charge carriers. This hypothesis is confirmed by the fact that the contribution to current related to the pressure change increases with the front slope (and magnitude) of the applied pressure pulse.

REFERENCES

1. F. Talipov and R. Kh. Khamidov, Pis'ma Zh. Tekh. Fiz. **19** (2), 55 (1993) [Tech. Phys. Lett. **19**, 59 (1993)].
2. S. Z. Zaĭnabidinov, O. O. Mamatkarimov, I. G. Tursunov, and U. Tuĭchiev, Fiz. Tekh. Poluprovodn. (St. Petersburg) **34**, 641 (2000) [Semiconductors **34**, 615 (2000)].
3. A. Abduraimov, S. Z. Zaĭnabidinov, O. O. Mamatkarimov, *et al.*, Prib. Tekh. Éksp. **35** (5), 229 (1992).
4. A. Abduraimov, S. Z. Zaĭnabidinov, and O. O. Mamatkarimov, Uzbek. Fiz. Zh., No. 3, 47 (1993).

Translated by P. Pozdeev

Technical Physics Letters, Vol. 29, No. 2, 2003, pp. 97–98. Translated from Pis'ma v Zhurnal Tekhnicheskoĭ Fiziki, Vol. 29, No. 3, 2003, pp. 29–32.

Electrical Properties of $YBa_2Cu_3O_{7-x}$ Films of Various Thicknesses

S. V. Razumov and A. V. Tumarkin

St. Petersburg State Electrotechnical University, St. Petersburg, Russia

e-mail: thinfilm@eltech.ru

Received August 6, 2002

Abstract—We have studied the electrical properties of high-T_c superconductor $YBa_2Cu_3O_{7-x}$ films obtained by the ion-plasma deposition technique on sapphire substrates. Dependences of the surface resistance and the critical current density on the film thickness are determined. *© 2003 MAIK "Nauka/Interperiodica".*

For the development of cryoelectronic devices based on the high-T_c superconductor $YBa_2Cu_3O_{7-x}$ (YBCO), it is necessary to obtain films possessing a highly perfect structure and good critical characteristics. In order to ensure localization of the field within a superconducting film and reduce the microwave losses, the film thickness has to be several times greater than the London penetration depth λ_L (according to various estimates, the λ values range from 1400 to 1800 Å) [1].

Specific conditions encountered in the microwave devices with superconducting films pose special requirements with respect to the electrical properties of such films. Besides a sufficiently high value of the superconducting transition temperature T_c, which is a traditionally important parameter, films intended for practical applications in cryoelectronics have to be characterized with respect to the surface resistance [2]. In addition, development of cryoelectronic devices requires the dc characteristics of high-T_c superconductor films to be studied as well. These parameters significantly depend on the structural perfection, configuration, and dimensions of the device elements.

We have studied the YBCO films prepared by ion-plasma sputtering of a stoichiometric ceramic target with a diameter of 76 mm in a planar dc magnetron system. The films were deposited onto sapphire substrates (*r*-cut [1$\underline{1}$02]-oriented plates) with a cerium dioxide buffer layer [3]. The process was conducted at a working gas (oxygen) pressure of 1 Torr. The substrate temperature during deposition was maintained constant at about 650°C, as monitored by a thermocouple fixed on the substrate holder. The discharge current increased from 100 to 600 mA during the first 30 min of the process and then remained unchanged. The YBCO film thicknesses (measured with a Dektak-3030 profilometer) were varied from 0.3 to 3.6 μm. The film growth rate estimated from these data was about 15 Å/min (±5%).

The structures of the as-grown YBCO films were studied by X-ray diffraction on a Geigerflex D/max-RC (Rigaku) diffractometer using monochromated CuK_α radiation (λ = 1.5418 Å). The diffractograms of the samples displayed all the allowed (00*l*) reflections, which was evidence of a perfect *c*-oriented crystal structure.

The surface morphology of the films was studied by electron microscopy. This examination revealed macrodefects of two types: pores and secondary phase inclusions. The pores were observed on the surface of relatively thick films, while the secondary phase inclusions were found on relatively thin films; slowly growing inclusions are also probable on the bottom surfaces of pores. This behavior is related to the considerable difference between the growth rates of secondary phases and the 123-YBCO phase [4, 5]. Thus, the electron-microscopic data are indicative of a change in the sample surface morphology depending on the film thickness. The relief development is manifested by an increase in the average pore size and in the surface area fraction occupied by pores, while the density of the secondary phase inclusions remains approximately constant.

All the YBCO films studied in our experiments exhibited a transition to the superconducting state at $T_c \sim 90$ K within $\Delta T = 1$ K. This behavior allows us to expect stable operation of the films in devices working at liquid nitrogen temperature (77 K).

The surface resistance R_s of the YBCO films in the microwave frequency range (8.3 GHz) was studied at 77 K in a dielectric (rutil, TiO_2) resonator. The dc current–voltage characteristics of the samples were measured by the conventional four-point-probe technique. The critical dc current density J_c was evaluated by determining the current at which a YBCO bridge features a normally conducting domain, which is manifested by a breakdown in the current–voltage characteristic. The total resistance of a sample film at the onset of the conducting domain formation is about 0.5–2.0 Ω.

1063-7850/03/2902-0097$24.00

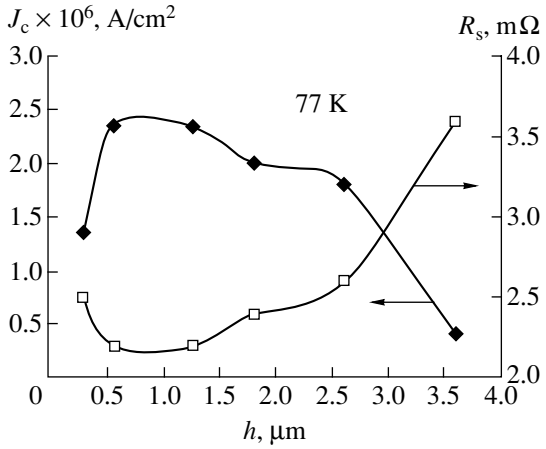

Plots of the surface resistance R_s and critical current density J_c versus thickness h for the YBCO films studied at liquid nitrogen temperature.

The results of our measurements of the surface resistance (R_s) and the critical dc current density (J_c) are plotted in the figure as functions of the film thickness (h). As can be seen from these data, the YBCO films with a thickness of about 1 μm are characterized by a combination of low surface resistance (2.2 mΩ at 8.3 GHz) and relatively high critical current density (2.3 MA/cm^2). A significant drop in the critical current density observed for films with thicknesses above 2.6 μm, together with a growth in the surface resistance, indicates that strongly developed surface relief and the large area occupied by pores (relative to the total area of the superconducting phase) are factors detrimentally influencing the electrical properties of the YBCO films studied.

The greater the film thickness, the larger the pore dimensions and the surface area fraction occupied by the pores. These trends indicate that there are at least two competitive processes influencing the quality of the YBCO film structure. The first is the slow growth of a secondary phase on the pore bottom, which leads to a decrease in the number of defects and in the level of stresses in the 123-YBCO phase [4, 5]. The second process is the increase in the total surface area occupied by pores, which decreases the film quality. Therefore, one can speak of a certain limiting thickness below which the YBCO films retain high structural and electrical properties and can be used in microwave devices. Under the conditions studied in our experiments, this limiting thickness is about 2.6 μm.

Thus, the results of our investigation of the surface resistance and the critical current density of YBCO films unambiguously indicate that such films, fabricated by ion-plasma deposition technology, have good prospects for use in cryoelectronic devices. Especially promising are the films with thicknesses in the range from 1 to 2.6 μm: while ensuring the best electrical properties, these values exceed the London penetration depth, which is an important advantage from the standpoint of microwave cryoelectronics.

Acknowledgments. This study was supported by the Russian Foundation for Basic Research, project no. 02-02-17667.

REFERENCES

1. Y. J. Tian, L. P. Guo, L. Li, *et al.*, Appl. Phys. Lett. **65**, 234 (1994).
2. A. B. Kozyrev, E. K. Hollmann, A. V. Ivanov, *et al.*, Integr. Ferroelectr. **17**, 257 (1997).
3. E. K. Hollmann, S. V. Razumov, and A. V. Tumarkin, Pis'ma Zh. Tekh. Fiz. **25** (11), 47 (1999) [Tech. Phys. Lett. **25**, 440 (1999)].
4. E. K. Hollmann, V. I. Gol'drin, D. A. Plotkin, *et al.*, Pis'ma Zh. Tekh. Fiz. **22** (22), 82 (1996) [Tech. Phys. Lett. **22**, 942 (1996)].
5. E. K. Hollmann, V. I. Gol'drin, D. A. Plotkin, *et al.*, Fiz. Tverd. Tela (St. Petersburg) **39**, 216 (1997) [Phys. Solid State **39**, 189 (1997)].

Translated by P. Pozdeev

Technical Physics Letters, Vol. 29, No. 2, 2003, pp. 99–101. Translated from Pis'ma v Zhurnal Tekhnicheskoĭ Fiziki, Vol. 29, No. 3, 2003, pp. 33–39.

Analytical Solution of a Model Kinetic Equation with Variable Frequency of Collisions for a Gas Streamlining a Cylindrical Surface

V. N. Popov

Pomorskiĭ State University, Arkhangelsk, Russia
e-mail: popov.vasily@pomorsu.ru

Received July 31, 2002

Abstract—An analytical method is proposed for solving a boundary-value problem in a half-space for the inhomogeneous Boltzmann equation with a collision operator in the form of the Bhatnagar–Gross–Kruck model, where the collision parameter is proportional to the absolute velocity of gas particles. The method is applied to description of a rarefied gas flow with inhomogeneous distributions of the temperature and the mass flow velocity, streamlining a right circular cylinder. © *2003 MAIK "Nauka/Interperiodica".*

Previously [1, 2], the problem of calculating the velocity of a rarefied gas with inhomogeneous temperature and mass flow velocity distributions, sliding around a right circular cylindrical surface, was analytically solved with allowance for the influence of a curved solid–gas interface on the thermal and isothermal sliding coefficients. The solution was obtained, using the Chapman–Enskog approximation and the Bhatnagar–Gross–Kruck (BGK) model, for the Boltzmann kinetic equation with a constant frequency of collisions. Below, an analytical solution is presented for the same problem with the BGK model in which the collision parameter is proportional to the absolute velocity of gas particles [3, 4].

Consider a solid cylindrical surface streamlined by the flow of a rarefied gas with inhomogeneous temperature distribution and small deviations from the equilibrium state. The gas flow will be described in terms of the Boltzmann equation with a collision operator in the form of the aforementioned BGK model. The problem under consideration admits two qualitatively different situations, whereby the temperature gradient and the mass flow velocity far from the cylinder surface are either perpendicular (transverse streamlining) or parallel (longitudinal streamlining) to the cylinder axis. A boundary condition on the cylinder surface will correspond to the model of diffuse reflection.

Let us linearize a distribution function describing the state of the gas relative to the distribution function in the gas volume in the Chapman–Enskog approximation. Expanding the $Y(\rho, \varphi, \mathbf{C})$ function (describing the deviation of the gas distribution function with respect to the velocities and coordinates of molecules in the Knudsen layer from the volume distribution function) into series in the small parameter $1/R$,

$$Y(\rho, \varphi, \mathbf{C}) = Y^{(1)}(\rho, \varphi, \mathbf{C}) + R^{-1}Y^{(2)}(\rho, \varphi, \mathbf{C}) + \ldots, \quad (1)$$

we arrive at an equation for determining the function $Y^{(2)}(\rho, \varphi, \mathbf{C})$,

$$C_\rho \frac{\partial Y^{(2)}}{\partial \rho} + CY^{(2)}(\rho, \varphi, \mathbf{C}) = \frac{\sqrt{\pi}}{2} C \int \rho(C') K(\mathbf{C}, \mathbf{C}') \times Y^{(2)}(\rho, \varphi, \mathbf{C}') d\mathbf{C}' - C_\varphi^2 \frac{\partial Y^{(1)}}{\partial C_\rho} + C_\rho C_\varphi \frac{\partial Y^{(1)}}{\partial C_\varphi} - C_\varphi \frac{\partial Y^{(1)}}{\partial \varphi}, \quad (2)$$

with the boundary conditions

$$Y^{(2)}(R, \varphi, \mathbf{C}) = -2\mathbf{C}\mathbf{U}^{(2)}, \quad (C_r > 0),$$
$$Y^{(2)}(\infty, \varphi, \mathbf{C}) = 0.$$

In Eqs. (1) and (2), the function $Y^{(1)}(\rho, \varphi, \mathbf{C})$ coincides with a solution to the problem of a rarefied gas sliding along a flat solid surface [4]; ρ is the dimensionless distance measured from the cylinder axis; R is the dimensionless radius of the cylinder; $\beta\mathbf{U}^{(2)}$ and $\beta\mathbf{C}$ are the mass flow velocity and the intrinsic velocity of gas molecules, respectively; $\rho(C) = \pi^{-3/2} C \exp(-C^2)$; and

$$K(\mathbf{C}, \mathbf{C}') = 1 + \frac{3}{2}\mathbf{C}\mathbf{C}' + \frac{1}{2}(C^2 - 2)(C'^2 - 2).$$

Equation (2) is written in a cylindrical coordinate system with the Oz axis coinciding with the cylinder axis. Let us assume that the temperature gradient far from the cylinder surface is perpendicular to this sur-

face, which implies that the quantity $(1/T_S)(\partial T/R\partial\varphi)|_S$ is nonzero. In this case,

$$Y^{(1)}(x, \varphi, \mathbf{C}) = C_\varphi\left(C - \frac{5}{2C}\right)\exp(-x/\mu)\Theta_+(\mu), \quad (3)$$

$$Y^{(2)}(x, \varphi, \mathbf{C}) = C_\varphi Z(x, \varphi, C_\rho) + \sum_k b_k(C_z, C_\varphi)L_k(x, \varphi, C_\rho), \quad (4)$$

where C_φ forms, together with $b_k(C_z, C_\varphi)$, a complete set of orthogonal polynomials (in terms of the scalar product); $\Theta_+(\mu)$ is the Heaviside step function; and $x = \rho - R$.

Let us pass to a spherical coordinate system in the space of velocities [4]:

$$C_\rho = C\cos\eta; \quad C_\varphi = C\sin\eta\cos\xi;$$
$$C_z = C\sin\eta\sin\xi.$$

Denoting $\mu = \cos\eta$, substituting expressions (3) and (4) into (2), multiplying the obtained equations by $\exp(-C^2)\cos\xi$, and integrating with respect to ξ (from 0 to 2π) and C (from 0 to $+\infty$), we arrive at a homogeneous integrodifferential equation

$$\mu\frac{\partial Z}{\partial x} + Z(x, \varphi, \mu) = \frac{3}{4}\int_{-1}^{1}(1-\tau^2)Z(x, \varphi, \tau)d\tau \quad (5)$$

with the boundary conditions

$$Z(0, \varphi, \mu) = -2U_\varphi^{(2)}\big|_S \ (\mu > 0), \quad Z(\infty, \varphi, \mu) = 0. \quad (6)$$

The general solution to Eq. (5) is [4]

$$Z(x, \varphi, \mu) = A_0 + A_1(x-\mu) + \int_{-1}^{1}\exp(-x/\eta)\Phi(\eta, \mu)n(\eta, \varphi)d\eta, \quad (7)$$

$$\Phi(\eta, \mu) = \frac{3}{4}\eta P\frac{1}{\eta-\mu} + \frac{\lambda(\eta)}{1-\eta^2}\delta(\eta-\mu),$$

$$\lambda(\eta) = 1 + \frac{3}{4}\eta\int_{-1}^{1}\frac{1-\mu^2}{\mu-\eta}d\mu,$$

$$X(z) = \frac{1}{z}\exp\left(\frac{1}{\pi}\int_0^1\frac{\zeta(\tau)d\tau}{\tau-z}\right),$$

$$\zeta(\tau) = -\frac{\pi}{2} - \arctan\frac{4\lambda(\tau)}{3\pi\tau(1-\tau^2)},$$

where $\lambda(z)$ is the dispersion function; Px^{-1} is the distribution in the sense of the principal value for the integral of x^{-1}; and $\delta(x)$ is the Dirac delta function. On the real positive semiaxis, the integral in the expression for $X(z)$ has the sense of the principle value. For the sake of brevity, the argument φ in $n(\eta, \varphi)$ in what follows will be omitted.

For $A_0 = A_1 = 0$, the solution (7) satisfies the boundary condition at infinity. Now let us select $n(\eta)$ such that the boundary condition is obeyed on the solid wall. Assuming $x = 0$, we obtain from Eqs. (7) the relation

$$-2U_\varphi^{(2)}\big|_S = \frac{3}{4}\int_0^1\frac{\eta n(\eta)}{\eta-\mu}d\eta + \frac{\lambda(\mu)}{1-\mu^2}n(\mu). \quad (8)$$

Introducing the function

$$N(z) = \int_0^1\frac{\eta n(\eta)}{\eta - z}d\eta, \quad (9)$$

we can write Sokhotsky's formulas for the limiting values of $N(z)$ and $\lambda(z)$ from above and below on the [0, 1] and [–1, 1] sections, respectively:

$$N^+(\mu) - N^-(\mu) = 2\pi i\mu n(\mu),$$
$$N^+(\mu) + N^-(\mu) = 2\int_0^1\frac{\eta n(\eta)}{\eta-\mu}d\eta,$$

$$\lambda^+(\mu) - \lambda^-(\mu) = \frac{3\pi i}{2}\mu(1-\mu^2),$$
$$\lambda^+(\mu) + \lambda^-(\mu) = 2\lambda(\mu).$$

Using these relations, we can reduce equation (8) to a homogeneous boundary-value problem

$$\left[N^+(\mu) + \frac{8}{3}U_\varphi^{(2)}\big|_S\right]\lambda^+(\mu) - \left[N^-(\mu) + \frac{8}{3}U_\varphi^{(2)}\big|_S\right]\lambda^-(\mu) = 0.$$

Upon factorization of the boundary-value problem coefficient, we obtain a relation

$$\left[N^+(\mu) + \frac{8}{3}U_\varphi^{(2)}\big|_S\right]X^+(\mu) - \left[N^-(\mu) + \frac{8}{3}U_\varphi^{(2)}\big|_S\right]X^-(\mu) = 0.$$

A solution to the above boundary-value problem is

$$N(z) = -\frac{8}{3}U_\varphi^{(2)}\big|_S. \quad (10)$$

In order to ensure that expressions (9) and (10) determine the same function, it is necessary that $N(z) = O(1/z)$ for $|z| \longrightarrow \infty$, from which it follows that $U_\varphi^{(2)}\big|_S = 0$.

Thus, using the BGK model with a variable frequency of collisions in the problem of a rarefied gas flow sliding along a solid spherical surface under the conditions of transverse streamlining of a right circular cylinder leads to a zero correction for the surface curvature effect. In the case of a longitudinal gas flow along

the cylinder, the quantities $(1/T_S)(\partial T/\partial z)|_S$ is nonzero, and, accordingly,

$$Y^{(1)}(x, \mathbf{C}) = C_z\left(C - \frac{5}{2C}\right)\exp(-x/\mu)\Theta_+(\mu),$$

$$Y^{(2)}(x, \mathbf{C}) = C_z Z_1(x, C_\rho) + \sum_k b_k(C_z, C_\varphi)L_k^{(1)}(x, C_\rho).$$

Both the equation and the boundary conditions for $Z_1(x, C_\rho)$ coincide to within the notations with expressions (5) and (6). From this, it follows that $U_z^{(2)}\big|_S = 0$. Therefore, the longitudinal flow of a rarefied gas with inhomogeneous temperature distribution along the surface of a right circular cylinder is also characterized by a zero correction for the surface curvature.

Let us assume that the mass flow velocity component tangent to the cylinder surface varies along the normal and that the mass flow velocity far from the cylinder surface is perpendicular to the cylinder axis. In this case, the quantity $(1U_\varphi/\partial\rho)|_S$ is nonzero, and we obtain

$$Y^{(1)}(x, \varphi, \mathbf{C}) = C_\varphi\psi(x, \varphi, \mu), \tag{11}$$

$$\psi(x, \varphi, \mu) = \int_0^1 \exp(-x/\eta)\Phi(\eta, \mu)a(\eta, \varphi)d\eta, \tag{12}$$

$$Y^{(2)}(x, \varphi, \mathbf{C}) = C_\varphi Z_2(x, \varphi, C_\rho) + \sum_k b_k(C_z, C_\varphi)L_k^{(2)}(x, \varphi, C_\rho).$$

Substituting expressions (11) and (12) into (2) and passing to a spherical coordinate system in the space of velocities, we obtain the equation

$$\mu\frac{\partial Z_2}{\partial x} + Z_2(x, \varphi, \mu) = \frac{3}{4}\int_{-1}^1 (1-\tau^2)Z_2(x, \varphi, \tau)d\tau - \frac{3}{2}(1-\mu^2)\frac{\partial\psi}{\partial\mu} + \mu\psi(x, \varphi, \mu) \tag{13}$$

with the boundary conditions

$$Z_2(0, \varphi, \mu) = -2U_\varphi^{(2)}\big|_S \ (\mu > 0), \ \ Z_2(\infty, \varphi, \mu) = 0. \tag{14}$$

Direct substitution shows that the term $\mu\psi(x, \varphi, \mu)$ does not contribute to the velocity of gas sliding around the surface, because the corresponding partial solution to Eq. (13) has the form of $x\psi(x, \varphi, \mu)$ and goes to zero on the cylinder surface ($x = 0$).

A comparison of Eqs. (13) and (14) to the analogous expressions obtained [5] for a rarefied gas with inhomogeneous temperature distribution streamlining a spherical solid surface shows that the velocity of the transverse gas flow past the right circular cylinder is 1.5 times that for the isothermal sliding along the spherical solid surface: $U_\varphi^{(2)}\big|_S = 0.42857145\dfrac{\partial U_\varphi}{\partial\rho}\Big|_S$ versus $0.2857143\dfrac{\partial U_\theta}{\partial\rho}\Big|_S$ [5].

In the case of a longitudinal gas flow along the cylinder surface, the quantity $(\partial U_z/\partial\rho)|_S$ is nonzero, and one can readily obtain

$$Y^{(1)}(x, \mathbf{C}) = C_z\psi(x, \mu),$$

$$Y^{(2)}(x, \mathbf{C}) = C_z Z_3(x, C_\rho) + \sum_k b_k(C_z, C_\varphi)L_k^{(3)}(x, C_\rho),$$

$$\mu\frac{\partial Z_3}{\partial x} + Z_3(x, \varphi, \mu) = \frac{3}{4}\int_{-1}^1 (1-\tau^2)Z_3(x, \varphi, \tau)d\tau - (1-\mu^2)\frac{\partial\psi}{\partial\mu},$$

$$Z_3(0, \varphi, \mu) = -2U_z^{(2)} \ (\mu > 0), \quad Z_3(\infty, \varphi, \mu) = 0,$$

$$U_z^2\big|_S = 0.2857143\frac{\partial U_z}{\partial\rho}\Big|_S.$$

Passing to dimensional variables and taking into account relation (1), we can evaluate the velocities of the transverse ($U_\varphi|_S$) and longitudinal ($U_z|_S$) sliding of the rarefied gas along the right circular cylinder surface:

$$U_\varphi|_S = 0.9375\nu\frac{1}{T_S}\frac{\partial T}{R\partial\varphi}\Big|_S + 1.0922\lambda(1 - 1.3795218\mathrm{Kn})\frac{\partial U_\varphi}{\partial\rho}\Big|_S,$$

$$U_z|_S = 0.9375\nu\frac{1}{T_S}\frac{\partial T}{\partial z}\Big|_S + 1.0922\lambda(1 - 0.9196812\mathrm{Kn})\frac{\partial U_z}{\partial\rho}\Big|_S,$$

where ν is the kinematic viscosity, λ is the mean free path of molecules in the gas, and $\mathrm{Kn} = \lambda/R$ is the Knudsen number.

REFERENCES

1. V. N. Popov, Zh. Tekh. Fiz. **72** (10), 15 (2002) [Tech. Phys. **47**, 1219 (2002)].
2. A. V. Latyshev, V. N. Popov, and A. A. Yushkanov, Pis'ma Zh. Tekh. Fiz. **28** (5), 70 (2002) [Tech. Phys. Lett. **28**, 204 (2002)].
3. A. V. Latyshev and A. A. Yushkanov, Izv. Ross. Akad. Nauk, Mekh. Zhidk. Gaza, No. 3, 140 (1996).
4. A. V. Latyshev and A. A. Yushkanov, Available from VINITI, No. 1360-B96 (25.04.96) (Moscow, 1996).
5. A. V. Latyshev, V. N. Popov, and A. A. Yushkanov, Inzh.-Fiz. Zh. **75** (3), 104 (2002).

Translated by P. Pozdeev